Investigations of Electron, Ion, and Proton Transport in Zirconium-based Metal-Organic Frameworks

Paula Juliana Celis Salazar

Dissertation submitted to the faculty of the Virginia Polytechnic Institute and State University in partial fulfillment of the requirements for the degree of

Doctor of Philosophy
In
Chemistry

Amanda J. Morris, Chair

James M. Tanko

Brian M. Tissue

John R. Morris

May 4th, 2018
Blacksburg, VA

Keywords: metal-organic frameworks, electron transport, electrochemistry, quinone chemistry, proton-coupled electron transport, electronic and ionic diffusion, charge storage

Investigations of Electron, Ion, and Proton Transport in Zirconium-based Metal-Organic Frameworks

Paula Juliana Celis Salazar

ABSTRACT

Metal-Organic Frameworks (MOFs) are porous materials consisting of organic ligands connected by inorganic nodes. Their structural uniformity, high surface area, and synthetic tunability, position these frameworks as suitable active materials to achieve efficient and clean electrochemical energy storage. In spite of recent demonstrations of MOFs undergoing diverse electrochemical processes, a fundamental understanding of the mechanism of electron, proton, and ion transport in these porous structures is needed for their application in electronic devices. The current work focuses on contributing to such understanding by investigating proton-coupled electron transfer, capacitance performance, and the relative contribution of electron and ionic transport in the voltammetry of zirconium-based MOFs.

First, we investigated the effects that the quinone ligand orientation inside two new UiO-type metal-organic frameworks (2,6-Zr-AQ-MOF and 1,4-Zr-AQ-MOF) have on the ability of the MOFs to achieve proton and electron conduction. The number of electrons and protons transferred by the frameworks was tailored in a Nernstian manner by the pH of the media, revealing different electrochemical processes separated by distinct pKa values. In particular, the position of the quinone moiety with respect to the zirconium node, the effect of hydrogen bonding, and the amount of defects in the MOFs, lead to different PCET processes. The ability of the MOFs to transport

discrete numbers of protons and electrons, suggested their application as charge carriers in electronic devices.

With that purpose in mind, we assembled 2,6-Zr-AQ-MOF and 1,4-Zr-AQ-MOF into two different types of working electrodes: a slurry-modified glassy carbon electrode, and as solvothermally-grown MOF thin films. The specific capacitance and the percentage of quinone accessed in the two frameworks were calculated for the two types of electrodes using cyclic voltammetry in aqueous buffered media as a function of pH. Both frameworks showed an enhanced capacitance and quinone accessibility in the thin films as compared to the powder-based electrodes, while revealing that the structural differences between 2,6-Zr-AQ-MOF and 1,4-Zr-AQ-MOF in terms of defectivity and the number of electrons and protons transferred were directly influencing the percentage of active quinones and the ability of the materials to store charge.

Additionally, we investigated in detail the redox-hopping electron transport mechanism previously proposed for MOFs, by utilizing the chronoamperometric response (I vs. t) of three metallocene-doped metal-organic frameworks (MOFs) thin films (M-NU-1000, M= Fe, Ru, Os) in two different electrolytes ($TBAPF_6$ and TBATFAB). We were able to elucidate, for the first time, the diffusion coefficients of electrons and ions (D_e and D_i, respectively) through the structure in response to an oxidizing applied bias. The application of a theoretical model for solid state-voltammetry to the experimental data revealed that the diffusion of ions is the rate-determining step at the three different time stages of the electrochemical transformation. Remarkably, the trends observed in the diffusion coefficients (D_e and D_i) of these systems obtained in PF_6^{1-} and $TFAB^{1-}$ based electrolytes at the different stages of the electrochemical reaction, demonstrated that the redox hopping rates inside frameworks can be controlled through the modifications of the self-exchange rates of redox centers, the use of large MOF channels, and the utilization of smaller

counter anions. These structure-function relationships provide a foundation for the future design, control, and optimization of electronic and ionic transport properties in MOF thin films.

Investigations of Electron, Ion, and Proton Transport in Zirconium-based Metal-Organic Frameworks

Paula Juliana Celis Salazar

GENERAL AUDIENCE ABSTRACT

The necessity of implementing new energy storage systems that enable the utilization of clean energy in diverse technologies such as electric vehicles and smart power grids, has generated great research efforts in the field of materials science. In particular, the development of nanoscale-based materials that can be utilized in batteries and supercapacitors is essential for achieving effective and clean electrochemical energy storage. Two of the main desired properties for such materials to be employed as electrodes in energy storage devices are high surface area and the possibility of incorporating redox-active moieties that are able to store electricity.

Metal-Organic Frameworks (MOFs) are a relatively new kind of porous materials with high surface area and structural uniformity, consisting of organic ligands connected by inorganic nodes. The application of these materials in charge transport and storage is still in its early stages. Therefore, fundamental understanding of the mechanism of electron, proton, and ion transport in MOFs is necessary for a rational design of these porous structures. In order to contribute to such understanding, the present work is focus on two main concepts: (1) elucidating the effect that the tridimensional orientation of redox moieties inside the MOF could have on the charge storage performance and the ability of the material to achieve proton and electron conduction; and (2) quantifying for the first time the individual relative contribution of electron and ionic transport in MOF materials.

Acknowledgements

First, I would like to thank my graduate advisor, Professor Amanda J. Morris, for her academic guidance and devoted efforts during the last five years. Pursuing doctoral studies in the United States was a dream that I had for many years and I will never forget that it was Dr. Amanda Morris who believed in me and gave me the wonderful opportunity of joining her group which made that dream come true. She is an excellent mentor and an inspiring example as a scientist and researcher. During my years at her laboratory I grew academically and professionally, and I am sincerely grateful for all the lessons she taught me. Thanks to her guidance I have become a more goal-oriented person and learned to always put the best of myself into every task encountered. Additionally, I would like to thank her for her patience, time, hard-work, discipline, and commitment to the work presented in this dissertation.

I would also like to thank all of my current and past committee members, Professors Brian Hanson, James Tanko, Brian Tissue, and John Morris for all their support during my years at the Chemistry Department of Virginia Tech. I owe a debt of gratitude to Professor Brian Hanson for encouraging me to apply for the doctoral chemistry program and for his guidance and friendship during my years at Virginia Tech. I also have a lot of appreciation for the support and help offered by Dr. James Tanko, Dr. John Morris, and Dr. Brian Tissue during all the milestones of the doctoral program. I would like to also thank Dr. Carla Slebodnick for her guidance on single-crystal X-ray Diffraction, a technique that I loved learning.

Additionally, I would like to thank my labmates for their friendship and support. I have had a wonderful time at the Dr. Amanda Morris laboratory. I am very grateful for the valuable advice of Dr. William Maza and Dr. Pavel Usov, who gave me much chemical and career advice. Especially, I would like to thank Shaoyang Lin, Jie Zhu, Jose Rodriguez, Jose Santiago, and Jenn

Rowe, for their unconditional friendship and support through the Ph.D. years. We all grew together!

To the Chemistry Department, Virginia Tech, the Blacksburg community, and all the friends I met during these five years, I would like to extend my gratitude for welcoming me in this country and making the last five years some of the best of my life. I always felt at home and am proud to be a Hokie. I will always carry with me fond memories of my time at Virginia Tech and will miss Blacksburg immensely.

I would like to thank my family for their unconditional support and immense love. To my mom Alix Salazar, who lived with me every moment of my graduate school years and now feels more than familiar talking about MOFs and electrochemistry. Thank you so much for being there in the distance, it would not have been possible without your optimism and love. I would also like to thank all of the Salazar family, especially my grandparents Miguel Salazar and Teresa de Salazar for their support, love, and influence in my life. You are my main inspiration.

Last, I would like to thank my wonderful husband, Micky Allen, who has been my rock, my best friend, and my main supporter through these years. Thanks for your unconditional love, patience, help, and for making my life so happy. It would not have been possible without your enthusiasm and happiness. Thanks for always being there for me. Your wise advice makes the difference.

Table of Contents

Table of Contents

Attributions

Chapters 2 of this dissertation was written using a published manuscript to which the author, Paula Juliana Celis-Salazar (P.J.C-S.), majorly contributed. The contributions of the co-authors to the presented chapters are as follows:

Chapter 2. P.J.C-S., performed experiments and assisted with manuscript writing and editing. Charity Epley performed SEM imaging. Spencer Ahrenholtz measured N_2 isotherms. Dr. William Maza contributed intellectually. Dr. Pavel Usov contributed intellectually and assisted in writing and editing. Dr. Amanda J. Morris, principle investigator, supervised the research project and provided technical insight during experimentation, and assisted in writing and editing.

Chapter 3. P.J.C-S., performed experiments and assisted with manuscript writing and editing. Dr. Linqin Mu assembled and tested coin cells. Connor Slamowitz was an undergraduate researcher on the project and performed synthesis of MOF thin films. Dr. Amanda J. Morris, principle investigator, supervised the research project and provided technical insight during experimentation, and assisted in writing and editing.

Chapter 4. P.J.C-S., performed experiments and assisted with manuscript writing and editing. Clark Cucinell was an undergraduate researcher on the project and performed synthesis of MOF thin films and ligands. Spencer Ahrenholtz initiated previous investigations relevant to the project. Meng Cai and Charity Epley performed SEM imaging. Dr. Pavel Usov contributed intellectually and assisted in writing and editing. Dr. Amanda J. Morris, principle investigator, supervised the research project and provided technical insight during experimentation, and assisted in writing and editing.

1. Introduction

1.1 Research Motivation

Transition from the current fossil fuel-based energy economy to an alternative and environmentally friendly form of energy generation and storage has become a challenge to the scientific community in the last few decades. However, greenhouse gas emissions are still growing dramatically. In 2011, world carbon dioxide emissions, due to petroleum consumption, reached 11.4 billion metric tons, a 34.2% increase as compared to the carbon dioxide emissions reported in 1981.[1] In order to alleviate the undesirable effects that greenhouse gas emissions produce in the global climate, research efforts have focused on generating new electrical energy storage systems that could contribute to the large-scale employment of emerging clean technologies, such as electric vehicles and smart power grids.[2, 3]

In particular, the development of nano-structured materials that can be utilized in batteries and supercapacitors is a fundamental part for achieving efficient and clean electrochemical energy storage.[4] Electrode materials displaying high surface area and the possibility of including redox-active moieties that are able to store electricity are suitable materials to be employed in such technologies.[5] Metal-organic frameworks (MOFs) are a relatively new class of porous materials that due to their structural uniformity, thermal and chemical stability, and inherent tunability have been proposed as active materials to achieve efficient charge storage in electronic devices.[6, 7]

In less than a decade, great research efforts have been done in the investigation of MOFs undergoing diverse electrochemical processes, validating their potential as key components of electrode materials.[6, 8] However, the rational design of MOFs requires fundamental understanding of the mechanism of electron, proton, and ion transport in these porous structures. The motivation

of the present work involves two main concepts to contribute to such understanding: (1) elucidating the effect that the orientation of redox moieties inside the MOF could have on the charge storage performance and the ability of the material to achieve proton and electron conduction; and (2) quantifying for the first time the individual relative contribution of electron and ionic transport in MOF materials. The latter two concepts aim to contribute to the current state of the art of MOF research, as well as and enhance the rational design of MOF structures based on structure-function relationships, for future applications.

1.2 Metal-organic frameworks

MOFs are highly porous materials assembled from secondary building units (metals or metal clusters) connected through organic linkers.[9, 10] These materials exhibit pores or void spaces that can be potentially occupied by host molecules.[11, 12] Figure 1.1 shows the crystal structure of MOF-5, one of the most widely studied in the literature, which has an apparent Langmuir surface area of 2900 m^2g^{-1}.[13] In fact, one of the tremendous advantages of MOFs is that they have demonstrated superior surface areas as compared to the largest surface areas of other porous materials such as activated carbon (2030 m^2g^{-1})[14] and zeolites (904 m^2g^{-1}, for zeolite-Y).[15, 16] At the present time, the highest surface area known for a porous material is 7140 m^2g^{-1}, for MOF NU-110.[17] Additionally, other remarkable advantages such as the high permanent microporosity, low density, crystallinity, and the inherent tunability of MOFs make them suitable materials for charge storage applications.[16, 18]

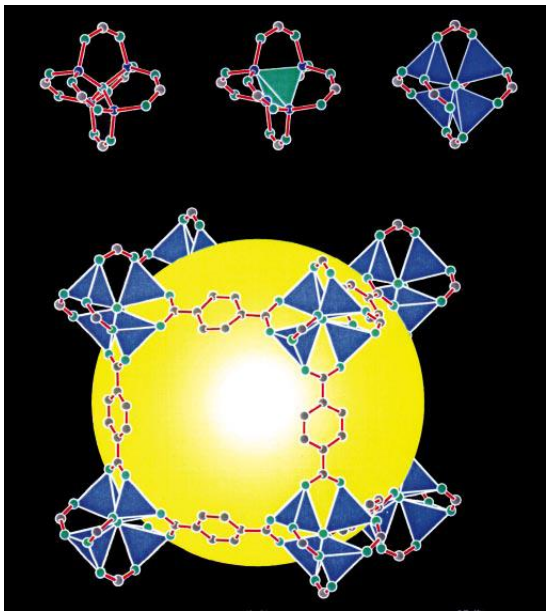

Figure 1.1: MOF-5 crystal structure. Top, the secondary building unit $Zn_4(O)O_{12}C_6$. Left, as a ball and stick model (Zn, blue; O, green; C, grey). Middle, with the $Zn_4(O)$ tetrahedron indicated in green. Right, with the ZnO_4 tetrahedra indicated in blue. Bottom, one of the cavities in the MOF-5 framework. Eight clusters constitute a unit cell and enclose a cavity, indicated by a yellow sphere of diameter 18.5 A°. This image was copied from Reference 13.

1.2.1 Zirconium MOFs

The assembly of metal-organic frameworks containing zirconium nodes constituted a milestone in the design and application of MOF materials.[19] Since MOFs are constructed of inorganic nodes connected by organic ligands, the reversible nature of such coordinating bonds prevented the chemical stability of the frameworks, especially when containing zinc clusters.[19] The discovery of UiO-66 MOF ($Zr_6(\mu_3\text{-}O)_4(\mu_3\text{-}OH)_4(BDC)_6$. BDC = benzene dicarboxylate), a framework containing a twelve-coordinated Zr cluster and exceptional hydrothermal stability (Figure 1.2),[20] allowed the future assembly of a variety of isoreticular Zr-MOFs (UiO MOFs series) that displayed high stability in water and in acidic pH.[20, 21]

The solvothermal synthesis of Zr-MOFs is usually achieved by modulated synthesis.[19, 22] This process consists of dissolving the organic ligand, the Zr precursor salt, and a modulator

molecule with similar chemical coordination functionality than the organic ligand, in a high boiling point solvent (usually) at temperatures around 80ºC - 120ºC.[20, 21] The main purpose of using a modulator is to control the coordination equilibrium between the ligands and the zirconium salt during the reaction. Therefore, regulating the rate of nucleation and growth of the MOF material.[22] The conditions employed during the modulated synthesis have a great impact on the crystallinity, particle size, and defectivity of UiO MOFs.[22]

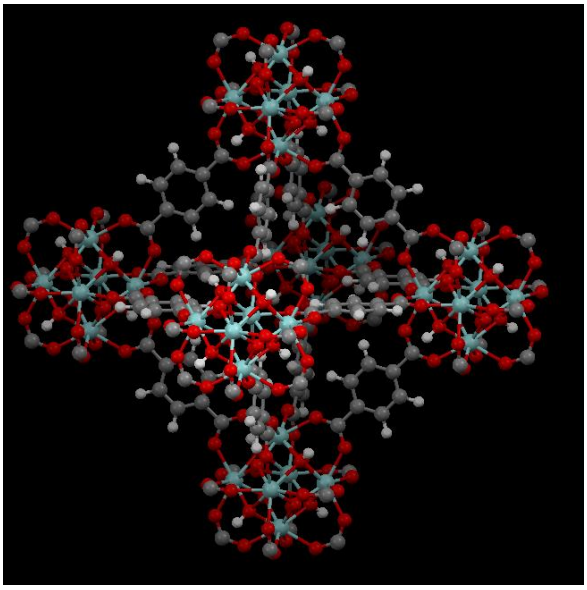

Figure 1.2 UiO-66 MOF ($Zr_6(\mu_3\text{-}O)_4(\mu_3\text{-}OH)_4(BDC)_6$. BDC = benzene dicarboxylate) crystal structure, indicating the octahedral cage of the framework. This image was created using the crystal structure reported in Reference 20.

The NU-1000 MOF is another Zr-MOF that not only displays chemical stability, but also has shown an excellent thermal stability.[23] One of the main characteristics of this framework is that its inorganic cluster contains open metal sites, allowing the introduction of extra ligands in their structure after the MOF has been assembled.[24, 25] This type of post synthetic process to modify the chemical structure of an existing MOF has been used widely,[26, 27] and constitutes one of the main strategies to append redox moieties into the core structure of MOF materials.[25, 28]

1.2.2 Synthesis of MOF thin films

The assembly of MOFs in conductive electrodes as thin films is one of the latest advances towards the application of MOFs in electronic technologies.[29] The main advantages of using MOF thin films in electrochemical analysis is that the MOF material is in direct contact with the electrolyte solution and that the material can be tested without the addition of other conductive materials, such as graphite.[30] The two main synthesis methods for MOF thin films are solvothermal synthesis and electrophoretic deposition: The solvothermal method consists on the spontaneous growth of the MOF in its crystalline form on the surface of a conductive material such as fluorinated tin oxide (FTO),[30] and the electrophoretic deposition involves creating a suspension of the MOF powder where two identical FTO slides facing each other and separated by 1 cm are immersed, and subjected to a DC voltage.[25]

1.3 MOFs in electrochemical systems

The possibility of generating materials capable of exhibiting both porosity and electrical conductivity has emerged as one of the most promising applications of MOFs[30-32] in order to possibly allow energy storage and conversion within these materials.[8] However, electrochemistry in MOFs is considered significantly complex since, in addition to the electron transfer process, insertion and ejection of ions must simultaneously take place into the framework and can affect the material's crystal lattice.[33] Three main experimental approaches have successfully enhanced the electrochemical activity in MOFs: The first is based on the redox behavior of the metal coordination center,[31, 34] the second involves charge transfer attributed to the organic linker,[35, 36] and the third relies in doping/mixing the MOF with conductive phases.[37]

One specific illustration of the latter approach was recently carried out when Alizarin red S (Scheme 1.1), a redox-active negatively charged material, was encapsulated in the redox-inactive MOF UMCM-1 (Figure 1.3A).[38] The electrochemical activity of this organic dye is attributed to its anthraquinone functionality that exhibits a pH dependent two-electron reduction mechanism (vide infra). Consequently, in a proton rich environment, two protons are consumed in addition to two electrons (Scheme 1.1a), and in alkaline media the two-electron reduction takes place without protonation (Scheme 1.1b).[8, 38]

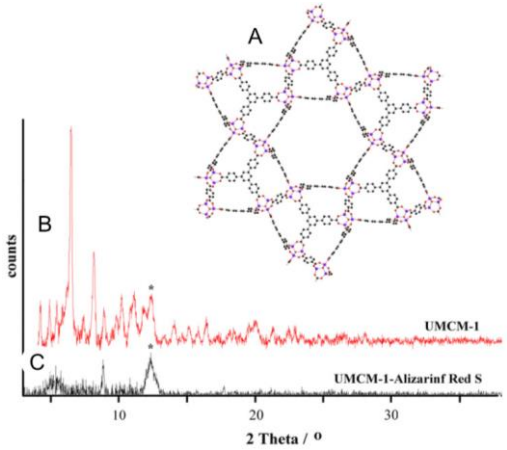

Figure 1.3 A) Molecular structure of UMCM-1 and Powder XRD pattern of B) UMCM-1 and (C) UMCM-1-Alizarin Red S powder. The symbol * denotes glass capillary background signals. This imaged was copied from Reference 38.

After alizarin red S was physisorbed in UMCM-1 (AR-UMCM-1), the original MOF structure experienced a loss of crystallinity as can be seen in Figure 1.3 B-C. Cyclic voltammetry studies of AR-UMCM-1 in ethanolic solution revealed two reduction waves at -0.2V and -1.2V, corresponding to the reduction reactions described in Scheme 1a and b, respectively (Figure 1.4A). Cyclic voltammograms obtained using a probe "collector-electrode", showed that reduced alizarin (*leuco*-alizarin) was released from the MOF to the solution, with a presumable degradation of the host framework (Figure 1.4B).[38] Apparently, when the proton consuming process described in

Scheme 1a occurs, the alkalinity within the MOF pores increases, leading mostly to reaction in Scheme 1b to takes place. Since this two-electron process is a non-charged balanced reaction, its product (*leuco*-alizarin) exhibits anion repulsion.[8] As a consequence, the necessity of stabilizing internal charge causes *leuco*-alizarin to be expulsed from the MOF pores.[8]

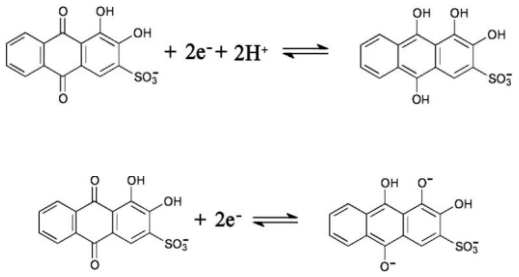

(a)

(b)

Scheme 1.1 a) Two-electron two-proton reduction of alizarin red S, b) Two-electron reduction of quinone in aqueous buffer. This image was copied from Reference 38.

Expelling anions from the framework is not the only possible disadvantage when impregnating MOFs with conductive phases. Other difficulties are the loss of porosity (Figure 1.3) as a result of pore filling and the fact that a substantial portion of the conductivity observed is due to the redox active guest rather than to the framework itself.[37] In this sense, incorporating redox active functionalities in the MOF structure by using electrochemically active and firmly attached organic linkers is a potential alternative to avoid the ion motion (ejection) observed in this case.[38]

Specifically, similar anthraquinone functionalities as the one observed in alizarin red S have only been built into a covalent organic framework (COF).[39] COFs are porous crystalline materials, assembled as polymer networks of light elements such as C, O or N, that are connected by covalent bonds. Figure 1.5 illustrates the structure of DAAQ-TFP COF, which is a β-ketoenamine-linked 2D COF, assembled from 2,6-diaminoanthraquinone (DAAQ). Cyclic voltammetry analysis of DAAQ showed the reduction of this compound to 9,10-

dihydroxyanthracene moieties by means of a two-electron two-proton reversible mechanism in a protic electrolyte (Figure 1.5).[39] Similarly, DAAQ-TFP COF also demonstrated reversible redox processes.[39]

Since the redox activity of the COF material is analogous to the anthraquinone subunit, the use of anthraquinone functionalities in MOFs emerges as a potential opportunity to synthesize electrochemically active porous materials. In particular, quinone-based ligands have served as an inspiration to the synthesis of COFs,[39, 40] and other MOFs that show potential applications in batteries and supercapacitors.[41-43] A positive performance of thin film electrodes has been recently observed in quinone-based COFs,[39, 40] where the assembly of two-dimensional frameworks in thin films provided more efficient quinone accessibility and capacitance as compared to randomly oriented slurry-modified electrodes.[5, 44] The electrochemical mechanism of quinone-hydroquinone systems is reviewed in detail in following sections.

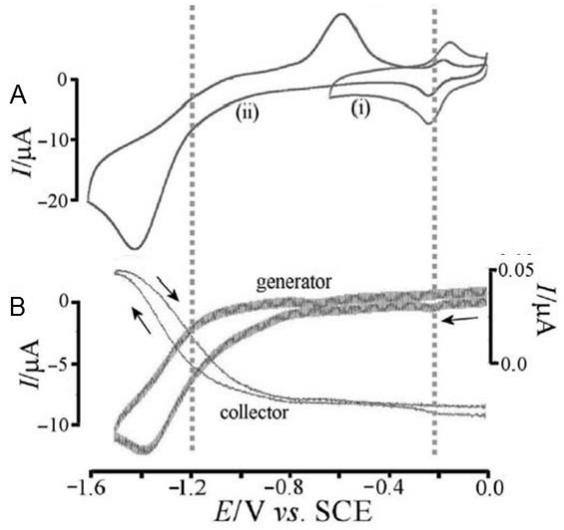

Figure 1.4 (A) Cyclic voltammogram for the reduction of immobilized UMCM-1-alizarin red S immersed in ethanol with 0.01 M NBu_4PF_6/1 mM $HClO_4$ (scan rate 0.05 V/s, cycle 4) , (B) Cyclic voltammogram (scan rate 0.01 V/s, second potential cycle) showing generator (4.9 mm diameter basal plane pyrolytic graphite) and collector (50 μm diameter platinum wire) data. This image was copied from Reference 38.

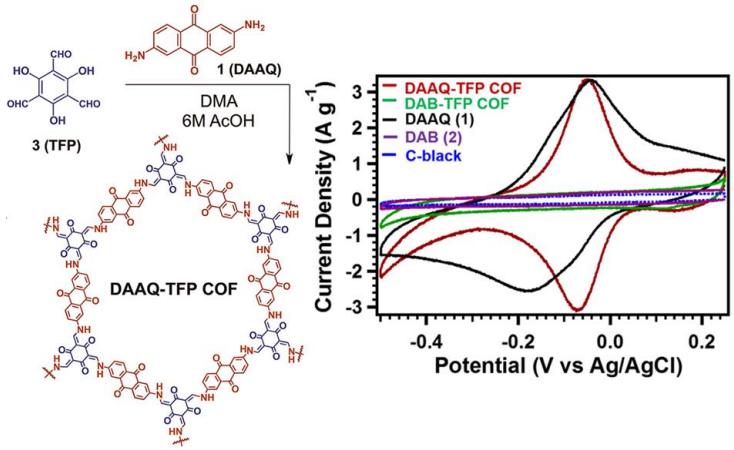

Figure 1.5 Left: Synthesis of DAAQ-TFP COF. Right: Cyclic voltammograms (50 mV/s, 1 M H_2SO_4 supporting electrolyte) of DAAQ-TFP COF (red), DAAQ monomer 1 (black), and carbon black-only (blue). This image was copied from Reference 39.

1.4 Electron Transport Mechanisms in MOFs

Although initially most MOFs were considered electrical insulators, in the recent years numerous examples of MOFs displaying the ability to transport electrical charge have been reported in the literature.[8, 31, 45] The structural design of MOF materials, where the desired electronic properties of both ligands and nodes are tuned in order to obtain specific characteristics in the synthesized MOFs, have led to some examples of MOFs containing charge transport pathways.[31, 45] The mechanisms of such pathways are described below:

1.4.1 Metal-ligand orbital overlap

One of the most inventive examples of charge transfer in MOFs, was based on the design of materials displaying metal-ligand orbital overlap (Figure 1.6).[46] Although charge transport is not favored in the majority of MOF materials, which contain coordination moieties containing oxygen or nitrogen atoms, attached to clusters of hard-metal ions; the introduction of other chemical species in the ligand (such as sulfur) creates a favorable pathway for charge transport.[46] In this particular example, the orbital overlap generated by the infinite Metal−Sulfur one-

dimensional chains displayed in the framework (denoted in purple on Figure 1.6), allowed the MOF material to exhibit high charge mobility, in the same order of magnitude than several organic semiconductors.[46]

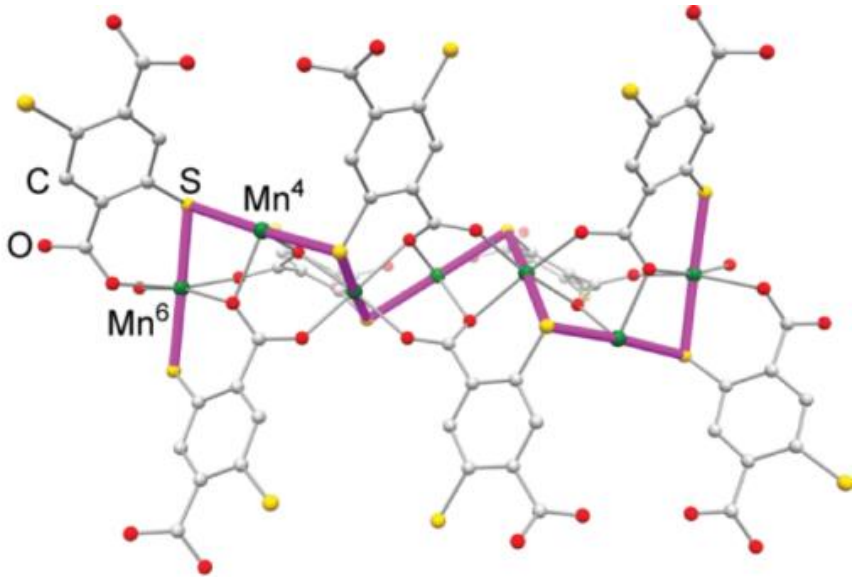

Figure 1.6 Metal-ligand overlap path for charge transport. This image was copied from Reference 46.

1.4.2 π-stacking interactions between electroactive ligands

The mechanism of charge transport by designing organic ligands containing conjugated systems, has also been reported as one of the methods for achieving charge transport in MOFs.[47] The first particular example of charge mobility due to π-stacking interactions between electroactive ligands involved the assembly of a zinc-based MOF containing tetrathiafulvalenetetrabenzoate (H_4TTFTB) linkers (Figure 1.7).[47] Although the framework displayed high intrinsic charge mobility due to the stacking of its individual building blocks,[47] the subsequent development of MOF thin films, allowed more detailed mechanistic studies of electron transport in MOF materials (redox hopping).[30]

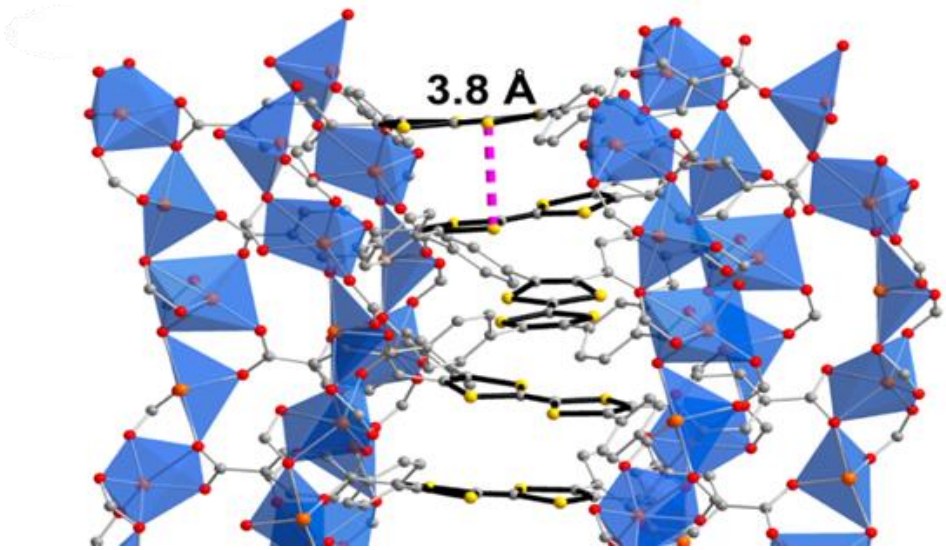

Figure 1.7 π-stacking interactions path for charge transport. This image was adapted from Reference 47.

1.4.3 Redox hopping

This electron-transport mechanism in MOFs was first demonstrated experimentally by both electrochemical and spectroelectrochemical analysis on a metalloporphyrin MOF thin film, CoPIZA/FTO.[30] Specifically, this framework contains large pores that allow unhindered access to its fixed redox centers. The electrochemical response observed in CV analysis, when applying a variety of different scan rates (10 mV/sec – 1000 mV/sec) revealed that this MOF film displayed nonzero, scan-rate dependent peak separation (ΔEp). Therefore, the CV response involved a diffusion-limited redox reaction equivalent to the one observed for redox centers diffusing freely in solution. This kind of behavior suggested that charge transport should occur via discrete ambipolar redox-hopping steps (Figure 1.8).[30] Once this mechanism was elucidated, the apparent diffusion coefficient (D_{app}) of this Co-based MOF thin films was quantified for the first time.[30]

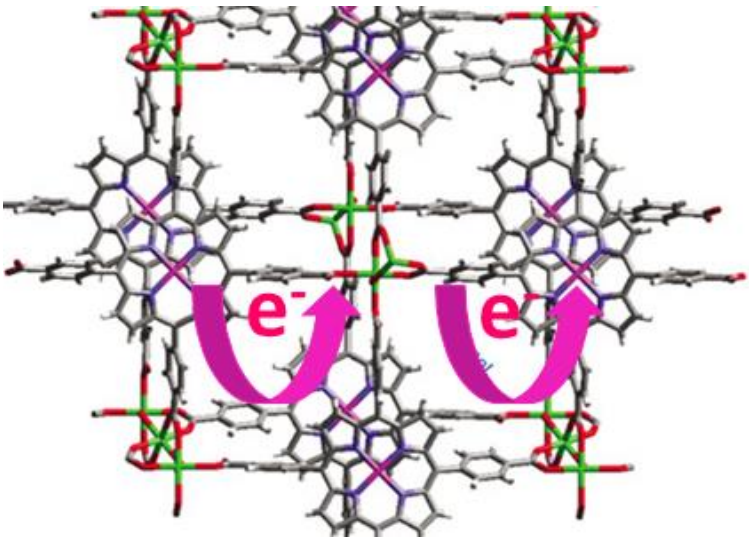

Figure 1.8 Redox-hopping electron transfer. This image was copied from Reference 30.

An important characteristic of the suggested redox hopping mechanism in MOFs, is the fact that the electrochemical charge transport should depend on the rate of electron diffusion (D_e) from one redox center to another, and the rate of ionic diffusion (D_i) through the MOF pores to satisfy the electroneutrality requirement.[30] Although there are no detailed reports examining such rates of diffusion in MOFs, a theoretical model capable of individually quantifying these diffusional components has been developed for immobilized microcrystals on the surface of an electrode.[48]. The application of the theoretical model to experimental MOF data is vital for the overall understanding of charge transport properties in MOFs, and constitutes one of the main objectives of the present study (Chapter 4).

1.5 Electrochemistry of Quinone-Hydroquinone Couples

Electrochemical reduction of quinones is probably one of the most illustrative examples of electron transfer reactions in organic redox systems. The importance of these compounds relies

mainly in their key function as proton-coupled electron transport agents in different biological processes such as photosynthesis and oxidative phosphorylation, as well as their proven medicinal activity in anticancer drugs.[49, 50] Several investigations about the redox behavior of quinones have been achieved and extended to contemporary studies using techniques such as cyclic voltammetry, pulse radiolysis, and electron spin resonance.[51, 52] Studies in different media allow for the description of the mechanism, kinetics, and potential pathways involved in quinones electrochemistry.[52]

1.5.1 Electrochemical reduction of quinones in aqueous media

1.5.1.1 Reduction of quinones in buffered aqueous media

It is well known that in buffered aqueous media, quinones undergo a reversible, single-step, two-electron reduction where the cathodic peak reduction potential (E_{pc}) varies with pH according to the Nernst equation.[52, 53] In acidic pH, this process is a two-proton two-electron reduction (Scheme 1.2a) where the slope of the linear relationship between E_{pc} and pH is approximately 60 mV/pH unit.[54] In basic pH, quinone is reduced to its quinone dianion Q^{2-} (Scheme 1.2c) in a two-electron transfer process,[50, 52] while at neutral pH, the reduction is either a one-proton two-electron transfer to form the protonated dianion QH^- (Scheme 1.2b) or a two electron transfer to form quinone dianion Q^{2-} (Scheme 1.2c).[50, 52]

In order to overcome the adsorption at the electrode surface displayed by carboxy-substituted 9,10-anthraquinones,[55, 56] anthraquinone-2-carboxylic acid (CAQ) have been studied using carbon paste electrodes finding a single and reversible reduction peak by cyclic voltammetry in aqueous buffer media (Figure 1.9A).[57] The $E_{1/2}$-pH diagram for this compound (Figure 1.9B) shows three different segments with slopes: -60.1 mV/pH (pH < 8.3), -27.5 mV/pH (8.3 > pH > 10.5), and -12.5 mV/pH (pH > 10.5), respectively. According to these slope values and using the

Nernst equation, the first process corresponds to a two-proton two-electron transfer to form the respective hydroquinone (H_2CAQ), the second chemical reaction is a two-electron one-proton transfer to form the correspondent protonated dianion ($HCAQ^-$), and the third segment involves a four-proton one-electron reactions of two quinone molecules to form both quinone dianion (CAQ^{2-}) and $HCAQ^-$.[57] The pK_a for the equilibrium between H_2CAQ and $HCAQ^-$ is 8.3, based on the intersection of the first and second segments previously described (Figure 1.9B).[57]

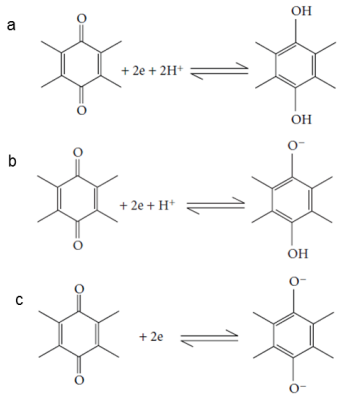

Scheme 1.2 a) Two-electron two-proton reduction of quinone in aqueous buffer b) Two-electron one-proton reduction of quinone in aqueous buffer c) Two-electron reduction of quinone in aqueous buffer. This image was copied from Reference 52.

The mixture of aqueous buffer solutions with small portions of organic solvents such as THF or DMF has also been used to address solubility issues in substituted 9,10-anthraquinones.[54, 58] For instance, the reduction of substituted 9,10-anthraquinones containing acetate groups were analyzed by cyclic voltammetry using a glassy carbon electrode in 50% aqueous buffer/THF mixtures.[54] The Nernstian variation of potential with pH consistent with a two-proton two-electron single step transfer was observed.[54]

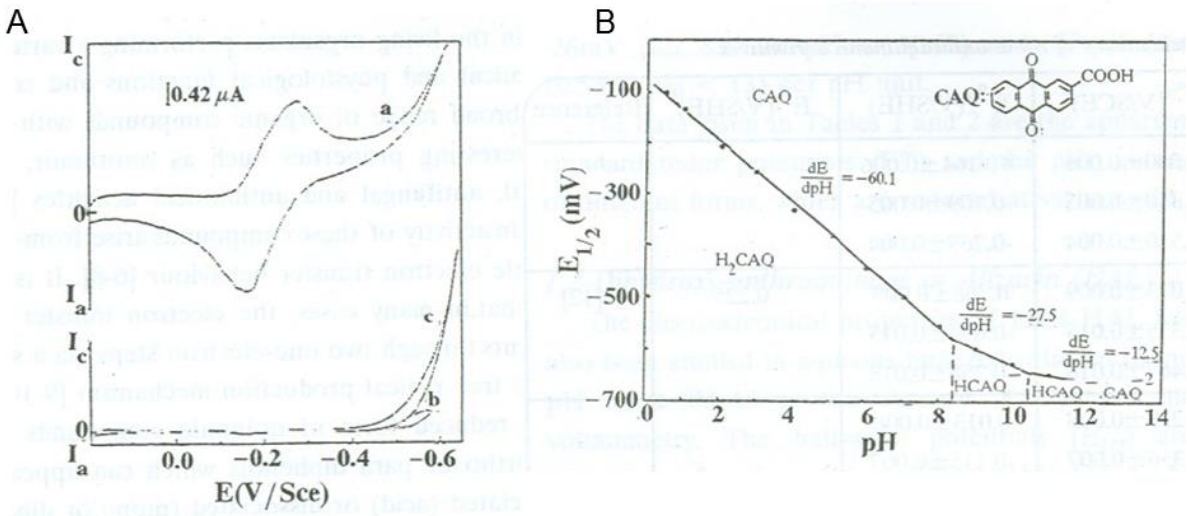

Figure 1.9 A) Cyclic voltammograms using the CPE of a) 1mM anthraquinone-2-carboxylic acid in aqueous buffer solution (pH=2.00), b) aqueous buffer solution (pH=2.00), and c) aqueous buffer solution (pH=2.00) in presence of dioxygen. Scan rate 50 mV/s and phosphate buffer supporting electrolyte. This image was copied from Reference 57.

1.5.1.2 Reduction of quinones in unbuffered aqueous media

The electrochemical reduction of quinones in aqueous media at acidic pH involves the consumption of protons and, therefore, the absence of buffer causes the pH at the electrode surface to be higher than the pH of the bulk solution.[59] This "effective pH" causes the reduction potentials to vary while the reduction takes place.[59] Indeed, this is the main reason for studying the electrochemical reduction of quinones in buffered aqueous solutions. In acidic unbuffered water, the typical two-proton two-electron transfer is observed.[59] However, when the concentration of protons in the media is less than the concentration of the quinone, the electrochemistry can be described as a single-step two-electron reduction to generate the strongly hydrogen-bonded quinone dianion. Because of the high basicity of this species, it exists in water as a mixture in equilibrium of protonation states (Q^{2-}, QH^-, and QH_2; Scheme 1.3).[59]

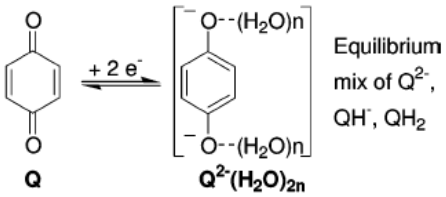

Scheme 1.3 Reduction of quinones in unbuffered aqueous media when [H+] < [Q]. This image was copied from Reference 59.

1.5.2 Electrochemistry of quinones in non-aqueous media

1.5.2.1 Reduction of quinones in neutral aprotic media

The reduction of quinones in aprotic solvents involves the generation of two different cathodic waves, corresponding to two consecutive one-electron reduction steps to produce semiquinone ($Q^{\cdot-}$) and quinone dianion (Q^{2-}), respectively (Scheme 1.4).[60] Electron spin resonance has been used to determine the presence of these radicals.[61] Generally, the first reduction step is entirely reversible while the second one is quasireversible (Figure1.10a).[60] In both reduction steps, current is controlled by the diffusion of species to the electrode and, therefore, the peak current is directly proportional to the square root of the scan rate.[60] The semiquinone has a short life-time and rapidly undergoes disproportionation to form the quinone and the quinone dianion.[52]

$$Q + e \rightarrow Q^{\cdot-}$$
$$Q^{\cdot-} + e \rightarrow Q^{2-}$$

Scheme 1.4 EE mechanism for the electrochemical reduction of quinones in neutral aprotic media ($Q^{\cdot-}$, semiquinone; Q^{2-}, quinone dianion).

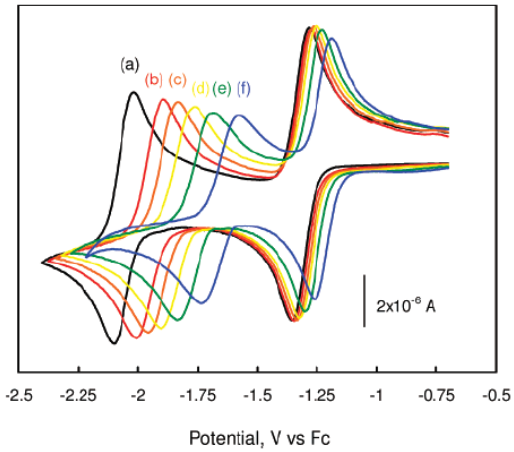

Figure 1.10 CVs of anthraquinone in 0.1 M NBu_4PF_6 in DMF after addition of water: (a) 0% H_2O, (b) 0.5% H_2O, (c) 1% H_2O, (d) 2% H_2O, (e) 4% H_2O, (f) 8% H_2O. Scan rate 100 mV/s with a Au working electrode. This image was copied from Reference 59.

1.5.2.2 The role of protonation and hydrogen bonding

Although the two waves are usually separated by approximately 0.7 V, the potentials strongly depend on the stability of the reduced species.[60] For instance, in hydroxy-substituted anthraquinones both semiquinone and quinone dianion can be strongly stabilized by intramolecular hydrogen bonding between the negatively-charged quinone oxygen and the hydroxylic proton.[62] As a consequence, the reduction potentials of selected 9,10-anthraquinones with hydroxy substituents in the positions 1,4,5- and 8- showed a positive shift in their reduction potentials of approximately +209 mV for the first reduction potential (E°' for $Q / Q^{\cdot-}$) and +291 mV for the second reduction potential (E°' for $Q / Q^{\cdot-}$).[62] From an electrostatic point of view this behavior is reasonable, since it should be harder to add an electron to a species that is already negatively charged and as a result once quinone radicals are stabilized by intramolecular hydrogen bonding, less potential is required to achieve electron transfer from the electrode to the compound.

Addition of hydrogen bonding agents has strong influence on the reduction potentials of quinones in neutral aprotic media.[52, 59] The addition of water to a DMF solution containing

anthraquinone causes the second reduction potential to move in a positive direction (Figure 1.10).[59] The first reduction wave also moves positively but less in extent. Therefore, sufficient addition of water causes the two waves to merge together. This effect was initially explained as protonation of the quinone dianion by water[63] but further studies revealed that hydrogen bonding was more likely the reason of the positive shift in the second reduction wave.[64] The analysis was based on the Born equation:

$$\Delta_{solv}G^{\ominus} = -\frac{N_A z^2 e^2}{8\pi\varepsilon_0 r}\left(1-\frac{1}{\varepsilon_r}\right) \qquad \text{Eq. (1.1)}$$

where *e* is the electronic charge, *N* is the Avogadro's number, ε is the diaelectric constant of the medium and *r* is the radius of the ion. The latter equation predicts that the positive shift of the reduction potential from the neutral quinone to the anion is higher in the solvent with the largest diaelectric constant. However, experimental data of anthraquinone, in a DMF-Ethanol system, revealed that the larger positive shift of the reduction potential was observed while increasing the concentration of the solvent with the lower diaelectric constant (ethanol, ε=24.3) in a solution of DMF(ε=36.7).[64] As a result, the positive shift of potentials is favorably interpreted by hydrogen-bond interactions of the produced semiquinone and quinone dianion with water or alcohol.[64]

Since the positive shift is more significant in the second reduction wave, quinone dianion undergoes stronger hydrogen-bonding interactions than semiquinone.[64] The number of hydrogen bonds per quinone ion is calculated in several studies based on the magnitude of the potential shift and the concentration of the hydrogen-bond donor agent.[65] The effect of hydrogen bonding can be clearly distinguished from that of protonation by analyzing the pK_a values of the species involved,

the dielectric constants of the solvents, the extent of the potential shifts and the reversibility observed in the cyclic voltammograms.[60]

1.6 References

1. Kimizuka, N. Towards Self-Assembling Inorganic Molecular Wires. *Advanced Materials* **2000,** 12 (19), 1461-1463 DOI: 10.1002/1521-4095(200010)12:19<1461::AID-ADMA1461>3.0.CO;2-X.

2. Sheberla, D.; Bachman, J. C.; Elias, J. S.; Sun, C.-J.; Shao-Horn, Y.; Dincă, M. Conductive MOF electrodes for stable supercapacitors with high areal capacitance. *Nature Materials* **2016,** 16, 220 DOI: 10.1038/nmat4766 https://www.nature.com/articles/nmat4766#supplementary-information.

3. Larcher, D.; Tarascon, J. M. Towards greener and more sustainable batteries for electrical energy storage. *Nature chemistry* **2015,** 7 (1), 19-29 DOI: 10.1038/nchem.2085.

4. Xu, G.; Nie, P.; Dou, H.; Ding, B.; Li, L.; Zhang, X. Exploring metal organic frameworks for energy storage in batteries and supercapacitors. *Materials Today* **2017,** 20 (4), 191-209 DOI: https://doi.org/10.1016/j.mattod.2016.10.003.

5. DeBlase, C. R.; Hernández-Burgos, K.; Silberstein, K. E.; Rodríguez-Calero, G. G.; Bisbey, R. P.; Abruña, H. D.; Dichtel, W. R. Rapid and Efficient Redox Processes within 2D Covalent Organic Framework Thin Films. *ACS Nano* **2015,** 9 (3), 3178-3183 DOI: 10.1021/acsnano.5b00184.

6. Allendorf, M. D.; Schwartzberg, A.; Stavila, V.; Talin, A. A. A roadmap to implementing metal-organic frameworks in electronic devices: challenges and critical directions. *Chemistry* **2011,** 17 (41), 11372-88 DOI: 10.1002/chem.201101595.

7. Wang, G.; Zhang, L.; Zhang, J. A review of electrode materials for electrochemical supercapacitors. *Chemical Society Reviews* **2012,** 41 (2), 797-828 DOI: 10.1039/C1CS15060J.

8. Halls, J. E.; Jiang, D.; Burrows, A. D.; Kulandainathan, M. A.; Marken, F. In *Electrochemistry: Volume 12*; The Royal Society of Chemistry: 2014; Vol. 12, pp 187-210.

9. Yaghi, O. M.; O'Keeffe, M.; Kanatzidis, M. Design of Solids from Molecular Building Blocks: Golden Opportunities for Solid State Chemistry. *Journal of Solid State Chemistry* **2000,** 152 (1), 1-2.

10. Tranchemontagne, D. J.; Ni, Z.; O'Keeffe, M.; Yaghi, O. M. ChemInform Abstract: Reticular Chemistry of Metal—Organic Polyhedra. *ChemInform* **2008,** 39 (40), no-no DOI: 10.1002/chin.200840226.

11. Dang, D.; Wu, P.; He, C.; Xie, Z.; Duan, C. Homochiral Metal−Organic Frameworks for Heterogeneous Asymmetric Catalysis. *Journal of the American Chemical Society* **2010,** 132 (41), 14321-14323 DOI: 10.1021/ja101208s.

12. Yaghi, O. M.; O'Keeffe, M.; Ockwig, N. W.; Chae, H. K.; Eddaoudi, M.; Kim, J. Reticular synthesis and the design of new materials. *Nature* **2003,** 423 (6941).

13. Li, H. E., Mohamed; O'Keeffe, M; Yaghi, O. M. Design and synthesis of an exceptionally stable and highly porous metal-organic framework. *Nature* **1999,** 402 (6759), 276-279.

14. Nijkamp, M. G.; Raaymakers, J. E. M. J.; van Dillen, A. J.; de Jong, K. P. Hydrogen storage using physisorption – materials demands. *Appl Phys A* **2001,** 72 (5), 619-623 DOI: 10.1007/s003390100847.

15. Chester, A. W.; Clement, C. P.; Han, S., Faujasite zeolitic materials. In Google Patents: 2000.

16. Davis, M. E. Ordered porous materials for emerging applications. *Nature* **2002,** 417 (6891), 813-21.

17. Farha, O. K.; Eryazici, I.; Jeong, N. C.; Hauser, B. G.; Wilmer, C. E.; Sarjeant, A. A.; Snurr, R. Q.; Nguyen, S. T.; Yazaydın, A. Ö.; Hupp, J. T. Metal–Organic Framework Materials with Ultrahigh Surface Areas: Is the Sky the Limit? *Journal of the American Chemical Society* **2012,** 134 (36), 15016-15021 DOI: 10.1021/ja3055639.

18. Murray, L. J.; Dinca, M.; Long, J. R. Hydrogen storage in metal-organic frameworks. *Chemical Society Reviews* **2009,** 38 (5), 1294-1314 DOI: 10.1039/b802256a.

19. Bai, Y.; Dou, Y.; Xie, L.-H.; Rutledge, W.; Li, J.-R.; Zhou, H.-C. Zr-based metal-organic frameworks: design, synthesis, structure, and applications. *Chem. Soc. Rev.* **2016,** 45 (8), 2327-2367 DOI: 10.1039/C5CS00837A.

20. Cavka, J. H.; Jakobsen, S.; Olsbye, U.; Guillou, N.; Lamberti, C.; Bordiga, S.; Lillerud, K. P. A New Zirconium Inorganic Building Brick Forming Metal Organic Frameworks with Exceptional Stability. *Journal of the American Chemical Society* **2008,** 130 (42), 13850-13851 DOI: 10.1021/ja8057953.

21. DeCoste, J. B.; Peterson, G. W.; Jasuja, H.; Glover, T. G.; Huang, Y.-g.; Walton, K. S. Stability and degradation mechanisms of metal-organic frameworks containing the Zr6O4(OH)4 secondary building unit. *Journal of Materials Chemistry A* **2013,** 1 (18), 5642-5650 DOI: 10.1039/C3TA10662D.

22. Shearer, G. C.; Chavan, S.; Bordiga, S.; Svelle, S.; Olsbye, U.; Lillerud, K. P. Defect Engineering: Tuning the Porosity and Composition of the Metal–Organic Framework UiO-66 via Modulated Synthesis. *Chemistry of Materials* **2016,** 28 (11), 3749-3761 DOI: 10.1021/acs.chemmater.6b00602.

23. Wang, T. C.; Vermeulen, N. A.; Kim, I. S.; Martinson, A. B. F.; Stoddart, J. F.; Hupp, J. T.; Farha, O. K. Scalable synthesis and post-modification of a mesoporous metal-organic framework called NU-1000. *Nature Protocols* **2015,** 11, 149 DOI: 10.1038/nprot.2016.001.

24. Deria, P.; Bury, W.; Hupp, J. T.; Farha, O. K. Versatile functionalization of the NU-1000 platform by solvent-assisted ligand incorporation. *Chem. Commun.* **2014,** 50 (16), 1965-1968 DOI: 10.1039/C3CC48562E.

25. Hod, I.; Bury, W.; Gardner, D. M.; Deria, P.; Roznyatovskiy, V.; Wasielewski, M. R.; Farha, O. K.; Hupp, J. T. Bias-Switchable Permselectivity and Redox Catalytic Activity of a Ferrocene-Functionalized, Thin-Film Metal–Organic Framework Compound. *The Journal of Physical Chemistry Letters* **2015,** 6 (4), 586-591 DOI: 10.1021/acs.jpclett.5b00019.

26. Marshall, R. J.; Forgan, R. S. Postsynthetic Modification of Zirconium Metal-Organic Frameworks. *European Journal of Inorganic Chemistry* **2016,** 2016 (27), 4310-4331 DOI: 10.1002/ejic.201600394.

27. Lin, S.; Pineda-Galvan, Y.; Maza, W. A.; Epley, C. C.; Zhu, J.; Kessinger, M. C.; Pushkar, Y.; Morris, A. J. Electrochemical Water Oxidation by a Catalyst-Modified Metal–Organic Framework Thin Film. *ChemSusChem* **2017,** 10 (3), 514-522 DOI: 10.1002/cssc.201601181.

28. Hod, I.; Farha, O. K.; Hupp, J. T. Modulating the rate of charge transport in a metal-organic framework thin film using host:guest chemistry. *Chemical Communications* **2016,** 52 (8), 1705-1708 DOI: 10.1039/C5CC09695B.

29. Liu, J.; Woll, C. Surface-supported metal-organic framework thin films: fabrication methods, applications, and challenges. *Chemical Society Reviews* **2017,** 46 (19), 5730-5770 DOI: 10.1039/C7CS00315C.

30. Ahrenholtz, S. R.; Epley, C. C.; Morris, A. J. Solvothermal Preparation of an Electrocatalytic Metalloporphyrin MOF Thin Film and its Redox Hopping Charge-Transfer Mechanism. *Journal of the American Chemical Society* **2014,** 136 (6), 2464-2472 DOI: 10.1021/ja410684q.

31. Kobayashi, Y.; Jacobs, B.; Allendorf, M. D.; Long, J. R. Conductivity, Doping, and Redox Chemistry of a Microporous Dithiolene-Based Metal−Organic Framework. *Chemistry of Materials* **2010,** 22 (14), 4120-4122 DOI: 10.1021/cm101238m.

32. Morozan, A.; Jaouen, F. Metal organic frameworks for electrochemical applications. *Energy & Environmental Science* **2012,** 5 (11), 9269-9290 DOI: 10.1039/c2ee22989g.

33. Millward, R. C.; Madden, C. E.; Sutherland, I.; Mortimer, R. J.; Fletcher, S.; Marken, F. Directed assembly of multilayers - the case of Prussian Blue. *Chemical Communications* **2001,** (19), 1994-1995 DOI: 10.1039/b106616c.

34. Lin, H.; Wang, X.; Hu, H.; Chen, B.; Liu, G. A novel copper(II) complex constructed with mixed ligands of biphenyl-4,4′-dicarboxylic acid (H2bpdc) and dipyrido[3,2-d:2′,3′-f]quinoxaline (Dpq): Synthesis, structure, electrochemistry and electrocatalysis. *Solid State Sciences* **2009,** 11 (3), 643-650 DOI: http://dx.doi.org/10.1016/j.solidstatesciences.2008.10.007.

35. Nguyen, T. L. A.; Devic, T.; Mialane, P.; Rivière, E.; Sonnauer, A.; Stock, N.; Demir-Cakan, R.; Morcrette, M.; Livage, C.; Marrot, J. r.; Tarascon, J.-M.; Férey, G. r. Reinvestigation of the MII (M = Ni, Co)/TetraThiafulvaleneTetraCarboxylate System Using High-Throughput Methods: Isolation of a Molecular Complex and Its Single-Crystal-to-Single-Crystal Transformation to a Two-Dimensional Coordination Polymer. *Inorganic Chemistry* **2010,** 49 (22), 10710-10717 DOI: 10.1021/ic101906u.

36. Behera, J. N.; D'Alessandro, D. M.; Soheilnia, N.; Long, J. R. Synthesis and Characterization of Ruthenium and Iron−Ruthenium Prussian Blue Analogues. *Chemistry of Materials* **2009,** 21 (9), 1922-1926 DOI: 10.1021/cm900230p.

37. Zeng, M.-H.; Wang, Q.-X.; Tan, Y.-X.; Hu, S.; Zhao, H.-X.; Long, L.-S.; Kurmoo, M. Rigid Pillars and Double Walls in a Porous Metal-Organic Framework: Single-Crystal to Single-Crystal, Controlled Uptake and Release of Iodine and Electrical Conductivity. *Journal of the American Chemical Society* **2010,** 132 (8), 2561-2563 DOI: 10.1021/ja908293n.

38. Halls, J. E.; Ahn, S. D.; Jiang, D.; Keenan, L. L.; Burrows, A. D.; Marken, F. Proton uptake vs. redox driven release from metal–organic-frameworks: Alizarin red S reactivity in UMCM-1. *Journal of Electroanalytical Chemistry* **2013,** 689, 168-175 DOI: http://dx.doi.org/10.1016/j.jelechem.2012.11.016.

39. DeBlase, C. R.; Silberstein, K. E.; Truong, T.-T.; Abruña, H. D.; Dichtel, W. R. β-Ketoenamine-Linked Covalent Organic Frameworks Capable of Pseudocapacitive Energy Storage. *Journal of the American Chemical Society* **2013,** 135 (45), 16821-16824 DOI: 10.1021/ja409421d.

40. Chandra, S.; Roy Chowdhury, D.; Addicoat, M.; Heine, T.; Paul, A.; Banerjee, R. Molecular Level Control of the Capacitance of Two-Dimensional Covalent Organic Frameworks: Role of Hydrogen Bonding in Energy Storage Materials. *Chemistry of Materials* **2017,** 29 (5), 2074-2080 DOI: 10.1021/acs.chemmater.6b04178.

41. Gui, B.; Meng, X.; Chen, Y.; Tian, J.; Liu, G.; Shen, C.; Zeller, M.; Yuan, D.; Wang, C. Reversible Tuning Hydroquinone/Quinone Reaction in Metal–Organic Framework: Immobilized Molecular Switches in Solid State. *Chemistry of Materials* **2015,** 27 (18), 6426-6431 DOI: 10.1021/acs.chemmater.5b02648.

42. Zhang, Z.; Yoshikawa, H.; Awaga, K. Monitoring the Solid-State Electrochemistry of Cu(2,7-AQDC) (AQDC = Anthraquinone Dicarboxylate) in a Lithium Battery: Coexistence of Metal and Ligand Redox Activities in a Metal–Organic Framework. *Journal of the American Chemical Society* **2014,** 136 (46), 16112-16115 DOI: 10.1021/ja508197w.

43. Zhang, Z.; Yoshikawa, H.; Awaga, K. Discovery of a "Bipolar Charging" Mechanism in the Solid-State Electrochemical Process of a Flexible Metal–Organic Framework. *Chemistry of Materials* **2016,** 28 (5), 1298-1303 DOI: 10.1021/acs.chemmater.5b04075.

44. Mulzer, C. R.; Shen, L.; Bisbey, R. P.; McKone, J. R.; Zhang, N.; Abruña, H. D.; Dichtel, W. R. Superior Charge Storage and Power Density of a Conducting Polymer-Modified Covalent Organic Framework. *ACS Central Science* **2016,** 2 (9), 667-673 DOI: 10.1021/acscentsci.6b00220.

45. Gándara, F.; Uribe-Romo, F. J.; Britt, D. K.; Furukawa, H.; Lei, L.; Cheng, R.; Duan, X.; O'Keeffe, M.; Yaghi, O. M. Porous, Conductive Metal-Triazolates and Their Structural Elucidation by the Charge-Flipping Method. *Chemistry – A European Journal* **2012,** 18 (34), 10595-10601 DOI: 10.1002/chem.201103433.

46. Sun, L.; Miyakai, T.; Seki, S.; Dincă, M. Mn2(2,5-disulfhydrylbenzene-1,4-dicarboxylate): A Microporous Metal–Organic Framework with Infinite (−Mn–S−)∞ Chains and High Intrinsic Charge Mobility. *Journal of the American Chemical Society* **2013,** 135 (22), 8185-8188 DOI: 10.1021/ja4037516.

47. Narayan, T. C.; Miyakai, T.; Seki, S.; Dincă, M. High Charge Mobility in a Tetrathiafulvalene-Based Microporous Metal–Organic Framework. *Journal of the American Chemical Society* **2012,** 134 (31), 12932-12935 DOI: 10.1021/ja3059827.

48. Schröder, U.; Oldham, K. B.; Myland, J. C.; Mahon, P. J.; Scholz, F. Modelling of solid state voltammetry of immobilized microcrystals assuming an initiation of the electrochemical reaction at a three-phase junction. *Journal of Solid State Electrochemistry* **2000,** 4 (6), 314-324 DOI: 10.1007/s100080000130.

49. Aguilar-Martinez, M.; Macias-Ruvalcaba, N. A.; Bautista-Martinez, J. A.; Gomez, M.; Gonzalez, F. J.; Gonzalez, I. Review: Hydrogen Bond and Protonation as Modifying Factors of the Quinone Reactivity. *Current Organic Chemistry* **2004,** 8 (17), 1721-1738 DOI: 10.2174/1385272043369548.

50. Guin, P. S.; Das, S.; Mandal, P. C. Sodium 1, 4-dihydroxy-9, 10-anthraquinone- 2-sulphonate interacts with calf thymus DNA in a way that mimics anthracycline antibiotics: an

electrochemical and spectroscopic study. *Journal of Physical Organic Chemistry* **2010,** 23 (6), 477-482 DOI: 10.1002/poc.1624.

51. Fieser, L. F. THE TAUTOMERISM OF HYDROXY QUINONES. *Journal of the American Chemical Society* **1928,** 50 (2), 439-465 DOI: 10.1021/ja01389a033.

52. Guin, P. S.; Das, S.; Mandal, P. C. Electrochemical Reduction of Quinones in Different Media: A Review. *International Journal of Electrochemistry* **2011,** 2011, DOI: 10.4061/2011/816202.

53. He, P.; Crooks, R. M.; Faulkner, L. R. Adsorption and electrode reactions of disulfonated anthraquinones at mercury electrodes. *The Journal of Physical Chemistry* **1990,** 94 (3), 1135-1141 DOI: 10.1021/j100366a023.

54. Blankespoor, R. L.; Hsung, R.; Schutt, D. L. Electroreductive cleavage of substituted 9,10-anthraquinones in 50% aqueous THF buffers: a pH-dependent process. *The Journal of Organic Chemistry* **1988,** 53 (13), 3032-3035 DOI: 10.1021/jo00248a024.

55. Han, S. W.; Ha, T. H.; Kim, C. H.; Kim, K. Self-Assembly of Anthraquinone-2-carboxylic Acid on Silver: Fourier Transform Infrared Spectroscopy, Ellipsometry, Quartz Crystal Microbalance, and Atomic Force Microscopy Study. *Langmuir* **1998,** 14 (21), 6113-6120 DOI: 10.1021/la980259j.

56. Osawa, M.; Ataka, K.-i.; Yoshii, K.; Yotsuyanagi, T. Surface-enhanced infrared ATR spectroscopy for in situ studies of electrode/electrolyte interfaces. *Journal of Electron Spectroscopy and Related Phenomena* **1993,** 64–65 (0), 371-379 DOI: http://dx.doi.org/10.1016/0368-2048(93)80099-8.

57. Ojani, R. R., Jahanbakhsh and Ebrahimi, Manochehr. A Cyclic Voltammetric Study of the Aqueous Electrochemistry of Some Anthraquinone Derivatives on Carbon Paste Electrode. *Iran. J. Chem. & Chem. Eng.* **2001,** 20 (2).

58. Partha Sarathi Guin, S. D., P. C. Mandal. Electrochemical Reduction of Sodium 1,4-dihydroxy-9,10-anthraquinone-2-sulphonate in Aqueous and Aqueous Dimethyl Formamide Mixed Solvent: A Cyclic Voltammetric Study. *Int. J. Electrochem. Sci* **2008,** 3, 1016 - 1028

59. Quan, M.; Sanchez, D.; Wasylkiw, M. F.; Smith, D. K. Voltammetry of Quinones in Unbuffered Aqueous Solution: Reassessing the Roles of Proton Transfer and Hydrogen Bonding in the Aqueous Electrochemistry of Quinones. *Journal of the American Chemical Society* **2007,** 129 (42), 12847-12856 DOI: 10.1021/ja0743083.

60. Gupta, N.; Linschitz, H. Hydrogen-Bonding and Protonation Effects in Electrochemistry of Quinones in Aprotic Solvents. *Journal of the American Chemical Society* **1997,** 119 (27), 6384-6391 DOI: 10.1021/ja970028j.

61. Meisel, D.; Czapski, G. One-electron transfer equilibriums and redox potentials of radicals studied by pulse radiolysis. *The Journal of Physical Chemistry* **1975,** 79 (15), 1503-1509 DOI: 10.1021/j100582a004.

62. Ashnagar, A.; Bruce, J. M.; Dutton, P. L.; Prince, R. C. One- and two-electron reduction of hydroxy-1,4-naphthoquinones and hydroxy-9,10-anthraquinones. The role of internal hydrogen bonding and its bearing on the redox chemistry of the anthracycline antitumour quinones. *Biochim Biophys Acta* **1984,** 801 (3), 351-9.

63. Peover, M. E. 879. A polarographic investigation into the redox behaviour of quinones: the roles of electron affinity and solvent. *Journal of the Chemical Society (Resumed)* **1962,** (0), 4540-4549 DOI: 10.1039/jr9620004540.

64. Hayano, S.; Fujihira, M. The Effect of Water on the Reduction Potentials of Some Aromatic Compounds in the DMF-Water System. *Bulletin of the Chemical Society of Japan* **1971,** 44 (8), 2051-2055 DOI: 10.1246/bcsj.44.2051.

65. Olmstead, W. N.; Margolin, Z.; Bordwell, F. G. Acidities of water and simple alcohols in dimethyl sulfoxide solution. *The Journal of Organic Chemistry* **1980,** 45 (16), 3295-3299 DOI: 10.1021/jo01304a032.

2. Proton-Coupled Electron Transport in Anthraquinone-based Zirconium Metal-Organic Frameworks

This chapter has been adapted from a published manuscript Paula J. Celis-Salazar, Charity C. Epley, Spencer R. Ahrenholtz, William A. Maza, Pavel M. Usov, Amanda J. Morris from the following reference: *Inorganic Chemisry*, **2017**, 56, 22, 13741-13747. Reprinted with permission from the American Chemical Society copyright © 2017.

2.1 ABSTRACT

The ditopic ligands, 2,6-dicarboxy-9,10-anthraquinone and 1,4-dicarboxy-9,10-anthraquinone were used to synthesize two new UiO-type metal-organic frameworks (2,6-Zr-AQ-MOF and 1,4-Zr-AQ-MOF, respectively). The Pourbaix diagrams (E vs. pH) of the MOFs and their ligands were constructed using cyclic voltammetry in aqueous buffered media. The MOFs exhibit chemical stability and undergo diverse electrochemical processes, where the number of electrons and protons transferred was tailored in a Nernstian manner by the pH of the media. Both the 2,6-Zr-AQ-MOF and its ligand reveal a similar electrochemical pKa value (7.56 and 7.35, respectively) for the transition between a two-electron, two-proton transfer (at pH < pKa) and a two-electron, one-proton transfer (at pH > pKa). In contrast, the position of the quinone moiety with respect to the zirconium node, the effect of hydrogen bonding, and the amount of defects in 1,4-Zr-AQ-MOF, lead to the transition from a two-electron, three-proton transfer to a two-electron, one-proton transfer. The pKa of this framework (5.18) is analogous to one of the three electrochemical pKa values displayed by its ligand (3.91, 5.46, and 8.80), which also showed

intramolecular hydrogen bonding. The ability of the MOFs to tailor discrete numbers of protons and electrons, suggests their application as charge carriers in electronic devices.

2.2 INTRODUCTION

The application of metal-organic frameworks (MOFs) as active materials in electronic devices has been proposed as a suitable alternative to achieve efficient charge storage and energy conversion.[1] The characteristic synthetic tunability, high permanent porosity, and structural uniformity of MOFs position these materials as prospective candidates for assembling high surface electrodes containing well-organized redox moieties that are capable to store electricity.[2] In particular, the ability of MOFs to undergo electron transport has been achieved through three different synthetic approaches: 1) charge transfer through metal-ligand orbital overlap,[3] 2) π-stacking interactions between electroactive ligands within the framework[4] and 3) redox hopping.[5] Nevertheless, the synthetic design of MOFs that exhibit proton-coupled electron transport (PCET) remains in its early stages. The two main necessities are the ability to facilitate high electron and proton conduction and a high water stability over a range of pH.

One way to address these requirements is to integrate ligands capable of undergoing PCET into isoreticular arrays of highly stable MOFs, such as the UiO-series. These zirconium-based MOFs have demonstrated an exceptional stability in water and in acidic pH.[6, 7] Similarly, quinone ligands are recognized as excellent PCET agents, since they play an important role in biochemical processes, including photosynthesis and oxidative phosphorylation.[8] The redox chemistry of quinones is strongly influenced by the pH of the media. Generally, at acidic pH, the quinone (Q) reduction is a single-step, two-electron, two-proton process which generates the respective hydroquinone (QH_2).[9] At alkaline pH, the concentration of protons is too low to support PCET,

therefore the redox process is a two-electron transfer to form the dianion (Q^{2-}).[9] At neutral pH, the quinone can undergo either a two-electron, one-proton process resulting in the protonated dianion specie (QH^-), or alternatively it could lead to the formation of the dianion (SI, Scheme S2).[9] The electrochemical pKa values of the different redox and protonation states of quinone species can be represented using a potential (E) vs. pH plot (Pourbaix diagram).

Quinone-based ligands have served as an inspiration to the synthesis of covalent-organic frameworks (COFs)[10, 11] and other MOFs that show potential applications in batteries and supercapacitors.[12-14] However, understanding the effect of local pH in the pore environment of these frameworks remains vague. A hitherto study of the reduction of MOF UMCM-1 containing a nanoconfined anthraquinone molecule (Alizarin red S) in its pores showed that a typical two-electron, two-proton process at acidic pH was experienced only in anthraquinone molecules located at the MOF surface.[15, 16] In contrast, the deficiency of protons inside the MOF pores created a local alkaline environment during the two-electron reduction that led to the formation of the negatively charged dianion, which was ejected from the framework in order to stabilize internal charge.[15, 16]

Furthermore, the protonation state of the zirconium nodes of UiO-MOFs is also directly influenced by the local pH.[17] As a result, assembling these frameworks with ligands that exhibit quinone moieties in the proximity of the zirconium cluster may result in the occurrence of other complex processes, such as hydrogen bonding or linker-to-node proton transfer. Additionally, the pore size and the amount of defects (missing ligands) in the framework may play an important role in the transport of protons within the MOF pores. In order to elucidate these factors, we sought to study the effect of applied potential and pH on the equilibrium between different quinone species in these materials, where the specific number of protons and electrons transferred can be

accounted. Herein, we report the first example of Pourbaix diagrams for two different anthraquinone-based zirconium MOFs that exhibit diverse electrochemical response in aqueous electrolytes due to the positioning of the quinone moiety with respect to the zirconium node, the amount of defects, and the pore size. To the best of our knowledge, these types of studies have not been performed on redox-active frameworks to date. These results demonstrate the potential of MOFs to be employed as proton-electron carriers in energy transport systems.

2.3 EXPERIMENTAL SECTION

2.3.1 Synthesis of 2,6-dicarboxy-9,10-anthhraquinone (1)

The synthesis of **1** was achieved in two steps by adapting previous procedures described in the literature (**Scheme S2.1**).[18, 19] Benzoquinone (3.25 g, 30 mmol), isoprene (10.0 mL) and traces of hydroquinone (two spatula tips), were suspended in 20.0 mL of absolute ethanol. The mixture was placed in a 40.0 mL autoclave and heated at 130 °C for 6 h. Once the autoclave reached room temperature, the mixture was dissolved in a potassium hydroxide solution in ethanol (8.5 g of KOH in 200 mL of EtOH) in a round bottom flask. The solution was stirred and heated for 8 h at 40 °C under air. Stirring was continued for 12 h at room temperature under air. The mixture was heated again at 50 °C for 2h, let to reach room temperature and filtered in vacuum to give a white cream solid. The solid was placed in a vial containing absolute ethanol and left in the fridge overnight. Subsequently, the solid was filtered again, washed with cold ethanol and water, and dried under air. ^{1}HNMR confirmed the identity of the product as 2,6-dimethyl-9,10-anthraquinone.[18] A solution of 2,6-dimethyl-9,10-anthraquinone (1.0 g) in 12.0 mL of 25% nitric acid was placed in a 40.0 mL autoclave and heated at 220 °C for 3 h. After cooling to room temperature, the yellow precipitate was filtered under vacuum and washed with water. The solid was dried overnight,

affording pure **1** with 69% yield.[19] ^{1}H NMR (400 MHz, DMSO): δ 13.77 (s, 2H), 8.69(dd, J= 1.8 Hz, 0.4 Hz, 2H), 8.44(dd, J=8 Hz, 1.8Hz, 2H), 8.36(d,d J= 8 Hz, 0.4 Hz, 2H). HRMS: $(M+H)^+$: 297.0375.

2.3.2 Synthesis of 1,4-dicarboxy-9,10-anthhraquinone (2)

The synthesis of **2** was achieved in two steps by adapting previous procedures described in the literature (Scheme S1).[19, 20] First, a solution of 1,4-naphthoquinone (9.35 g, 0.059 mol) and 2,4-hexadiene (5.0 g, 0.605 mol) in toluene (35 mL) was heated at 65°C for 4 days. Subsequently, the solvent was evaporated and the remaining oily solid was used in the next step without further purification. The oily solid (15.0 g) was disolved in 250 mL absolute ethanol and added to a solution of KOH (30 g) in ethanol (1.25 L), while cooled at 10 °C. Then a current of oxygen was bubbled through the solution for 1 h while the temperature was maintained at 10 °C. After the solvent was evaporated, the semisolid residue was treated with water (600 mL) and extracted with benzene. Removal of the aromatic solvent and afforded 1,4-dimethyl-9,10-anthraquinone with 70% yield.[20] A solution of 1,4-dimethyl-9,10-anthraquinone (1.0 g) in 12.0 mL of 25% nitric acid was placed in a 40.0 mL autoclave and heated at 220 °C for 3 h. After cooling to room temperature, the yellow precipitate was filtered under vacuum and washed with water. The solid was dried overnight, affording pure **2** with 69% yield.[19] ^{1}H NMR (400 MHz, DMSO): δ 13.37 (s, 2H), 8.19 (dd, J=5.6 Hz, 3.2 Hz, 2H), 7.99 (dd, J=5.6 Hz, 3.2 Hz, 2H), 7.89 (s, 2H). HRMS: $(M+H)^+$: 297.0376.

2.3.3 Synthesis of 2,6-Zr-AQ MOF $[Zr_6O_4(OH)_4(C_{16}O_6H_6)_6\,(C_3H_7NO)_{17}(H_2O)_{22}]$

The synthesis was carried out using a similar procedure previously reported in the literature.[21] $ZrCl_4$ (23.0 mg, 0.1 mmol) was disolved in 2.0 mL of DMF and sonicated for 5 minutes. Then, the ligand 2,6-dicarboxy-9,10-anthraquinone **1** (29.6 mg, 0.1 mmol) was added to

the solution, as well as 47 equivalents (0.3 mL) of acetic acid as a modulator. The mixture was sonicated for 15 minutes before being set at 120 °C for 24 h. The 2,6-Zr-AQ-MOF was obtained as a pink powder and isolated by centrifugation. The pink solid was washed and centrifuged three times with fresh DMF and dried under vacuum at room temperature (Yield 31.3 mg, 75 %).

2.3.4 Synthesis of 1,4- Zr-AQ-MOF [$Zr_6O_4(OH)_4(C_{16}O_6H_6)_4(C_2O_2H_3)_{2.76}(CO_2H)_{1.2}(C_3H_7NO)_{11}(H_2O)_{40}$]

A mixture of $ZrCl_4$ (23.0 mg, 0.1 mmol), the ligand 1,4-dicarboxy-9,10-anthraquinone **2** (29.6 mg, 0.1 mmol), acetic acid (1.2 mL, 200 equivalents) and DMF (3.0 mL) was sonicated for 15 minutes. The mixture was heated at 120 °C for 48 h. After cooling at a rate of 1 °C/min, the 1,4-Zr-AQ-MOF was obtained as a pink powder, which was isolated by centrifugation. The pink solid was washed and centrifuged three times with fresh DMF and dried under vacuum at room temperature (Yield 30.0 mg, 72 %).

2.4 RESULTS AND DISCUSSION

The ligands, 2,6-dicarboxy-9,10-anthraquinone (**1**) and 1,4-dicarboxy-9,10-anthraquinone (**2**) were synthesized in two steps by means of a Diels-Alder reaction followed by oxidation, according to Scheme S1.[18-20] The powdered samples of 2,6-Zr-AQ-MOF [$Zr_6O_4(OH)_4(C_{16}O_6H_6)_6(C_3H_7NO)_{17}(H_2O)_{22}$] and 1,4-Zr-AQ-MOF [$Zr_6O_4(OH)_4(C_{16}O_6H_6)_4(C_2O_2H_3)_{2.76}(CO_2H)_{1.24}(C_3H_7NO)_{11}(H_2O)_{40}$] were obtained by the solvothermal synthesis of $ZrCl_4$ and either **1** or **2** in DMF, using acetic acid as a modulator (Figure 2.1). Specifically, the addition of **1** and 47 equivalents of acetic acid to a solution of $ZrCl_4$ in DMF, followed by heating at 120 °C for 1 day afforded 2,6-Zr-AQ-MOF as a pink powder.[21] Similarly, the treatment of **2** and $ZrCl_4$ in a mixture of acetic acid and DMF (1:2.5 by volume) at 120 °C for 2 days gave 1,4-Zr-AQ-MOF as a pink powder.

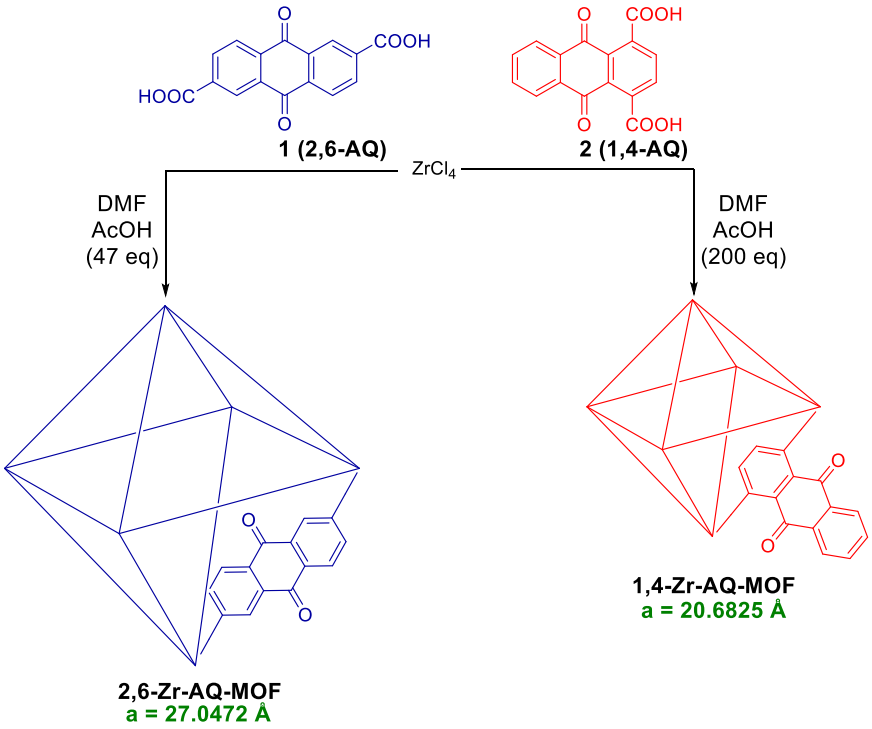

Figure 2.1. Synthesis of 2,6-Zr-AQ-MOF and 1,4-Zr-AQ-MOF.

Powder X-ray diffraction (PXRD) patterns of 2,6-Zr-AQ-MOF and 1,4-Zr-AQ-MOF reveal that both MOFs are isostructural with the UiO series (Figure 2.2). Le Bail refinement of the powder patterns using crystallographic data for UiO-67 and UiO-66 as starting models respectively, revealed a lattice parameter of a=27.0472 Å for 2,6-Zr-AQ-MOF and a=20.6825 Å for 1,4-Zr-AQ-MOF (Figure S2.9-S2.10), which is consistent with the length of each ligand. SEM images of 2,6-Zr-AQ-MOF show that it consists of octahedral-shaped crystallites, characteristic of UiO-type frameworks. The 1,4-Zr-AQ-MOF, on the other hand, exhibited a more inconsistent morphology (Figure S2.11-S2.12), presumably due to incorporated defects (vide infra). The N_2 adsorption isotherms of both MOFs are shown in Figure 2.2. A BET surface area of 175.6 m^2g^{-1} was found for 2,6-Zr-AQ-MOF, while the 1,4-Zr-AQ-MOF exhibited a surface area of 554.16 m^2g^{-1}.

The redox behavior of the ligands in aqueous phosphate buffer was studied by cyclic voltammetry (CV), using a glassy carbon (GC) working electrode. Reduction potentials were recorded at different pH, in order to construct the Pourbaix diagrams. Both ligands show a single-step, reversible CV wave, which shifted to more negative reduction potentials with increasing pH (Figure 2.3 A-B).

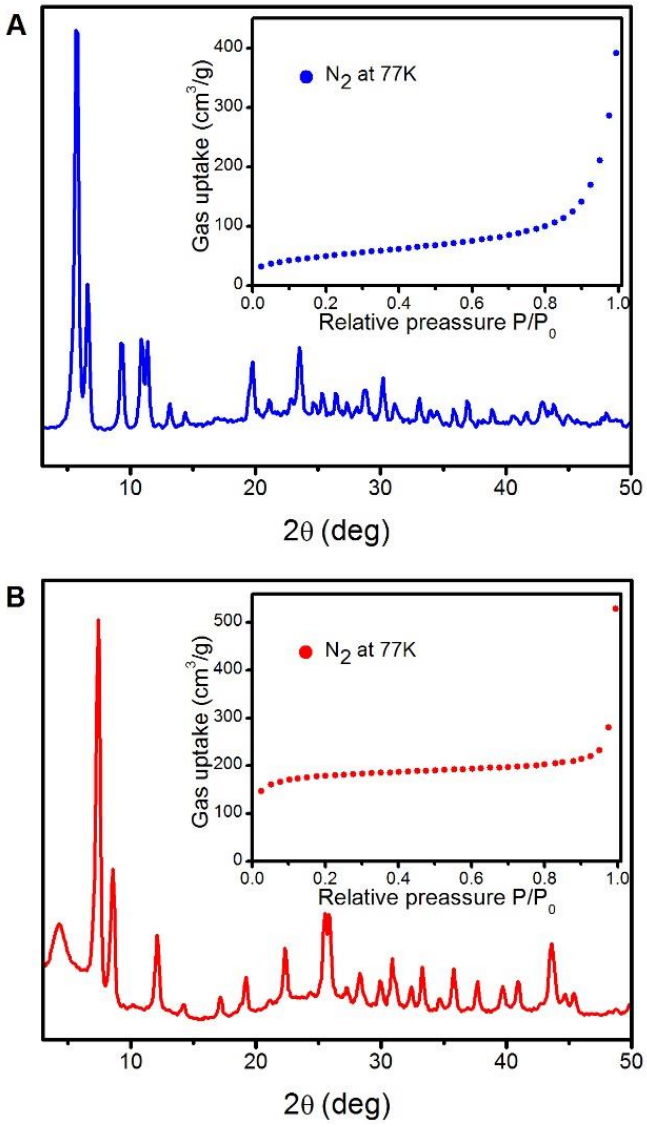

Figure 2.2. PXRD patterns of A) **2,6-Zr-AQ-MOF** and B) **1,4-Zr-AQ-MOF**. The insets show the corresponding N_2 adsorption isotherms.

This linear dependence of the reduction potential with respect to pH is expected to follow the modified Nernst equation:

$$E = E° - \frac{0.05916}{n}\log\frac{1}{[H^+]^m} \qquad (2.1)$$

where m is the number of protons and n is the number of electrons involved in the process. Therefore, the derivative of this relationship can be expressed as:

$$\frac{\partial E}{\partial pH} = -0.05916\frac{m}{n} \qquad (2.2)$$

and represents the slope of the linear regression between E and pH in the different segments of the Pourbaix diagrams (Figure 2.3 C-D). As a result, this expression allows the elucidation of the number of protons and electrons transferred during the reduction. For instance, two different electrochemical processes are apparent in the Pourbaix diagram of ligand **1** (Figure 2.3C). An experimentally determined relationship of dE/dpH of -53 ± 6 between pH 1.33 and 7.35, suggests a two-electron, two-proton transfer to the quinone moiety of the ligand to form the respective hydroquinone. In addition, from pH 7.35 to 11.38, a slope (dE/dpH) of -26 ± 6 evidenced a two-electron, one-proton transfer from the quinone to the correspondent protonated dianion. The appearance of these two processes in ligand **1** is typical of many anthraquinone systems in aqueous buffer and has been extensively discussed in the literature.[8, 9, 22, 23]

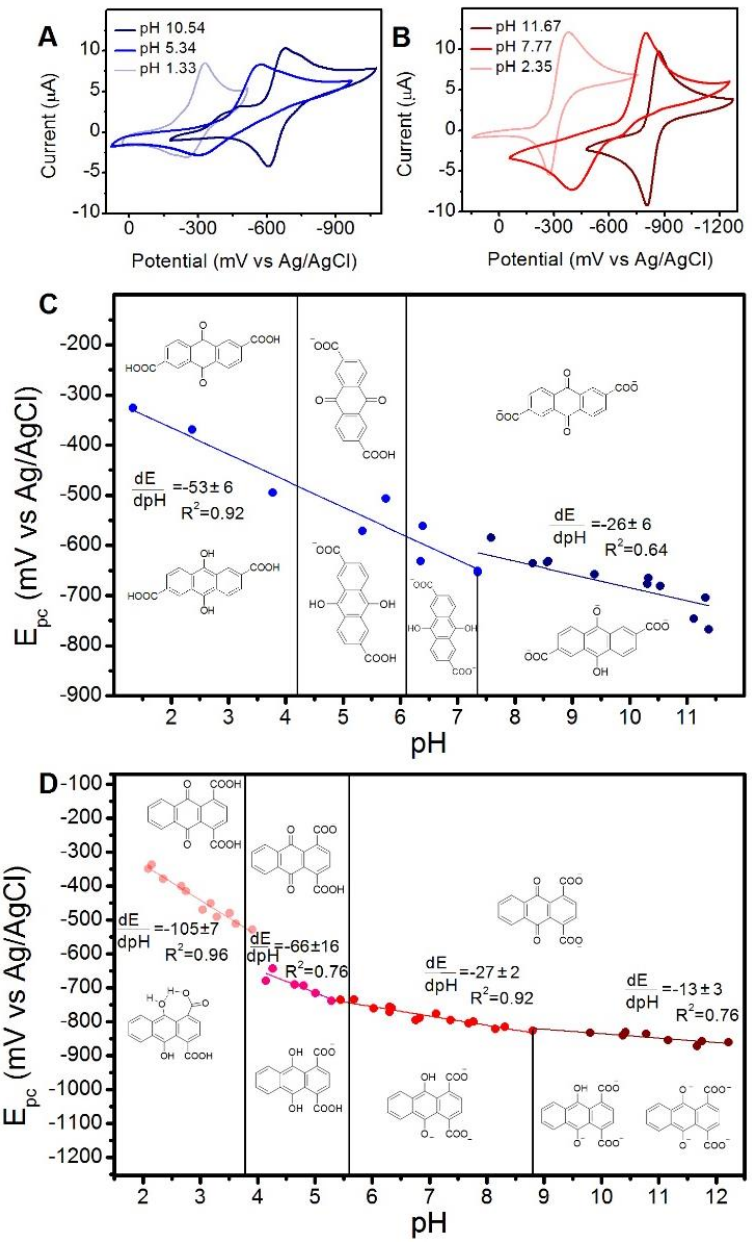

Figure 2.3. Cyclic voltammograms (10 mV s^{-1}) of A) Ligand **1**, 0.1 M phosphate buffer - DMF (9:1 volume) as supporting electrolyte, and B) Ligand **2**, 0.1 M phosphate buffer as supporting electrolyte. Pourbaix diagrams of C) Ligand **1**, and D) Ligand **2**.

The boundary between the two types of electrochemical processes defines the electrochemical pKa of **1** (7.35). In addition, the two chemical pKa values for the carboxylic acids of **1** were determined via the titration with NaOH (Figure S2.7). These pKa values (pKa_1 = 4.2 and pKa_2 = 6.1) are also represented in the Pourbaix Diagram of **1** as vertical lines (Figure 2.3C).

Similarly, the titration of **2** (Figure S2.8) allowed the determination of $pKa_1 = 3.7$ and $pKa_2 = 5.6$ for the two carboxylic acid in **2** (Figure 2.3D).

Interestingly, ligand **2** was found to undergo four different PCET processes (Figure 2.3D). Similar to ligand **1**, a two-electron, one-proton transfer from the quinone to the correspondent protonated dianion was observed from pH 5.46 to 8.80, as evidenced by a slope of -27 ± 2. In addition, for pH between 3.91 and 5.46, the slope was found to be -66 ± 16, suggesting a two-electron, and two-proton transfer process of the quinone moiety of **2** to form the hydroquinone.

However, two other processes were evidenced at the highest and lowest pH ranges tested in this study: At high pH (from pH 8.80 to 12.22) a four-electron one-proton transfer represented by a slope of -13 ± 3, involved the reaction of two ligand molecules to produce both the dianion and protonated dianion.[24-26] The formation of equal amounts of these species of **2** at alkaline pH, which was not observed in **1**, may be a result of the difficulty to protonate this moiety due to the proximity of the carboxylic acid.

Moreover, at pH below 3.91, a slope of -105±7 involving a transfer of either two electrons and three protons, or two electrons and four protons characterized the last process. Since the carboxylic acid groups of **2** are fully protonated at pH <3.7 a maximum of two protons can be transferred to the quinone to form the hydroquinone. The apparition of a third or fourth proton during the reduction can be explained based on the proximity of the carboxylic acids to the quinone moiety in **2**. First, it is expected that the pKa of the carboxylic acids of **2** in the hydroquinone state is much lower (≈2) compared to the quinone state.[27, 28] As a result, the observed transfer of two electrons and three/four protons could be attributed to a simultaneous protonation of the carboxylic acid of the reduced hydroquinone moiety that is stabilized through hydrogen bonding. Figure 2.3D shows the proposed seven-membered ring structure formed during the two-electron, three-proton

transfer. Predominantly, hydroquinones have been found to form both intermolecular[29, 30] and intramolecular hydrogen bonding with other –OH functionalities.[31] In fact, the existence of hydrogen bonding between hydroquinone moieties and carboxylic acids is well documented.[31, 32] Consequently, the proximity of the carboxylic acids to the hydroxyl group in the hydroquinone species could also lead to intramolecular stabilization due to hydrogen bonding. In order to test this claim, the Pourbaix diagram of a similar derivative, 1,4-dimethyl-9,10-anthraquinone, was obtained under identical conditions (Figure S2.18). In this analogue, the carboxylic acid groups are replaced with methyl groups. A slope of -52 ± 2 was determined for pH between 1.69 and 6.15 indicating that this analogue undergoes a two-electron, two-proton transfer. This finding supports the earlier explanation for the transfer of additional protons during the reduction of **2** at pH <3.91 with the third/fourth proton originating from the protonation of the carboxylate in the hydroquinone form of **2**, and stabilized through intramolecular hydrogen bonding. This stabilization is less likely in **1** since carboxylic acid and hydroxyl functionalities are further apart.

Cyclic voltammetry of the anthraquinone frameworks were performed on the dried slurry of the MOF powder (10 mg), graphite (10 mg), poly-methyl methacrylate (3.34 mg), and THF (1 mL), deposited on a GC electrode. Subsequently, this working electrode was used in a three-electrode assembly, with a HEPES-buffered aqueous solution as supporting electrolyte (see SI for detailed procedure). UV-Vis spectroscopy was used to monitor the stability of the frameworks, evidenced as the absence of ligand absorption in solution before and after the CV measurements over the range of pH (Figure S2.20-S2.22). The 2,6-Zr-AQ-MOF showed stability from pH 1.74 to 9.67, while the 1,4-Zr-AQ-MOF was stable from pH 1.66 to 6.75. Both MOFs showed a reversible redox process which shifted to more negative potential with increasing pH (Figure 2.4 A-B).

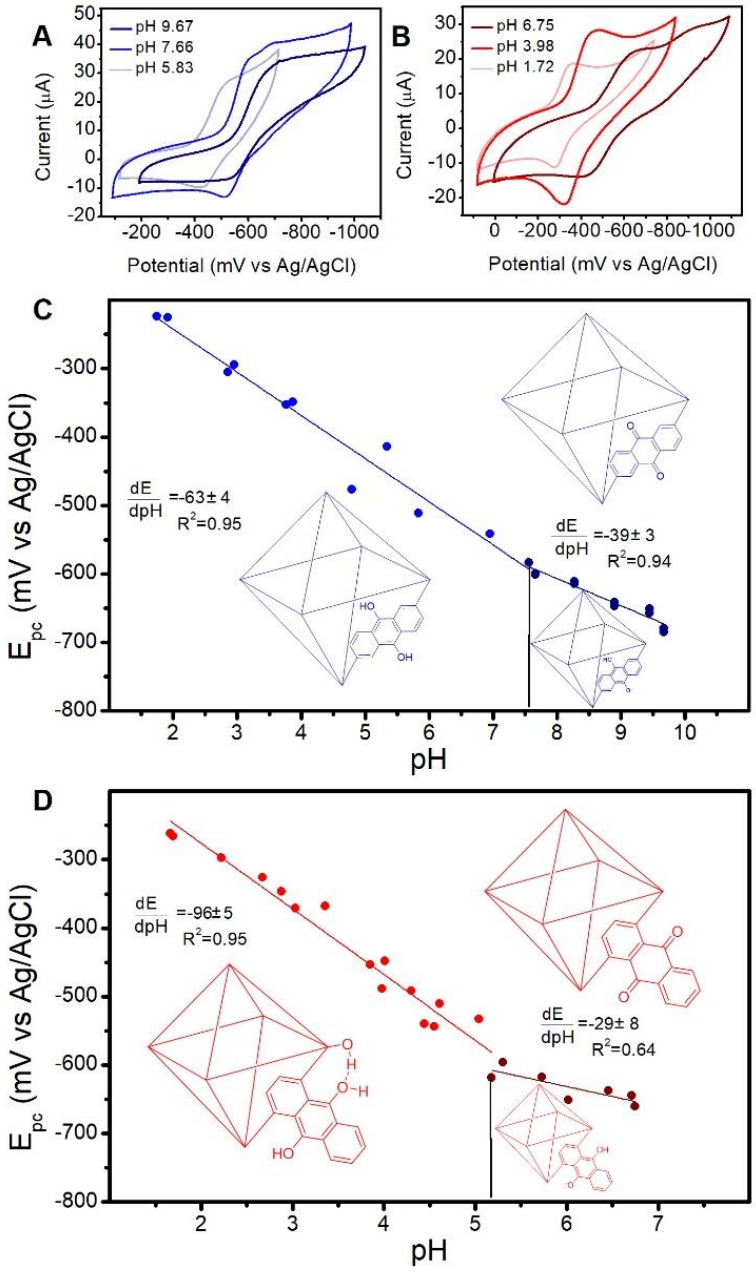

Figure 2.4. Cyclic voltammograms (100 mV s^{-1}, 0.1 M HEPES buffer as supporting electrolyte) of A) **2,6-Zr-AQ-MOF**, and B) **1,4-Zr-AQ-MOF**. Pourbaix diagrams of C) **2,6-Zr-AQ-MOF**, and D) **1,4-Zr-AQ-MOF**

The behavior of 2,6-Zr-AQ-MOF was very similar to that observed for its free ligand in solution. The Pourbaix diagram of this MOF showed two electrochemical processes, defined by an electrochemical pKa of 7.56 (Figure 2.4C). For pH <7.56, a slope of -63 ± 4 was observed

indicating the two-electron, two-proton transfer to the quinone resulting in the hydroquinone state of the ligand inside 2,6-Zr-AQ-MOF. Furthermore, for pH >7.56 either a two-electron, one-proton transfer or a two-electron, two-proton transfer took place, as evidenced by a slope of -39 ± 3. For clarity, only the two-electron, one-proton transfer is shown in the correspondent segment of the Pourbaix Diagram in Figure 2.4C. The similarity in the electrochemical pKa of 2,6-Zr-AQ-MOF (7.56) and its ligand in solution (7.35) reveals that the pore dimensions of this framework allow a sufficient transport of protons inside the MOF pores. Consequently, the pH in the pores is the same as in the bulk solution, and only the pH tailors the number of protons transferred to the quinone moiety during the reduction. This fact corroborates the benefits of introducing anthraquinone moieties as ligands instead of encapsulating them in the MOF pores as nanoconfined molecules.[15, 16]

Unlike its ligand, 1,4-Zr-AQ-MOF revealed only two electrochemical processes (Figure 2.4D). For pH > 5.18, the formation of the protonated dianion through a two-electron, one-proton transfer was characterized by a slope of -29 ± 8. This behavior is comparable to the one of its ligand in solution at pH between 5.46 and 8.80 (Figure 2.3D), and to the 2,6-Zr-AQ-MOF (Figure 2.4C). This observation suggests that 1,4-Zr-AQ-MOF also allows the efficient penetration of protons into the MOF structure, and demonstrates the consistency between the pore environment with respect to the bulk.

The Pourbaix diagram of 1,4-Zr-AQ-MOF also showed a slope of -96 ± 5 for pH < 5.18, representing a two-electron, three-proton transfer, similar to the one observed for **2** at pH < 3.91 (Figure 2.3D). Since the ligand of 1,4-Zr-AQ-MOF can only accept maximum of two protons without breaking the metal-carboxylate bonds, this behavior could be explained based on the level of defects in the MOF. Particularly, the UiO frameworks exhibit two different types of defects. On

one hand, “missing linker defects” refer to the absence of ligands coordinated to the Zr-oxide cluster, that is commonly compensated by modulator molecules connected to the node.[33] On the other hand, the recently discovered “missing cluster defects”, correspond to the absence of $Zr_6(\mu_3\text{-}O)_4(\mu_3\text{-}OH)_4$ node, as well as the 12 ligands connected to it, in correlated nanoregions of the **reo** topology.[34, 35] We sought to calculate the defects in 1,4-Zr-AQ-MOF using quantitative NMR analysis (Figure S2.23), finding a total modulator to linker molar ratio of 0.96, suggesting an equivalent amount of linker and modulator in the framework, presumably due to the high concentration of acetic acid utilized during the synthesis (Figure 2.1). Elemental analysis on the framework (Table S2.1) also supported these findings. This framework is an analogue of the UiO-66 MOF, which has been typically recognized to have a high amount of defects,[33, 35, 36] and the shape of the anthraquinone ligand suggests steric hindrance during its formation (Figure 2.1). More importantly, the PXRD pattern of 1,4-Zr-AQ-MOF (Figure 2.2B) displays a broad peak at 2θ range of *ca.* 3-6°, which has been recently assigned as a fingerprint of missing node defects in UiO frameworks, where one quarter of the MOF clusters are missing.[34] The high defectivity of 1,4-Zr-AQ-MOF, can subsequently explicate the observed two-electron, three-proton transfer shown in Figure 2.4D, when considering two different possibilities:

The existence of ligands connected only to one node could lead to intramolecular hydrogen bonding between the free carboxylic acid and the reduced hydroquinone moiety, in a similar fashion than its ligand in solution (Figure 2.3D). Alternatively, the proximity of the quinone moiety to the zirconium node (2.6-2.8 Å) inside the framework could also lead to hydrogen bonding between the hydroquinone and the protons present on the inorganic cluster, as represented in Figure 2.4D for pH < 5.18. Two of the three types of protons present in the zirconium node are recognized as -OH and $-OH_2$ groups that occupy the place of missing linkers.[17] The acidity of these

protons in UiO-66 has been recently studied, finding pKa values of 8.30 and 6.79, respectively.[17] This fact suggests that at pH < 5.18 the highly defected node of 1,4-Zr-AQ-MOF is most likely protonated, facilitating hydrogen bonding between the hydroquinone and the protons in the node (Figure 2.4D). A related cooperative behavior between linker and node was postulated for the electrocatalytic water oxidation in PCN-224, where the node acts as a proton acceptor.[37] These processes are not observed in the Pourbaix diagram of 2,6-Zr-AQ-MOF because the quinone moiety is relatively distant (5.0-5.2 Å) from the zirconium node (Figure 2.1).

2.5 CONCLUSION

In summary, we have shown that PCET can be modulated in anthraquinone-based Zr MOFs as a function of the pH. The positioning of the quinone moiety with respect to the zirconium node, the amount of defects, and the pore size of these materials are directly influencing the amount of protons transported to the frameworks. These results demonstrate that MOFs have potential as proton-electron carriers for electronic applications and encourage further research in this area.

2.6 SUPPORTING INFORMATION

2.6.1 Materials and Instrumentation

2.6.1.1 Materials

All reagents and solvents were purchased from commercial sources and used without further purification.

2.6.1.2 Nuclear Magnetic Resonance (NMR)

^{1}H NMR spectra were acquired on a Agilent U4-DD2 spectrometer operating at 400 MHz. Samples were analyzed as solutions in DMSO-d_6 (ca. 10 mg mL^{-1}) at 25 °C in standard 5 mm o.d. tubes.

2.6.1.3 High Resolution Mass Spectrometry (HR-MS)

High-resolution mass spectra were taken on an Agilent Technologies 6220 TOF LC/MS mass spectrometer.

2.6.1.4 Attenuated Total Reflectance Fourier-Transform Infrared Spectroscopy (ATR-FTIR)

ATR-FTIR spectra were collected on a Varian 670 FT-IR Spectrometer with a diamond Specac Golden Gate attachment. All spectra were recorded from 4000 to 400 cm^{-1} with 4 cm^{-1} resolution. The spectra of the powder samples consists of the average of 24 scans. A background spectrum collected on air was subtracted from sample spectra.

2.6.1.5 Titrations with base

Titrations were performed manually with a Venier LabQuest pH meter. The 0.01M NaOH titrant was standardized before measurements using KHP, and was delivered from a 50.0-ml graduated buret. For the titration of the ligand 2,6-dicarboxy-9,10-anthhraquinone **1**, the titrand consisted of a solution of 24.3 mg of the ligand in 100.0 mL of water. For the titration of the ligand

1,4-dicarboxy-9,10-anthhraquinone **2**, the titrand consisted of a solution of 27.5 mg of the ligand in 65.0 mL of water.

2.6.1.6 Powder X-Ray Diffraction (PXRD)

PXRD measurements were carried out on a Rigaku Miniflex equipped with a Cu(Kα) radiation source (λ=1.5418 Å). The scanning rate was 1°/min using a 2θ range of 3- 50° on continuous mode. The samples were mounted onto reflective disks with a Si (510) surface.

2.6.1.7 Scanning Electron Microscopy (SEM)

A LEO (Zeiss) 1550 high-performance Schottky field-emission scanning electron microscope equipped with an in-lens detector was used at 5.0 kV to obtain high-resolution images of the MOFs.

2.6.1.8 Thermogravimetric Analysis (TGA)

A Q-series TGA from TA Instruments was used to analyze the thermal stability of the MOFs. Samples (∼16 mg) were placed on an aluminum pan and heated under nitrogen at a rate of 10 °C/min over the temperature range of 25−700 °C (for **2,6-Zr-AQ-MOF**) and 25−1000 °C (for **1,4-Zr-AQ-MOF**).

2.6.1.9 Gas Sorption Isotherms

The sorption isotherm measurements were collected on a Quantachrome Autosorb-1. The samples were placed in a 6 mm large bulb sample cell, which was degassed under vacuum at a temperature of 100 °C for 8 h and at room temperature for 16 h. The surface area of the MOFs was determined from the N_2 adsorption isotherms at 77 K by fitting the adsorption data within the 0.05−0.3 P/P0 pressure range to the BET equation.[38]

2.6.1.10 Electrochemistry

All electrochemical experiments were performed in a BASi EC Epsilon potentiostat using a standard three-electrode configuration: a glassy carbon (GC) electrode as a working electrode, a high surface area Pt mesh as the counter electrode, and an aqueous Ag/AgCl reference electrode (saturated aqueous KCl). Potassium Ferricyanide was used to calibrate the reference electrode with all the potentials reported vs Ag/AgCl. For the 0.1 M phosphate buffer and 0.1 M HEPES buffer electrochemistry, phosphoric acid, potassium phosphate monobasic, sodium phosphate dibasic, sodium phosphate, and HEPES were used as purchased from Sigma Aldrich.

2.6.1.11 UV-Visible Absorption Spectroscopy

Steady-state UV-vis absorption spectroscopy was performed in a Cary 5000 UV-vis-NIR spectrophotometer at a scan rate of 600 nm/min over the wavelength range of 200-500 nm.

2.6.2 Synthetic Procedures

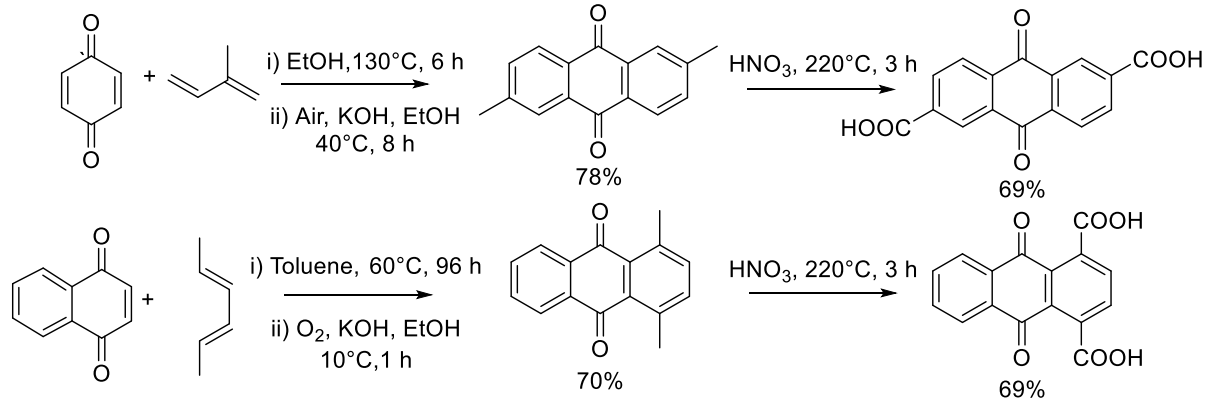

Scheme S2.1: Synthesis of 2,6-dicarboxy-9,10-anthhraquinone (**1**) and 1,4-dicarboxy-9,10-anthhraquinone (**2**)

2.6.3 Physical Characterization of the ligands: NMR, MS, FT-IR and Titrations

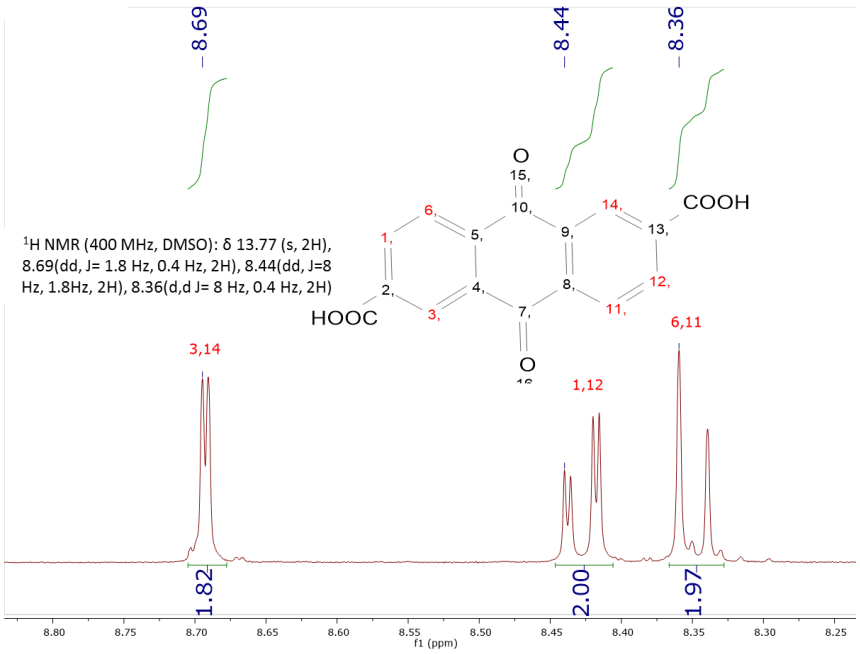

Figure S2.1: ^{1}H NMR of 2,6-dicarboxy-9,10-anthhraquinone

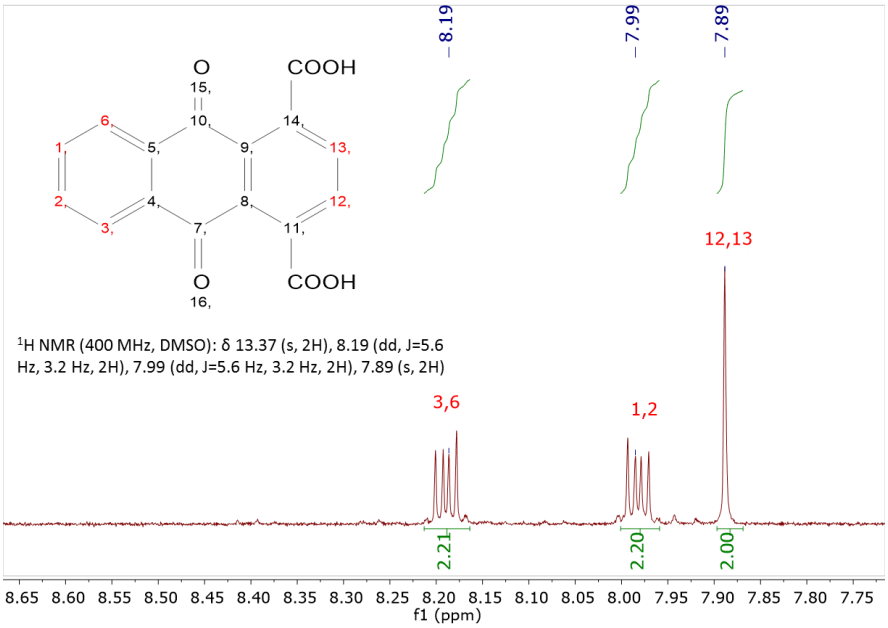

Figure S2.2: ^{1}H NMR of 1,4-dicarboxy-9,10-anthhraquinone

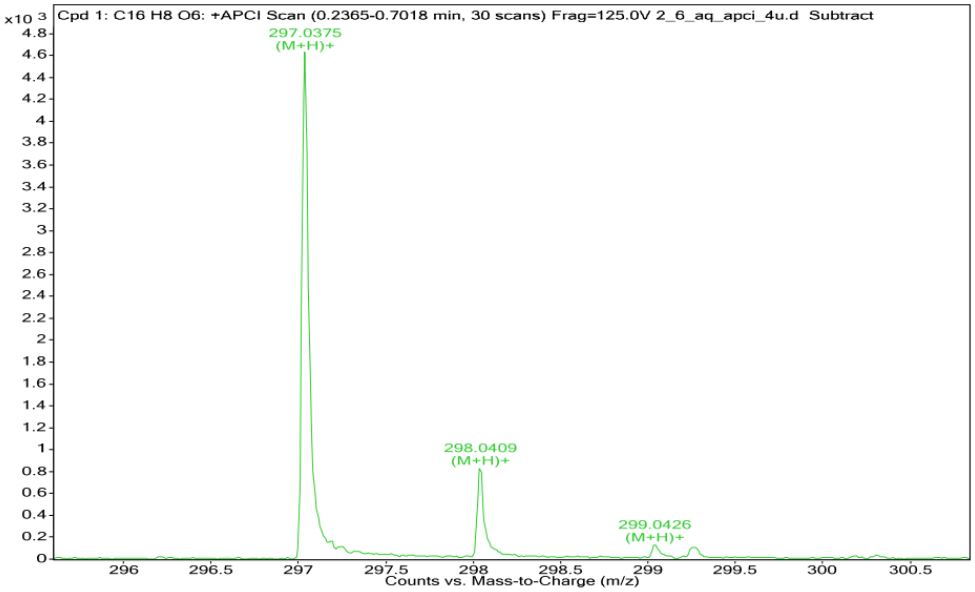

Figure S2.3: HRMS of 2,6-dicarboxy-9,10-anthhraquinone

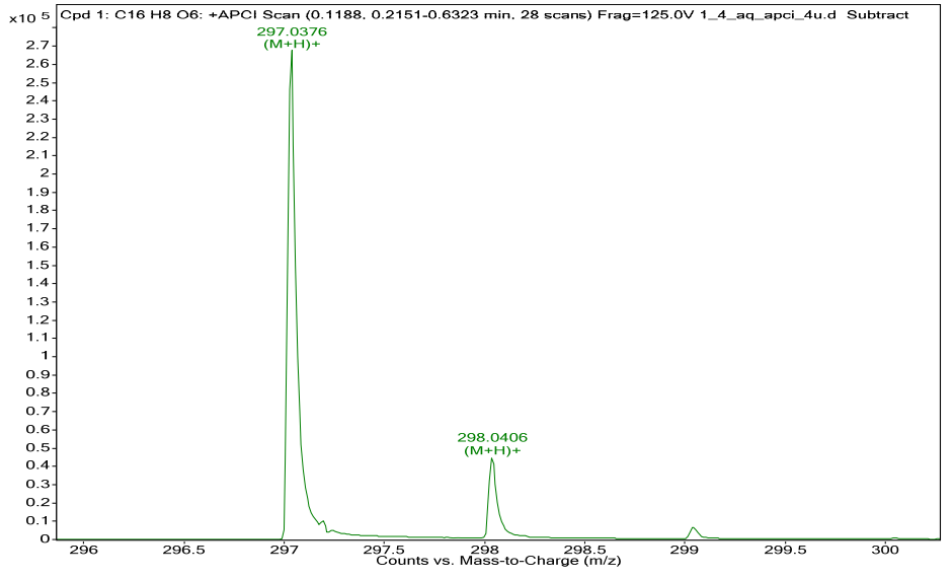

Figure S2.4: HRMS of 1,4-dicarboxy-9,10-anthhraquinone

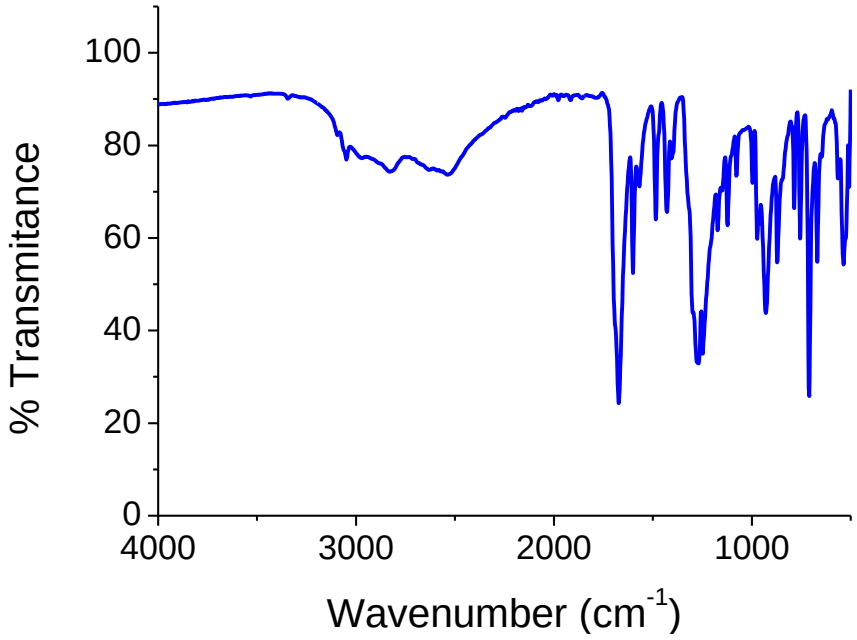

Figure S2.5: FT-IR spectra of 2,6-dicarboxy-9,10-anthhraquinone

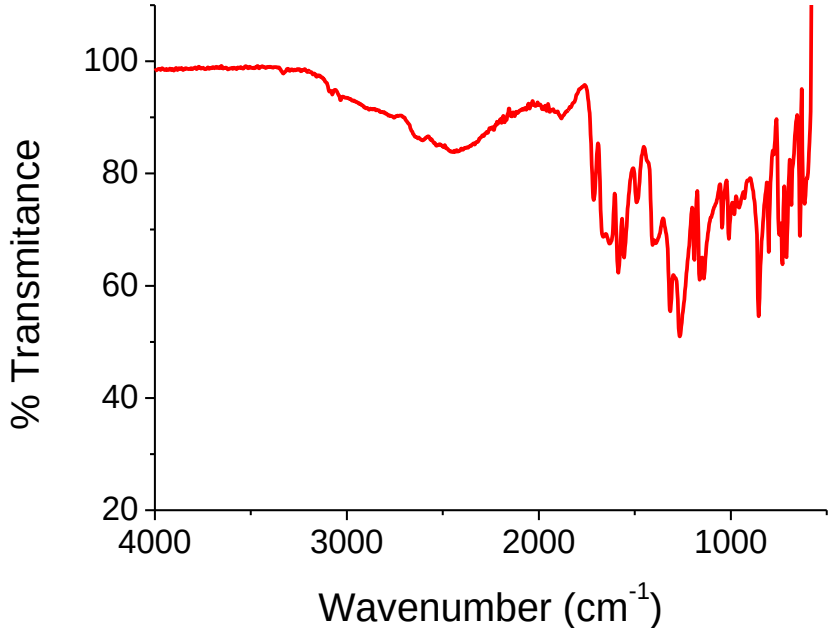

Figure S2.6: FT-IR spectra of 1,4-dicarboxy-9,10-anthhraquinone

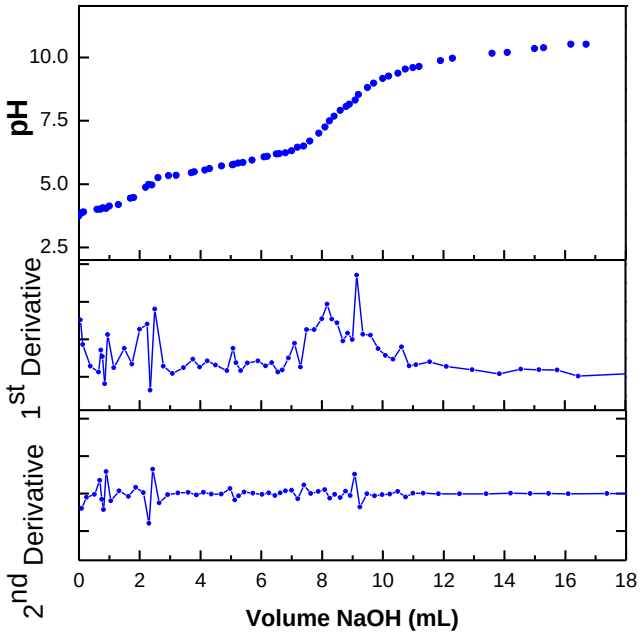

Figure S2.7: Titration curve of 2,6-dicarboxy-9,10-anthhraquinone

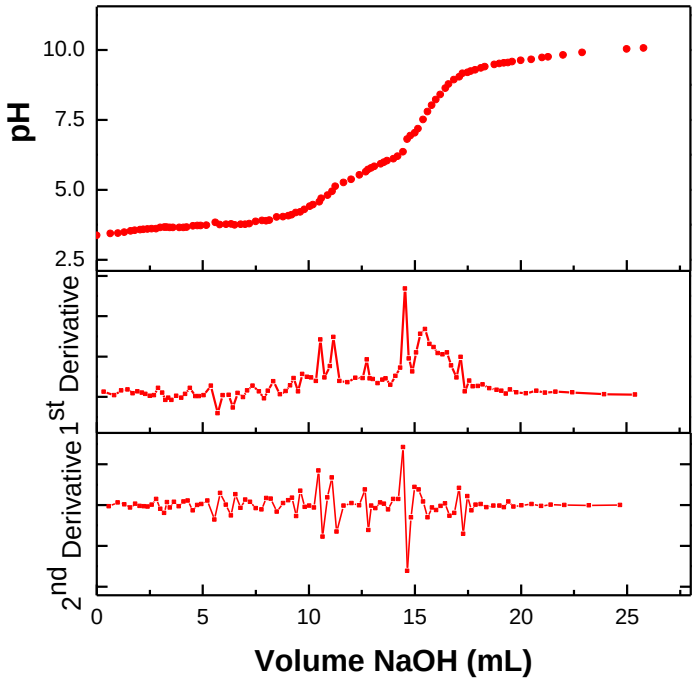

Figure S2.8: Titration curve of 1,4-dicarboxy-9,10-anthhraquinone

2.6.4 Physical Characterization of the MOFs: PXRD Le Bail refinement, SEM, and TGA

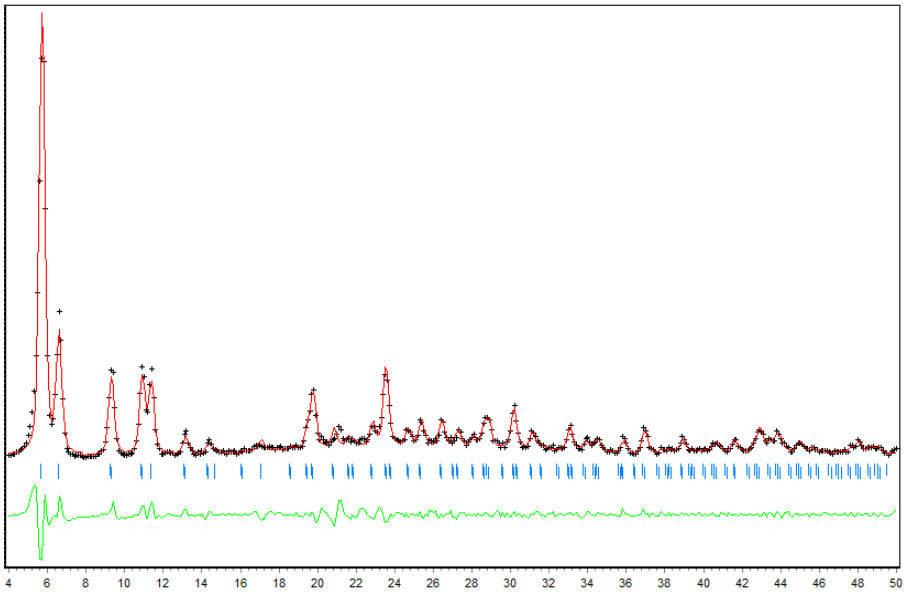

Figure S2.9: Le Bail refinement of 2,6-Zr-AQ-MOF PXRD pattern. Black cross – experimental pattern, Red – Model pattern, Blue – Positions of the allowed reflections, Green – Difference between model and experimental patterns.

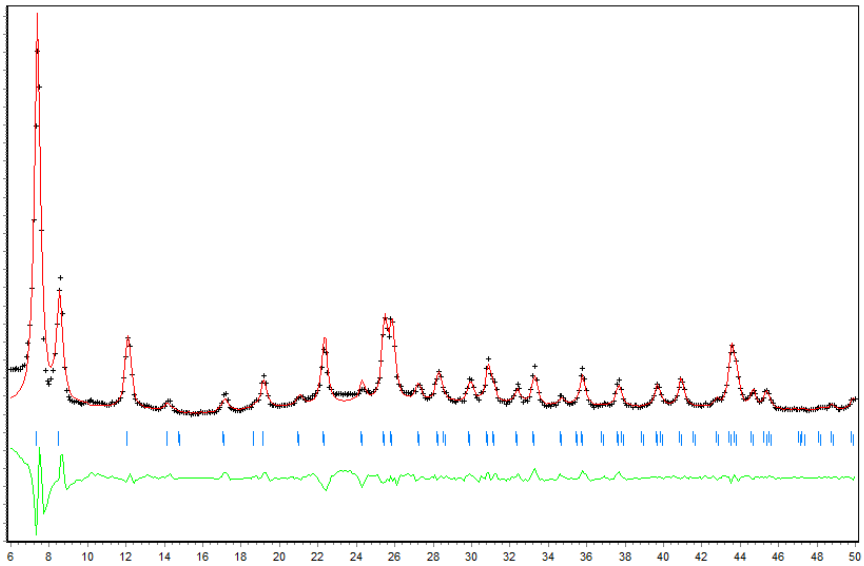

Figure S2.10: Le Bail refinement of 1,4-Zr-AQ-MOF PXRD pattern. Black cross – experimental pattern, Red – Model pattern, Blue – Positions of the allowed reflections, Green – Difference between model and experimental patterns.

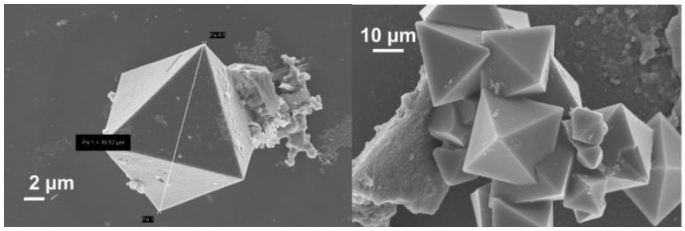

Figure S2.11: SEM images of 2,6-Zr-AQ-MOF

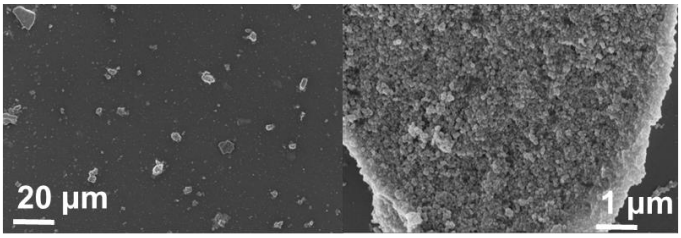

Figure S2.12: SEM images of 1,4-Zr-AQ-MOF

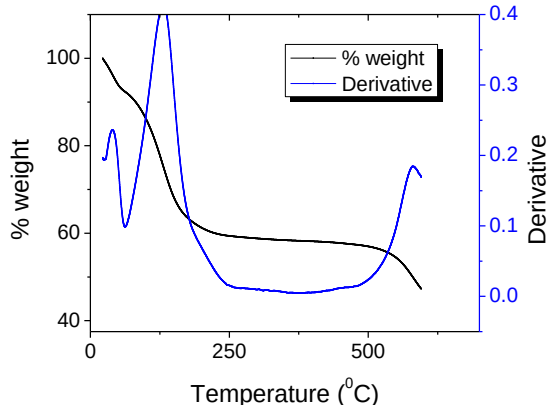

Figure S2.13: TGA of 2,6-Zr-AQ-MOF

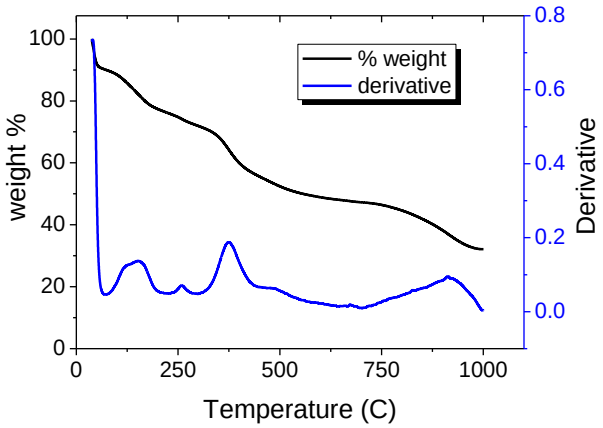

Figure S2.14: TGA of 1,4-Zr-AQ-MOF

2.6.5 Electrochemical Methods and Characterization of the ligands Cyclic voltammetry analysis

Analyses were performed in a standard three-electrode array: a glassy carbon (GC) electrode, a Ag/AgCl reference, and a Pt mesh. Phosphate buffer solutions 0.1 M (10.0 mL) at different pH were used as the supporting electrolyte. The buffers used were: H_3PO_4 + KH_2PO_4 (for pH 1-4), KH_2PO_4 + Na_2HPO_4 (for pH 5-9), and Na_2HPO_4 + Na_3PO_4 (for pH 10-14). Before the experiment was carried out, nitrogen was bubbled for 20 minutes to the solution. A background scan was taken before the addition of the analyte. The concentration of the ligand in solution was 1 mM. Cyclic voltammograms were collected at a scan rate of 10 mV s^{-1} (12 cycles). The GC electrode was polished between scans.

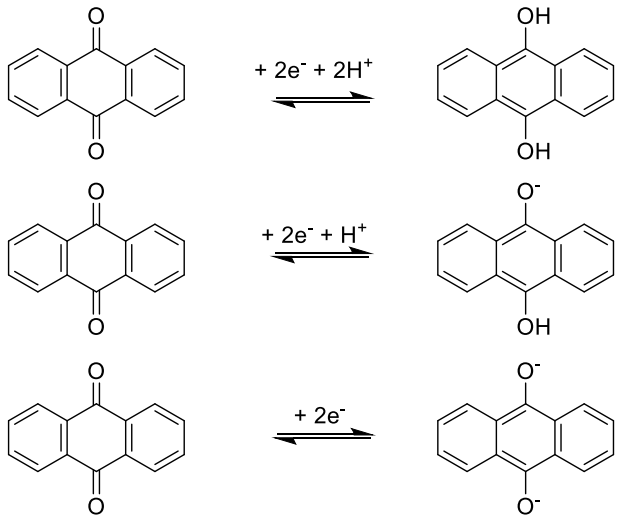

Scheme S2.2: Reduction of anthraquinone in aqueous buffer. Top – Two-electron, two-proton reduction of quinone (Q) to hydroquinone (QH_2), Middle – Two-electron, one-proton reduction of quinone (Q) to protonated dianion (QH^-), Bottom –Two-electron reduction of quinone (Q) to dianion (Q^{2-}).

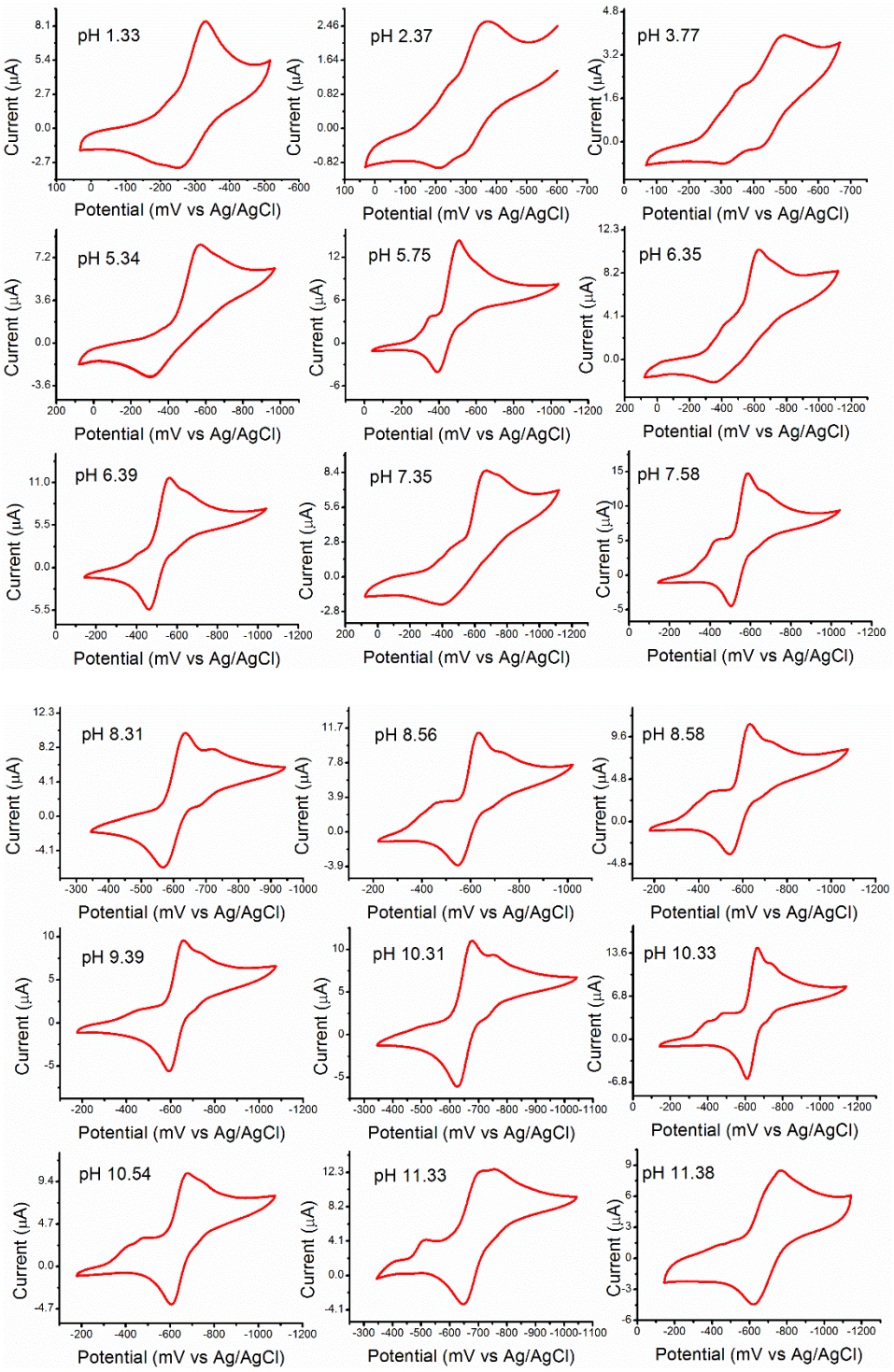

Figure S2.15: Cyclic voltammograms (GC electrode, 10 mV s^{-1}, 0.1 M phosphate buffer-DMF (9:1 volume) as supporting electrolyte) of ligand **1** at different pH

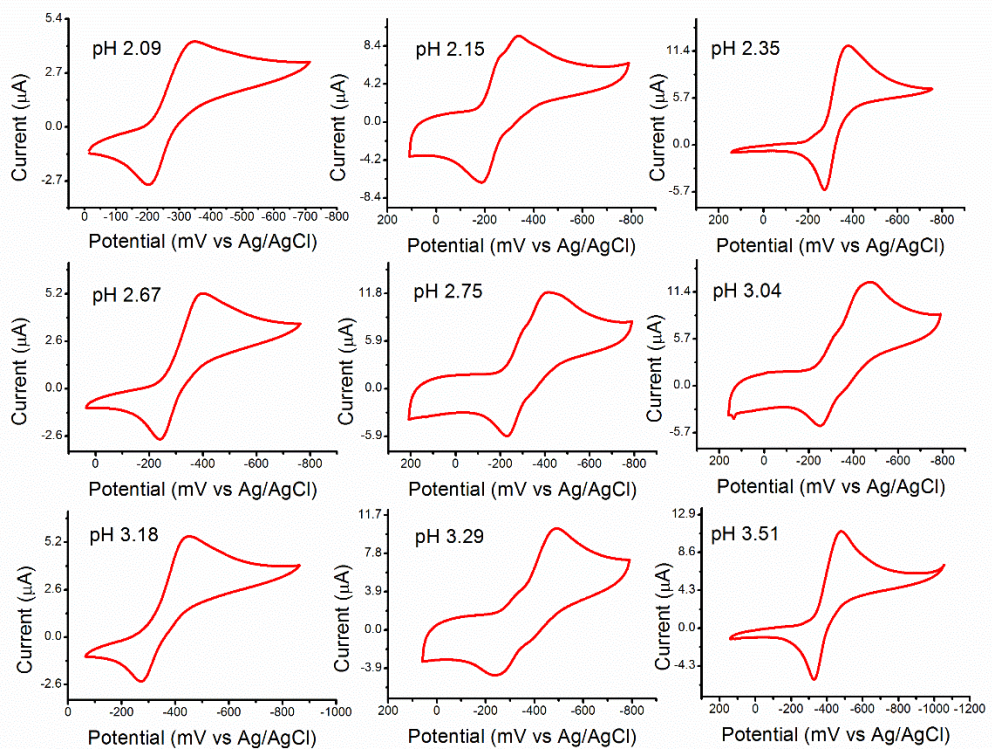
pH 2.09
pH 2.15
pH 2.35
pH 2.67
pH 2.75
pH 3.04
pH 3.18
pH 3.29
pH 3.51
Current (μA)
Potential (mV vs Ag/AgCl)

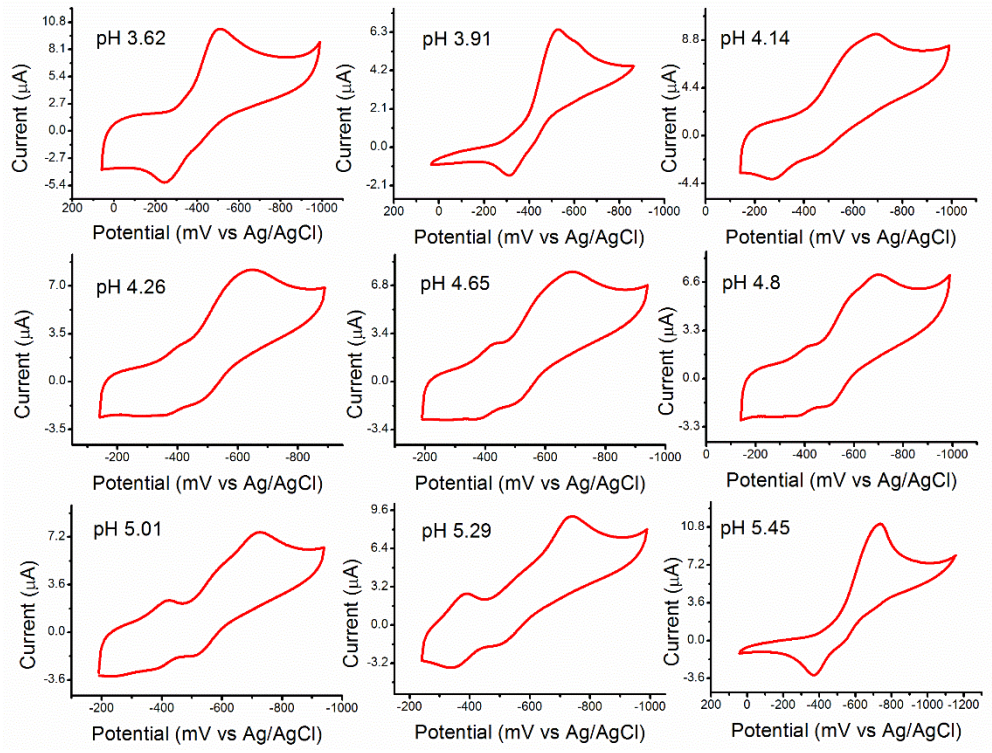
pH 3.62
pH 3.91
pH 4.14
pH 4.26
pH 4.65
pH 4.8
pH 5.01
pH 5.29
pH 5.45
Current (μA)
Potential (mV vs Ag/AgCl)

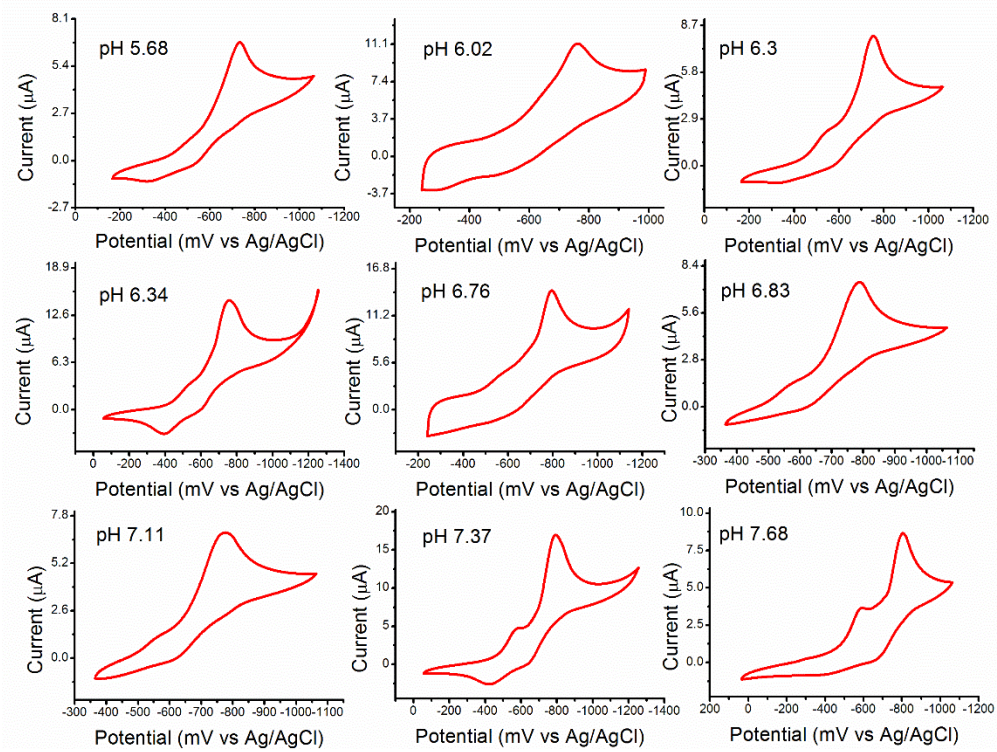
pH 5.68
pH 6.02
pH 6.3
pH 6.34
pH 6.76
pH 6.83
pH 7.11
pH 7.37
pH 7.68
Current (μA)
Potential (mV vs Ag/AgCl)

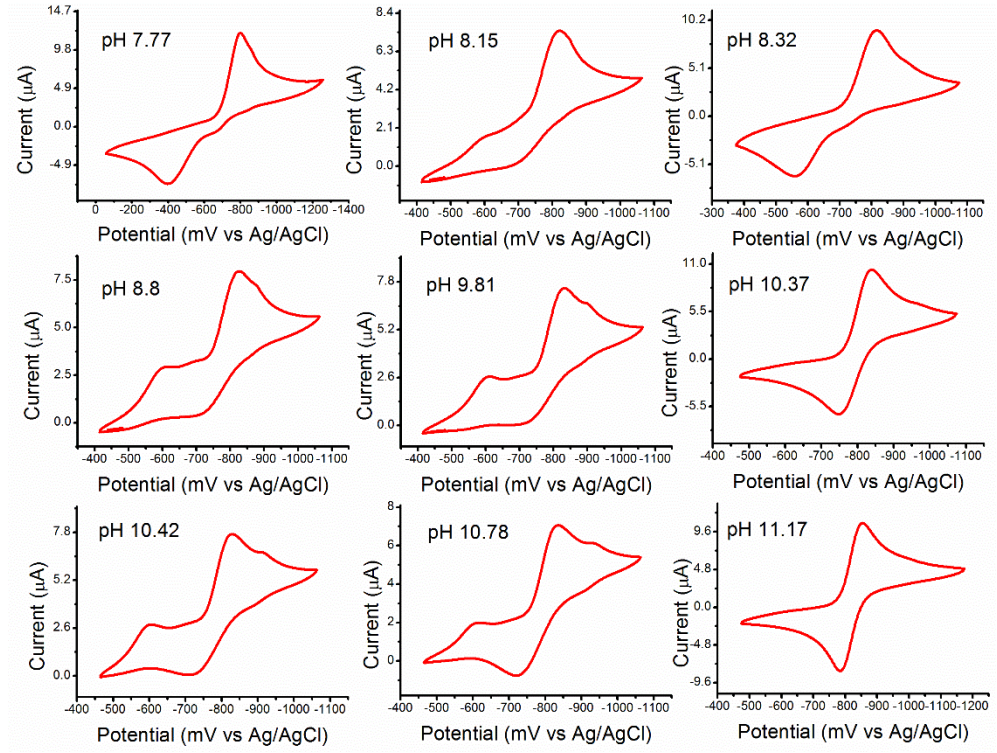
pH 7.77
pH 8.15
pH 8.32
pH 8.8
pH 9.81
pH 10.37
pH 10.42
pH 10.78
pH 11.17
Current (μA)
Potential (mV vs Ag/AgCl)

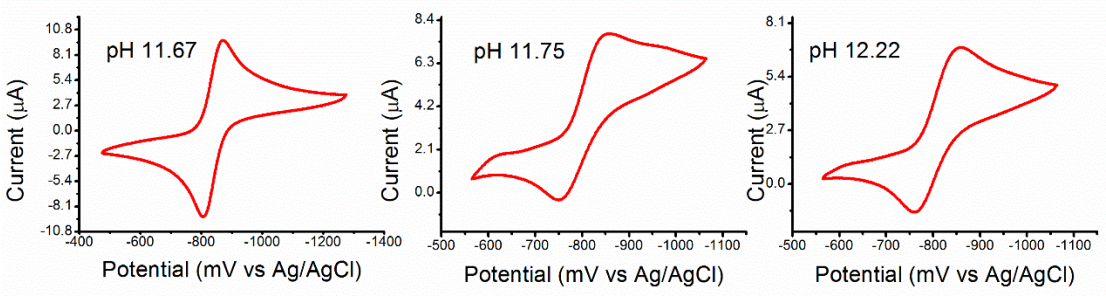

Figure S2.16: Cyclic voltammograms (GC electrode, 10 mV s^{-1}, 0.1 M phosphate buffer as supporting electrolyte) of ligand **2** at different pH

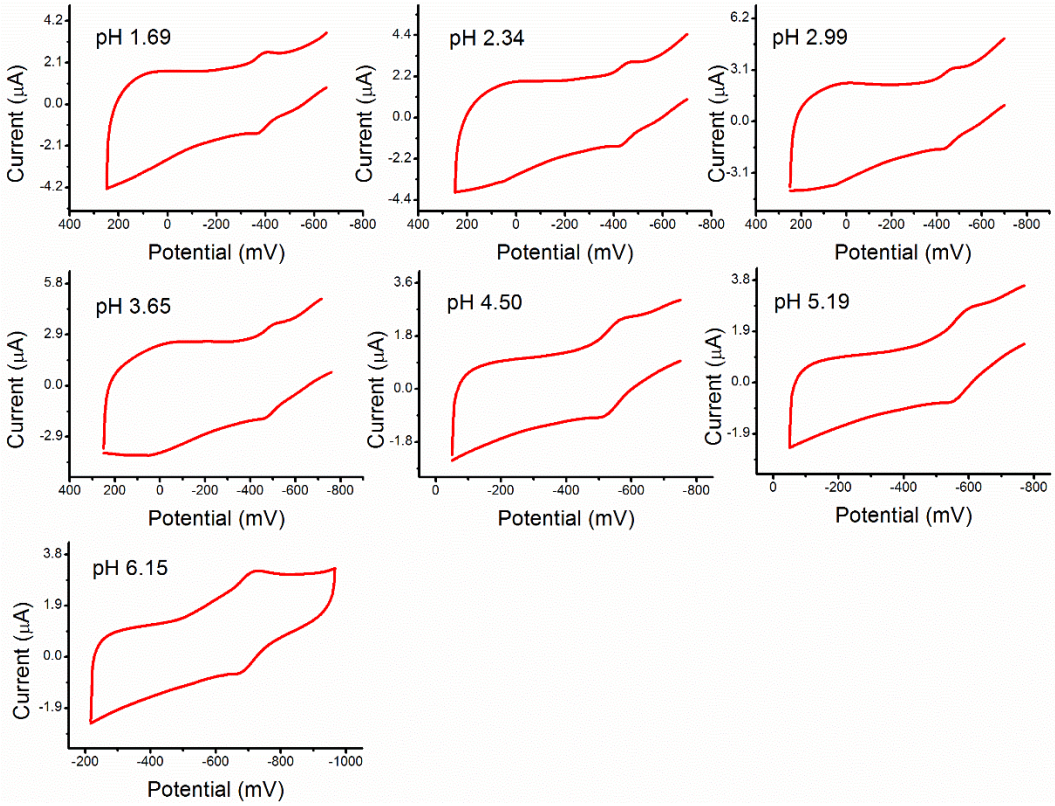

Figure S2.17: Cyclic voltammograms (GC electrode, 10 mV s^{-1}, 0.1 M phosphate buffer as supporting electrolyte) of 1,4-dimethyl-9,10-anthraquinone at different pH

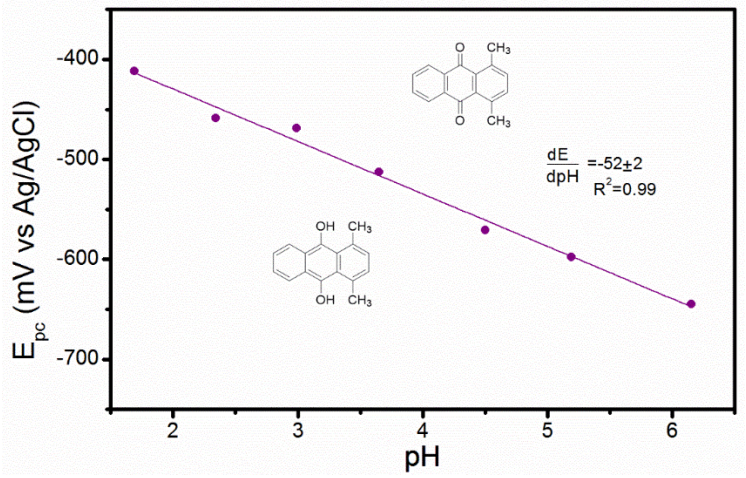

Figure S2.18: Pourbaix diagram (GC electrode, 10 mV s^{-1}, 0.1 M phosphate buffer as supporting electrolyte) of 1,4-dimethyl-9,10-anthraquinone

2.6.6 Electrochemical Methods and Characterization of the MOFs

2.6.6.1 Preparation and dropcasting of the slurry modified electrode

A solution of Poly-methyl methacrylate (3.34 mg) in 1.0 mL of THF was sonicated for 10 min. Subsequently, 10.0 mg of MOF and 10.0 mg of graphite were added to the solution in order to create a suspension that was stirred for 1 h. The dropcasting was performed by adding 40.0 µL of the slurry in the surface of the glassy carbon electrode, and letting it dry for 20 min. The electrode was polished and re-coated again after every measurement.

2.6.6.2 Cyclic voltammetry analysis

Analyses were performed in a standard three-electrode array: a slurry modified GC electrode, a Ag/AgCl reference, and a Pt mesh. Solutions of 0.1 M HEPES (10.0 mL) buffer at different pH were used as the supporting electrolyte. The pH was adjusted using either HCl or NaOH. Before the experiment was carried out, nitrogen was bubbled for 20 minutes to the solution. Cyclic voltammograms were collected at a scan rate of 100 mV s^{-1} (12 cycles). UV-vis spectroscopy was used to monitor the stability of the MOFs, evidenced by the absence of ligand absorption before and after the CV measurements over the range of pH.

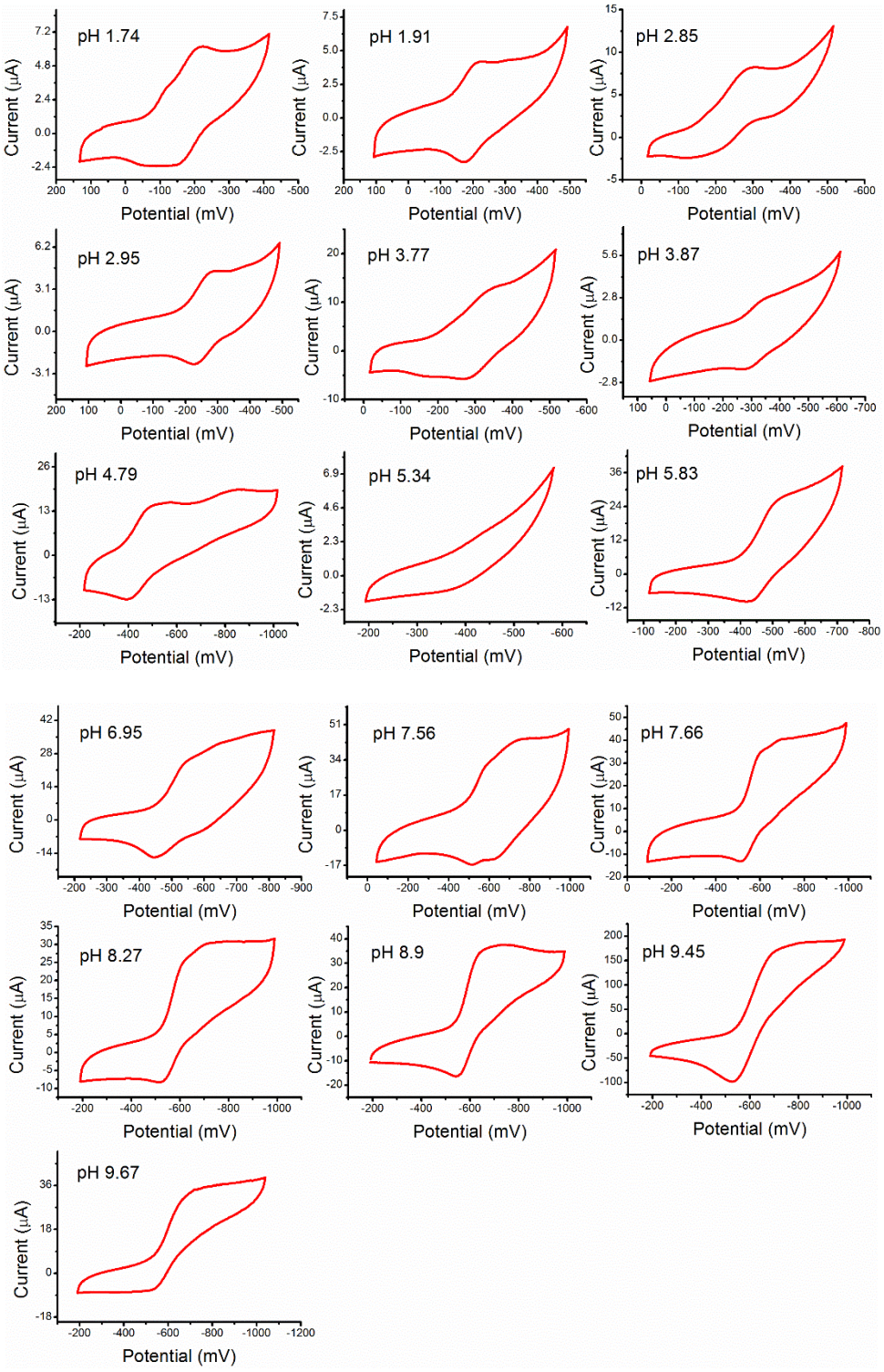

Figure S2.19: Cyclic voltammograms (slurry modified GC electrode, 100 mV s^{-1}, 0.1 M HEPES buffer in water as supporting electrolyte) of **2,6-Zr-AQ-MOF** at different pH

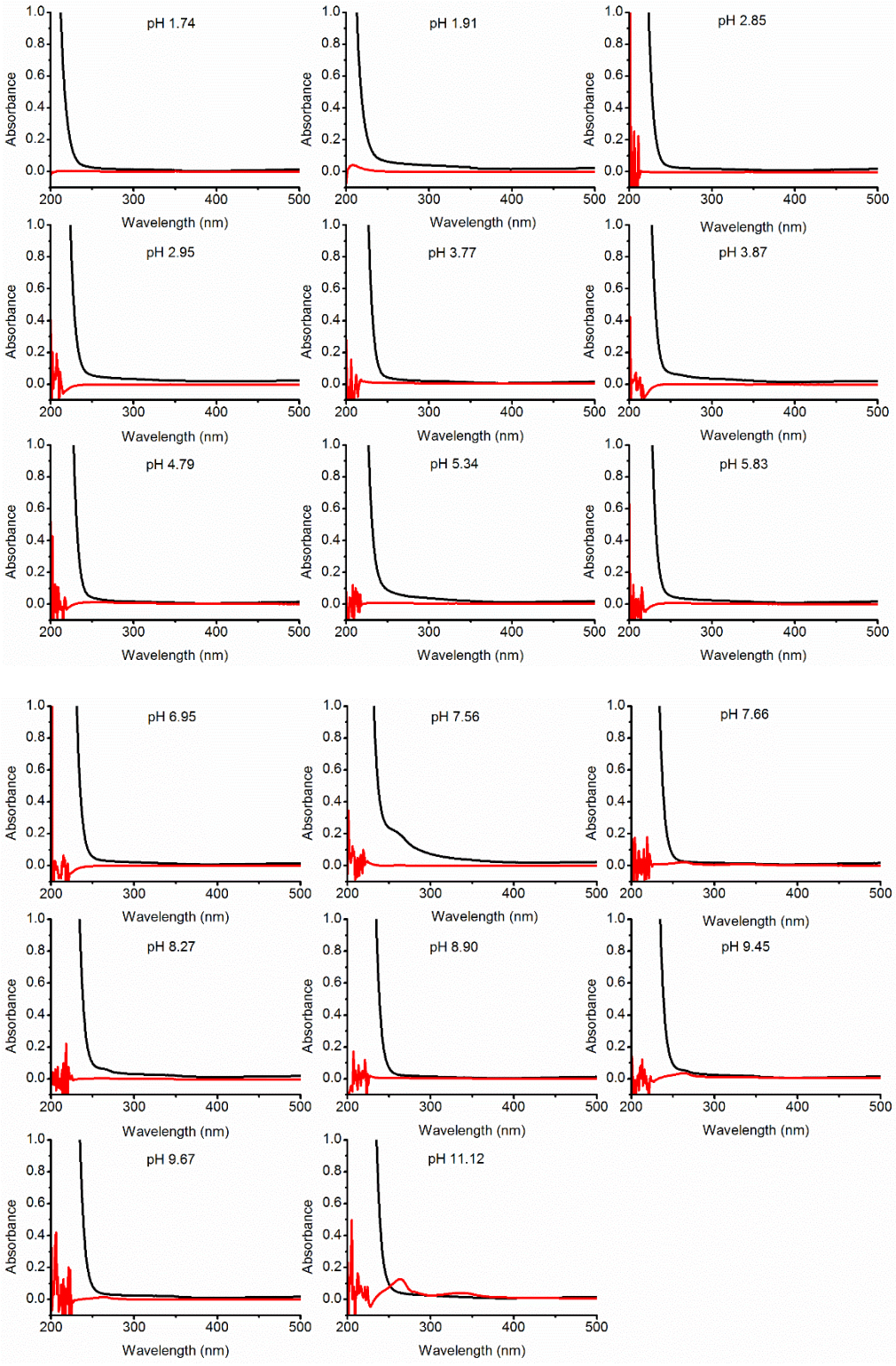

Figure S2.20: Stability of **2,6-Zr-AQ-MOF** upon CV analysis at different pH. Black – HEPES solution before CV, Red – HEPES solution after CV. 2,6-Zr-AQ-MOF is unstable at pH > 9.67

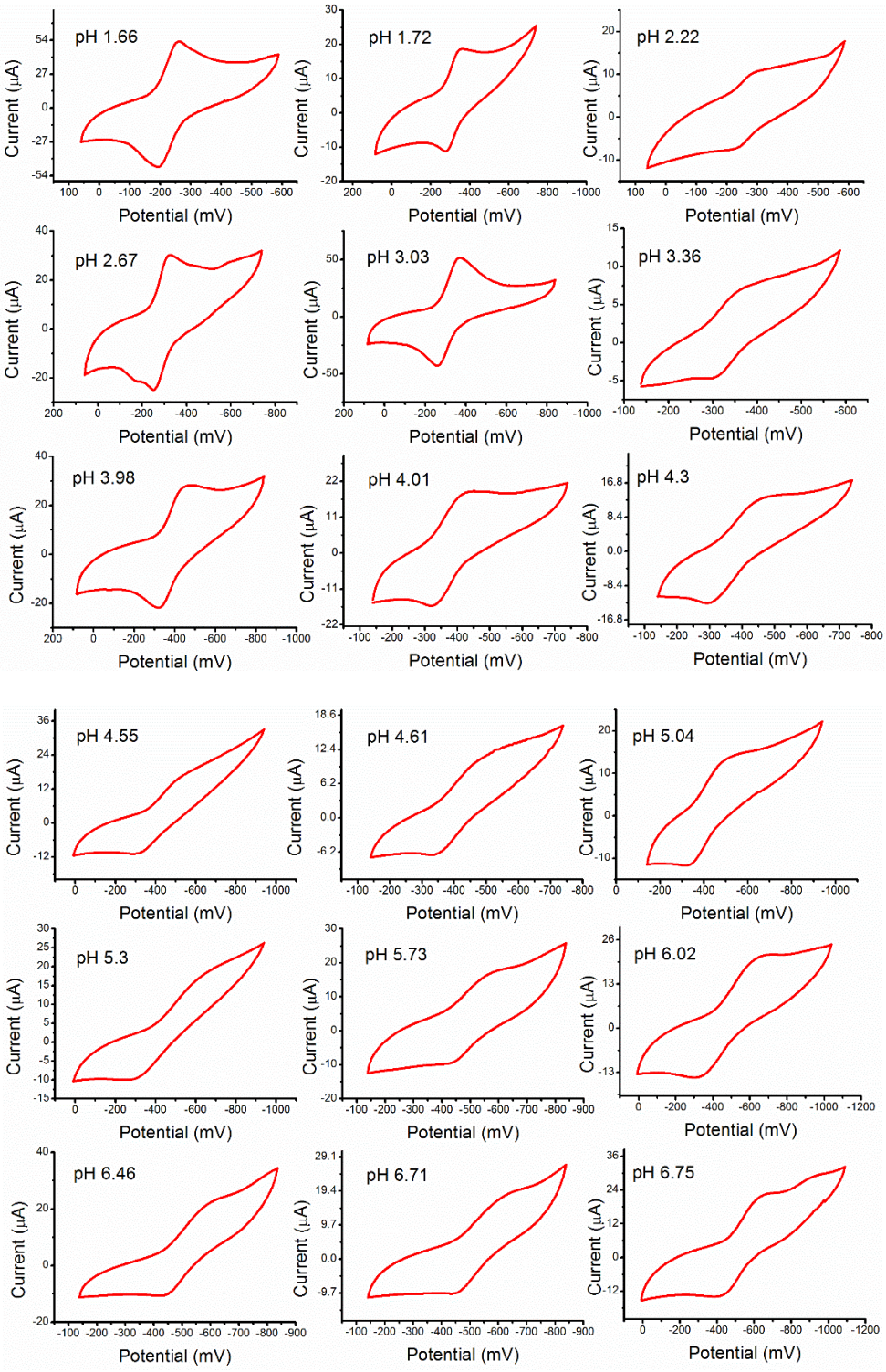

Figure S2.21: Cyclic voltammograms (slurry modified GC electrode, 100 mV s^{-1}, 0.1 M HEPES buffer in water as supporting electrolyte) of **1,4-Zr-AQ-MOF** at different pH

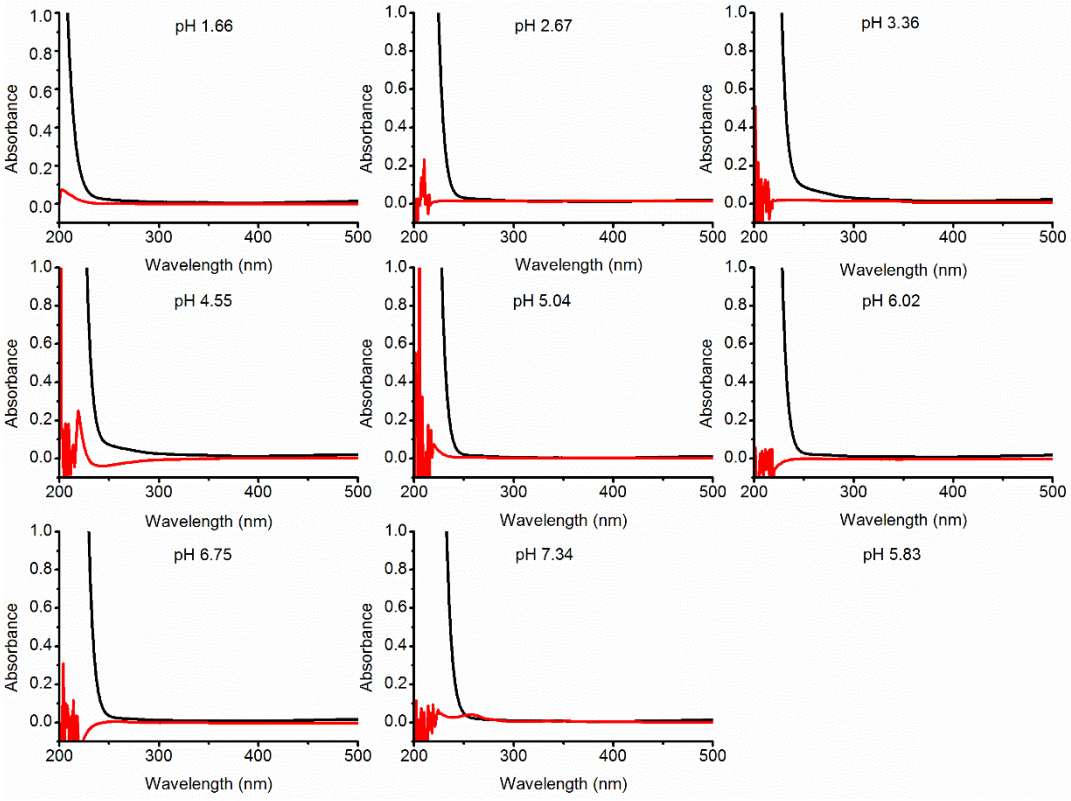

Figure S2.22: Stability of **1,4-Zr-AQ-MOF** upon CV analysis at different pH. Black – HEPES solution before CV, Red – HEPES solution after CV. 1,4-Zr-AQ-MOF is unstable at pH > 6.75

2.6.7 Determination of MOFs defects by NMR

The experimental determination of the defects of **1,4-Zr-AQ-MOF** was achieved by following a similar procedure described in the literature.[39] A sample of 1.22 mg of **1,4-Zr-AQ-MOF** was placed in an NMR tube, where 600 µL of a 50 mM KOH solution in D_2O were added. The mixture was sonicated for 30 min and heated at 85 °C. A quantitative ^1H NMR was taken, showing the signals of the ligand, acetic acid, and formic acid (Figure S2.23). The molar ratio of total modulator to ligand was calculated according to established equations reported in the literature:[34]

$$\frac{Total\ modulator}{Ligand} = \frac{Acetic\ Acid}{Ligand} + \frac{Formic\ Acid}{Ligand}$$

$$\frac{Acetic\ Acid}{Ligand} = \frac{Integration\ Acetic\ Acid}{Equivalent\ ^1H\ nuclei\ Ac.Acid} * \frac{Equivalent\ ^1H\ nuclei\ Ligand}{Integration\ Ligand}$$

$$\frac{Formic\ Acid}{Ligand} = \frac{Integration\ Formic\ Acid}{Equivalent\ ^1H\ nuclei\ For.Acid} * \frac{Equivalent\ ^1H\ nuclei\ Ligand}{Integration\ Ligand}$$

where $\boldsymbol{Equivalent\ ^1H\ nuclei}$ is the number of equivalent ^{1}H nuclei contributing to the ^{1}H NMR signal per molecule. For example, the ^{1}H signal of acetic acid originates from its CH3 group in which all 3 protons are equivalent, therefore $\boldsymbol{Equivalent\ ^1H\ nuclei\ Ac.Acid = 3}$. Similarly, $\boldsymbol{Equivalent\ ^1H\ nuclei\ For.Acid = 1}$ and $\boldsymbol{Equivalent\ ^1H\ nuclei\ Ligand = 6}$. Replacing the numerical $\boldsymbol{Integration}$ value of the signals for the ligand, acetic acid, and formic acid obtained from the ^{1}H NMR spectra (Figure S2.23), the molar ratios can be expressed as:

$$\frac{Acetic\ Acid}{Ligand} = \frac{1.94}{3} * \frac{6}{(1.93 + 2.00 + 1.96)} = 0.66$$

$$\frac{Formic\ Acid}{Ligand} = \frac{0.29}{1} * \frac{6}{(1.93 + 2.00 + 1.96)} = 0.30$$

$$\frac{Total\ modulator}{Ligand} = 0.66 + 0.30 = 0.96$$

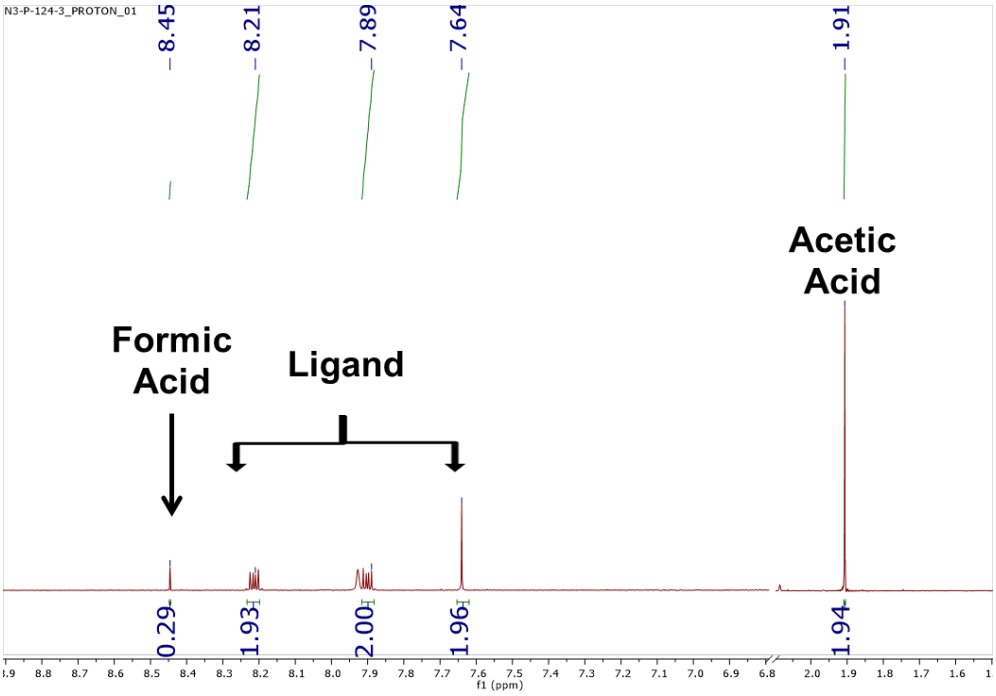

Figure S2.23: ^{1}H NMR spectra obtained for digested **1,4-Zr-AQ-MOF**

2.6.8 Elemental Analysis (C, N, H) of the MOFs

The C, N, H elemental analysis of both MOFs is shown below.

Table S2.1: Elemental Analysis of **2,6-Zr-AQ-MOF** and **1,4-Zr-AQ-MOF**

	2,6-Zr-AQ-MOF	**1,4-Zr-AQ-MOF**
%C	43.08	34.46
%N	5.38	3.83
%H	4.69	4.08

The **2,6-Zr-AQ-MOF** initial molecular formula was $\mathbf{Zr_6O_4(OH)_4(C_{16}O_6H_6)_6}$, based on the typical formula of a UiO-type framework. However, the framework can also host guest molecules such as DMF and water. Using the software *CHN+: calculator*[4] as a tool for estimating the amount of guest molecules in the MOF and correlating these results with the TGA analysis of **2,6-Zr-AQ-**

MOF (Figure S2.13)**,** the formula was found to be **$Zr_6O_4(OH)_4(C_{16}O_6H_6)_6(C_3H_7NO)_{17}(H_2O)_{22}$.** This molecular formula provides a theoretical 43.24% of Carbon, 5.83% of Nitrogen, and 5.01% of Hydrogen, which are in good agreement (less than 0.5% error) with the elemental analysis provided in **Table S2.1**. The normalized TGA of **2,6-Zr-AQ-MOF** (Figure S2.24) revealed a 67.18% of solvent lost, which is in agreement with the 67.04% of weight of DMF and H_2O in the formula **$Zr_6O_4(OH)_4(C_{16}O_6H_6)_6(C_3H_7NO)_{17}(H_2O)_{22}$.**

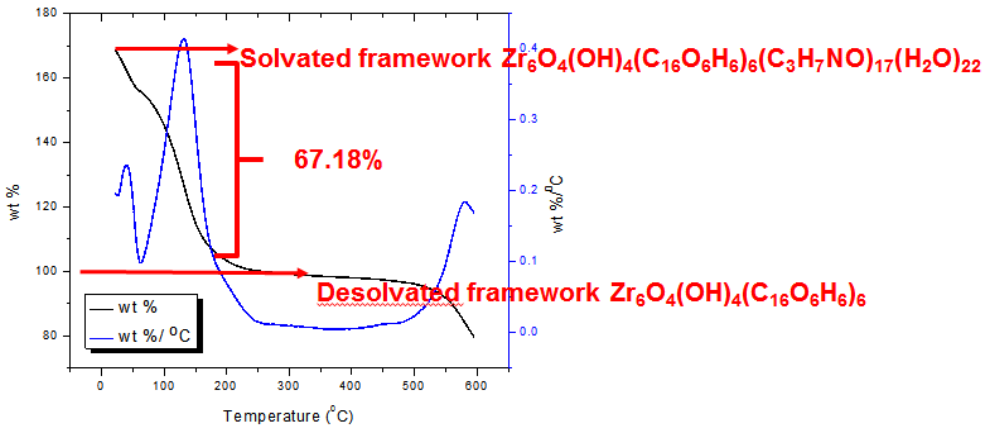

Figure S2.24: Normalized TGA of **2,6-Zr-AQ-MOF**

The initial molecular formula of the highly defective **1,4-Zr-AQ-MOF** was **$Zr_6O_4(OH)_4(C_{16}O_6H_6)_4(C_2O_2H_3)_{2.76}(CO_2H)_{1.24}$**, according to the NMR analysis shown in Figure S2.23. However, the amount of DMF and water in the framework was also estimated by correlating the elemental analysis and TGA (Figure S2.13)**,** to obtain a molecular formula of **$Zr_6O_4(OH)_4(C_{16}O_6H_6)_4(C_2O_2H_3)_{2.76}(CO_2H)_{1.24}$ $(C_3H_7NO)_{11}(H_2O)_{40}$**. According to this formula the theoretical percentage of Carbon is 34.62% and the percentage of Nitrogen is 4.28% which are in good agreement with the percentages obtained experimentally (**Table S**2.**1**). The theoretical percentage of Hydrogen in the formula is 5.45%, which is 1.37% higher from the one obtained in the elemental analysis. The presence of many hydrogen donors and acceptors in the framework (ligand, modulators, and hydroxyl groups in the node) may account for this variability in the

percentage of hydrogen. The normalized TGA of **1,4-Zr-AQ-MOF** (Figure S2.25) revealed a 77.80% of solvent lost, which is in agreement with the 73.5% of weight of DMF and H_2O in the formula $\mathbf{Zr_6O_4(OH)_4(C_{16}O_6H_6)_4(C_2O_2H_3)_{2.76}(CO_2H)_{1.24}\,(C_3H_7NO)_{11}(H_2O)_{40}}$.

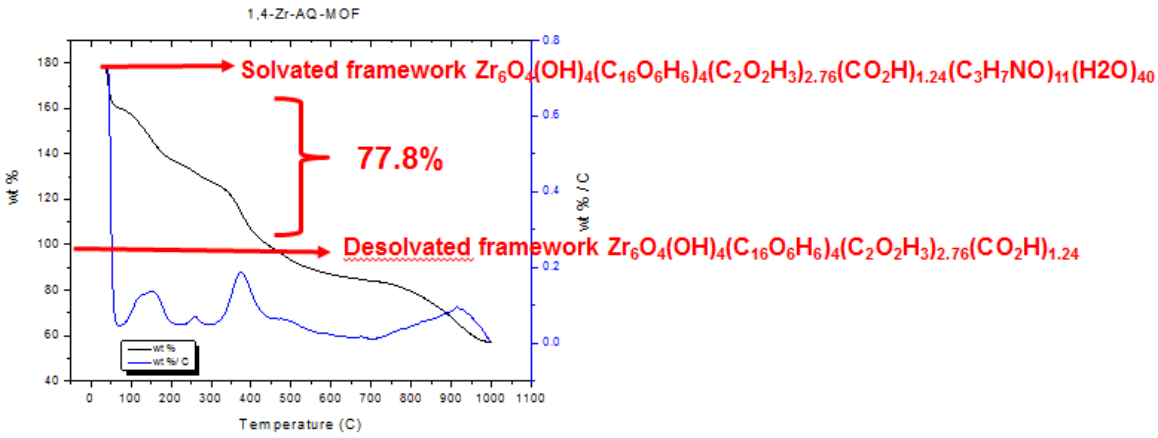

Figure S2.25: Normalized TGA of **1,4-Zr-AQ-MOF**

2.7 ACKNOWLEDGMENTS

This material is based upon work supported by the National Science Foundation under Grant No. 1551964

2.8 REFERENCES

1. Allendorf, M. D.; Schwartzberg, A.; Stavila, V.; Talin, A. A. A roadmap to implementing metal-organic frameworks in electronic devices: challenges and critical directions. *Chemistry* **2011,** 17 (41), 11372-88 DOI: 10.1002/chem.201101595.

2. DeBlase, C. R.; Hernández-Burgos, K.; Silberstein, K. E.; Rodríguez-Calero, G. G.; Bisbey, R. P.; Abruña, H. D.; Dichtel, W. R. Rapid and Efficient Redox Processes within 2D Covalent Organic Framework Thin Films. *ACS Nano* **2015,** 9 (3), 3178-3183 DOI: 10.1021/acsnano.5b00184.

3. Sun, L.; Miyakai, T.; Seki, S.; Dincă, M. Mn2(2,5-disulfhydrylbenzene-1,4-dicarboxylate): A Microporous Metal–Organic Framework with Infinite (−Mn–S−)∞ Chains and High Intrinsic Charge Mobility. *Journal of the American Chemical Society* **2013,** 135 (22), 8185-8188 DOI: 10.1021/ja4037516.

4. Narayan, T. C.; Miyakai, T.; Seki, S.; Dincă, M. High Charge Mobility in a Tetrathiafulvalene-Based Microporous Metal–Organic Framework. *Journal of the American Chemical Society* **2012,** 134 (31), 12932-12935 DOI: 10.1021/ja3059827.

5. Ahrenholtz, S. R.; Epley, C. C.; Morris, A. J. Solvothermal Preparation of an Electrocatalytic Metalloporphyrin MOF Thin Film and its Redox Hopping Charge-Transfer Mechanism. *Journal of the American Chemical Society* **2014,** 136 (6), 2464-2472 DOI: 10.1021/ja410684q.

6. Cavka, J. H.; Jakobsen, S.; Olsbye, U.; Guillou, N.; Lamberti, C.; Bordiga, S.; Lillerud, K. P. A New Zirconium Inorganic Building Brick Forming Metal Organic Frameworks with Exceptional Stability. *Journal of the American Chemical Society* **2008,** 130 (42), 13850-13851 DOI: 10.1021/ja8057953.

7. DeCoste, J. B.; Peterson, G. W.; Jasuja, H.; Glover, T. G.; Huang, Y.-g.; Walton, K. S. Stability and degradation mechanisms of metal-organic frameworks containing the Zr6O4(OH)4 secondary building unit. *Journal of Materials Chemistry A* **2013,** 1 (18), 5642-5650 DOI: 10.1039/C3TA10662D.

8. Guin, P. S.; Das, S.; Mandal, P. C. Electrochemical Reduction of Quinones in Different Media: A Review. *International Journal of Electrochemistry* **2011,** 2011, 22 DOI: 10.4061/2011/816202.

9. Guin, P. S.; Das, S.; Mandal, P. Electrochemical reduction of sodium 1, 4-dihydroxy-9, 10-anthraquinone-2-sulphonate in aqueous and aqueous dimethyl formamide mixed solvent: a cyclic voltammetric study. *Int. J. Electrochem. Sci* **2008,** 3 (9), 1016-1028.

10. DeBlase, C. R.; Silberstein, K. E.; Truong, T.-T.; Abruña, H. D.; Dichtel, W. R. β-Ketoenamine-Linked Covalent Organic Frameworks Capable of Pseudocapacitive Energy Storage. *Journal of the American Chemical Society* **2013,** 135 (45), 16821-16824 DOI: 10.1021/ja409421d.

11. Chandra, S.; Roy Chowdhury, D.; Addicoat, M.; Heine, T.; Paul, A.; Banerjee, R. Molecular Level Control of the Capacitance of Two-Dimensional Covalent Organic Frameworks: Role of Hydrogen Bonding in Energy Storage Materials. *Chemistry of Materials* **2017,** 29 (5), 2074-2080 DOI: 10.1021/acs.chemmater.6b04178.

12. Gui, B.; Meng, X.; Chen, Y.; Tian, J.; Liu, G.; Shen, C.; Zeller, M.; Yuan, D.; Wang, C. Reversible Tuning Hydroquinone/Quinone Reaction in Metal–Organic Framework: Immobilized Molecular Switches in Solid State. *Chemistry of Materials* **2015,** 27 (18), 6426-6431 DOI: 10.1021/acs.chemmater.5b02648.

13. Zhang, Z.; Yoshikawa, H.; Awaga, K. Monitoring the Solid-State Electrochemistry of Cu(2,7-AQDC) (AQDC = Anthraquinone Dicarboxylate) in a Lithium Battery: Coexistence of Metal and Ligand Redox Activities in a Metal–Organic Framework. *Journal of the American Chemical Society* **2014,** 136 (46), 16112-16115 DOI: 10.1021/ja508197w.

14. Zhang, Z.; Yoshikawa, H.; Awaga, K. Discovery of a “Bipolar Charging” Mechanism in the Solid-State Electrochemical Process of a Flexible Metal–Organic Framework. *Chemistry of Materials* **2016,** 28 (5), 1298-1303 DOI: 10.1021/acs.chemmater.5b04075.

15. Halls, J. E.; Ahn, S. D.; Jiang, D.; Keenan, L. L.; Burrows, A. D.; Marken, F. Proton uptake vs. redox driven release from metal–organic-frameworks: Alizarin red S reactivity in UMCM-1. *Journal of Electroanalytical Chemistry* **2013,** 689, 168-175 DOI: http://dx.doi.org/10.1016/j.jelechem.2012.11.016.

16. Halls, J. E.; Jiang, D.; Burrows, A. D.; Kulandainathan, M. A.; Marken, F. In *Electrochemistry: Volume 12*; The Royal Society of Chemistry: 2014; Vol. 12, pp 187-210.

17. Klet, R. C.; Liu, Y.; Wang, T. C.; Hupp, J. T.; Farha, O. K. Evaluation of Bronsted acidity and proton topology in Zr- and Hf-based metal-organic frameworks using potentiometric acid-base titration. *Journal of Materials Chemistry A* **2016,** 4 (4), 1479-1485 DOI: 10.1039/C5TA07687K.

18. Cabellero, A. G.; Croft, A. K.; Nalli, S. M. Remote aromatic stabilization in radical reactions. *Tetrahedron Letters* **2008,** 49 (22), 3613-3615 DOI: http://dx.doi.org/10.1016/j.tetlet.2008.04.009.

19. Arient, J.; Podstata, J. Nitration and oxidation of anthraquinone dimethyl derivatives. *Collect. Czech. Chem. Commun.* **1974,** 39 (11), 3117-3123.

20. Garay, R. O.; Naarmann, H.; Muellen, K. Synthesis and characterization of poly(1,4-anthrylenevinylene). *Macromolecules* **1994,** 27 (7), 1922-1927 DOI: 10.1021/ma00085a040.

21. Bon, V.; Senkovska, I.; Weiss, M. S.; Kaskel, S. Tailoring of network dimensionality and porosity adjustment in Zr- and Hf-based MOFs. *CrystEngComm* **2013,** 15 (45), 9572-9577 DOI: 10.1039/C3CE41121D.

22. Furman, N. H.; Stone, K. G. A Polarographic Study of Certain Anthraquinones1. *Journal of the American Chemical Society* **1948,** 70 (9), 3055-3061 DOI: 10.1021/ja01189a064.

23. Zhu, Z. W.; Li, N. Q. Electrochemical studies of the interaction of 9,10-anthraquinone with DNA 1. Hanging mercury drop electrode. *Microchemical Journal* **1998,** 59 (2), 294-306 DOI: 10.1006/mchj.1998.1576.

24. Ojani, R.; Raoof, J.; Ebranimi, M. A cyclic voltammetric study of the aqueous electrochemistry of some anthraquinone derivatives on carbon paste electrode. *Iranian Journal of Chemistry and Chemical Engineering (IJCCE)* **2001,** 20 (2), 75-81.

25. Petrova, S. A.; Kolodyazhny, M. V.; Ksenzhek, O. S. Electrochemical properties of some naturally occurring quinones. *Journal of Electroanalytical Chemistry and Interfacial Electrochemistry* **1990,** 277 (1), 189-196 DOI: http://dx.doi.org/10.1016/0022-0728(90)85101-A.

26. Raoof, D. B.; Golabi, S. M. Electrochemical Properties of Carbon-Paste Electrodes Spiked with Some 1,4-Naphthoquinone Derivatives. *Bulletin of the Chemical Society of Japan* **1995,** 68 (8), 2253-2261 DOI: 10.1246/bcsj.68.2253.

27. Driebergen, R. J.; Den Hartigh, J.; Holthuis, J. J. M.; Hulshoff, A.; van Oort, W. J.; Postma Kelder, S. J.; Verboom, W.; Reinhoudt, D. N.; Bos, M.; van der Linden, W. E. Electrochemistry of potentially bioreductive alkylating quinones. *Analytica Chimica Acta* **1990,** 233, 251-268 DOI: http://dx.doi.org/10.1016/S0003-2670(00)83486-8.

28. Örnskov, E.; Linusson, A.; Folestad, S. Determination of dissociation constants of labile drug compounds by capillary electrophoresis. *Journal of Pharmaceutical and Biomedical Analysis* **2003,** 33 (3), 379-391 DOI: http://dx.doi.org/10.1016/S0731-7085(03)00238-3.

29. Nemkevich, A.; Spackman, M. A.; Corry, B. Mechanism of Concerted Hydrogen Bond Reorientation in Clathrates of Dianin's Compound and Hydroquinone. *Journal of the American Chemical Society* **2011,** 133 (46), 18880-18888 DOI: 10.1021/ja206962f.

30. Ilczyszyn, M.; Selent, M.; Ilczyszyn, M. M. Participation of Xenon Guest in Hydrogen Bond Network of β-Hydroquinone Crystal. *The Journal of Physical Chemistry A* **2012,** 116 (12), 3206-3214 DOI: 10.1021/jp210670k.

31. Salazar, R.; Vidal, J.; Martinez-Cifuentes, M.; Araya-Maturana, R.; Ramirez-Rodriguez, O. Electrochemical characterization of hydroquinone derivatives with different substituents in acetonitrile. *New Journal of Chemistry* **2015,** 39 (2), 1237-1246 DOI: 10.1039/C4NJ01657B.

32. Astudillo, P. D.; Valencia, D. P.; González-Fuentes, M. A.; Díaz-Sánchez, B. R.; Frontana, C.; González, F. J. Electrochemical and chemical formation of a low-barrier proton transfer complex between the quinone dianion and hydroquinone. *Electrochimica Acta* **2012,** 81, 197-204 DOI: http://dx.doi.org/10.1016/j.electacta.2012.07.078.

33. Wu, H.; Chua, Y. S.; Krungleviciute, V.; Tyagi, M.; Chen, P.; Yildirim, T.; Zhou, W. Unusual and Highly Tunable Missing-Linker Defects in Zirconium Metal–Organic Framework UiO-66 and Their Important Effects on Gas Adsorption. *Journal of the American Chemical Society* **2013,** 135 (28), 10525-10532 DOI: 10.1021/ja404514r.

34. Shearer, G. C.; Chavan, S.; Bordiga, S.; Svelle, S.; Olsbye, U.; Lillerud, K. P. Defect Engineering: Tuning the Porosity and Composition of the Metal–Organic Framework UiO-66 via Modulated Synthesis. *Chemistry of Materials* **2016,** 28 (11), 3749-3761 DOI: 10.1021/acs.chemmater.6b00602.

35. Cliffe, M. J.; Wan, W.; Zou, X.; Chater, P. A.; Kleppe, A. K.; Tucker, M. G.; Wilhelm, H.; Funnell, N. P.; Coudert, F. X.; Goodwin, A. L. Correlated defect nanoregions in a metal-organic framework. *Nat Commun* **2014,** 5, 4176 DOI: 10.1038/ncomms5176.

36. Øien, S.; Wragg, D.; Reinsch, H.; Svelle, S.; Bordiga, S.; Lamberti, C.; Lillerud, K. P. Detailed Structure Analysis of Atomic Positions and Defects in Zirconium Metal–Organic Frameworks. *Crystal Growth & Design* **2014,** 14 (11), 5370-5372 DOI: 10.1021/cg501386j.

37. Usov, P. M.; Ahrenholtz, S. R.; Maza, W. A.; Stratakes, B.; Epley, C. C.; Kessinger, M. C.; Zhu, J.; Morris, A. J. Cooperative electrochemical water oxidation by Zr nodes and Ni-porphyrin linkers of a PCN-224 MOF thin film. *Journal of Materials Chemistry A* **2016,** 4 (43), 16818-16823 DOI: 10.1039/C6TA05877A.

38. Brunauer, S.; Emmett, P. H.; Teller, E. Adsorption of Gases in Multimolecular Layers. *Journal of the American Chemical Society* **1938,** 60 (2), 309-319 DOI: 10.1021/ja01269a023.

39. Liang, W.; Coghlan, C. J.; Ragon, F.; Rubio-Martinez, M.; D'Alessandro, D. M.; Babarao, R. Defect engineering of UiO-66 for CO2 and H2O uptake - a combined experimental and simulation study. *Dalton Transactions* **2016,** 45 (11), 4496-4500 DOI: 10.1039/C6DT00189K.

3. Charge Storage and Quinone Accessibility in Anthraquinone-based Zirconium Metal-Organic Frameworks

Paula J. Celis-Salazar, Linqin Mu, Connor Slamowitz, Feng Lin, Amanda J. Morris*

3.1 ABSTRACT

The previously reported metal-organic frameworks (MOFs) 2,6-Zr-AQ-MOF and 1,4-Zr-AQ-MOF were assembled into two different types of working electrodes: a slurry-modified glassy carbon electrode, and as solvothermally-grown MOF thin films. The specific capacitance and the percentage of quinone accessed in the two frameworks were calculated for the two types of electrodes using cyclic voltammetry in aqueous buffered media as a function of pH. Both frameworks showed an enhanced capacitance and quinone accessibility in the thin films as compared to the powder-based electrodes, while revealing that the structural differences between 2,6-Zr-AQ-MOF and 1,4-Zr-AQ-MOF in terms of defectivity and the number of electrons and protons transferred were directly influencing the percentage of active quinones and the ability of the materials to store charge. The non-defective 2,6-Zr-AQ-MOF displayed higher quinone accessibility and capacitance at pH > pKa, where the protonated dianion formed from a two-electron, one-proton transfer, facilitated the charge storage in a higher extent than its hydroquinone analogue formed at pH < pKa. In contrast, the highly defective 1,4-Zr-AQ-MOF showed better performance at pH < pKa, due to linker to node hydrogen bonding interactions that assisted higher capacitance and quinone access via a two-electron, three-proton transfer. The maximum specific capacitance observed was in the order of 1.68 F g^{-1} and the highest quinone accessibility was of

0.6%, exhorting the necessity to improve the thin film assembly strategies to create more efficient charge transport pathways.

3.2 INTRODUCTION

Supercapacitors are energy storage devices of great importance for the electrical–based technologies arising from the necessity of a transition to a more sustainable, and low-emission society.[1] The study of materials capable of exhibiting pseudocapacitance, where the charge-storage ability is due to the electrochemical activity of redox moieties in the material, has become predominant in the last years.[2] Metal-organic frameworks (MOFs), a class of porous materials consisting in inorganic nodes connected by organic ligands, are proper candidates for showing pseudocapacitance properties, due to their high surface area, well-organized pores, and their exceptional tunability advantage that allow the introduction of redox functionalities in the core structure, providing potential charge storage capabilities.[1, 3, 4]

Quinone moieties are an example of functionalities that show reversible redox behavior and the ability to achieve proton-coupled electron transport (PCET).[5] Recently, we reported the PCET of two UiO-type zirconium MOFs (2,6-Zr-AQ-MOF and 1,4-Zr-AQ-MOF) containing anthraquinone ligands, that exhibited different electrochemical response in aqueous electrolyte as a function of the pH.[6] Essentially, structural differences such as the positioning of the quinone moiety with respect to the zirconium node, the amount of defects, and the ability to undergo hydrogen bonding, have an important effect on the PCET processes during cyclic voltammetry experiments of slurry-modified electrodes containing these frameworks.[6] Nevertheless, the understanding of the pseudocapacitance performance and the quinone accessibility during the different PCET processes is vital to use these materials in energy storage devices.

One of the latest advances on the application of MOFs in electronic platforms, is the assembly of these frameworks in conductive electrodes as thin films.[7] Unlike the slurry-modified electrodes, solvothermally grown MOF thin films allow direct contact with the electrolyte solution during cyclic voltammetry analysis, and prevent any permeability effects of the polymer present in the slurry-modified electrode in pH-dependence studies. More importantly, the thin film electrodes allow the spontaneous growth of the MOF in its crystalline form, facilitating pathways for redox hopping, without the addition of other conductive materials, such as graphite.[8] A positive performance of thin film electrodes has been recently observed in quinone-based covalent-organic frameworks (COFs),[9, 10] where the assembly of two-dimensional frameworks in thin films provided more efficient quinone accessibility and capacitance as compared to the randomly oriented slurry-modified electrodes.[4, 11]

In the present study, we sought to investigate the capacitance and quinone accessibility of 2,6-Zr-AQ-MOF and 1,4-Zr-AQ-MOF in two different types of electrodes (powder-based and solvothermally grown conductive thin films) in aqueous electrolyte at a variety of pH. The ability of the materials to store charge was also tested by charge-discharge potential profiles on coin cells containing the frameworks. The results of this study encourage further research on improving thin film manufacture in order to obtain more efficient charge transport paths.

3.3 EXPERIMENTAL SECTION

3.3.1 Synthesis of 2,6-dicarboxy-9,10-anthhraquinone

The synthesis of this ligand was achieved according to previous reports.[6, 12, 13] A mixture of benzoquinone (3.25 g, 30 mmol), isoprene (10.0 mL) and traces of hydroquinone, in absolute ethanol (20.0 mL) was heated at 130 °C for 6 h in a metal autoclave. After cooling to room temperature, the mixture was added to a potassium hydroxide solution in ethanol (8.5 g of KOH

in 200 mL of EtOH). The solution was stirred under air for 8 h at 40 °C, for 12 h at room temperature, and for 2h at 50 °C. A white solid was obtained after filtration in vacuum at room temperature. Subsequently, the solid was suspended in absolute ethanol and left at 0 °C overnight. After filtration and multiple washes with cold ethanol and water the solid was dried under air to afford 2,6-dimethyl-9,10-anthraquinone.[6, 12] The 2,6-dimethyl-9,10-anthraquinone (1.0 g) was suspended in 12.0 mL of an aqueous solution of 25% nitric acid. The mixture was placed in a 40.0 mL autoclave and heated slowly until reaching 220 °C, where the temperature was maintained for 3 h. After cooling to room temperature and filtered under vacuum, a yellow powder was obtained and washed with water. The solid was dried overnight, affording pure 2,6-dicarboxy-9,10-anthhraquinone with 69% yield.[6, 13] ^{1}H NMR (400 MHz, DMSO): δ 13.77 (s, 2H), 8.69(dd, J= 1.8 Hz, 0.4 Hz, 2H), 8.44(dd, J=8 Hz, 1.8Hz, 2H), 8.36(d,d J= 8 Hz, 0.4 Hz, 2H). HRMS: $(M+H)^+$: 297.0375.

3.3.2 Synthesis of 1,4-dicarboxy-9,10-anthhraquinone

The synthesis of this ligand was achieved by following previous procedures.[6, 13, 14] A mixture of 1,4-naphthoquinone (9.35 g, 0.059 mol), 2,4-hexadiene (5.0 g, 0.605 mol), and toluene (35 mL) was heated and stirred at 65°C for 4 days. After evaporation of the solvent, the remaining oily solid (15.0 g) was dissolved in absolute ethanol (250 mL), and added to a solution of KOH in ethanol (30 g in 1.25 L) at 10 °C. Subsequently, oxygen was bubbled through the solution at 10 °C for 1 h. After evaporation of the solvent, the semisolid residue was dissolved in 600 mL of water and extracted with benzene. Removal of the organic solvent afforded 1,4-dimethyl-9,10-anthraquinone with 70% yield.[20] The 1,4-dimethyl-9,10-anthraquinone (1.0 g) was suspended in 12.0 mL of an aqueous solution of 25% nitric acid. The mixture was placed in a 40.0 mL autoclave and heated slowly until reaching 220 °C, where the temperature was maintained for 3 h. After

cooling to room temperature and filtered under vacuum, a yellow powder was obtained and washed with water. The solid was dried overnight, affording pure 1,4-dicarboxy-9,10-anthhraquinone with 69% yield.[6, 13] ^{1}H NMR (400 MHz, DMSO): δ 13.37 (s, 2H), 8.19 (dd, J=5.6 Hz, 3.2 Hz, 2H), 7.99 (dd, J=5.6 Hz, 3.2 Hz, 2H), 7.89 (s, 2H). HRMS: $(M+H)^+$: 297.0376.

3.3.3 Synthesis of 2,6-Zr-AQ MOF $[Zr_6O_4(OH)_4(C_{16}O_6H_6)_6\,(C_3H_7NO)_{17}(H_2O)_{22}]$

A solution of $ZrCl_4$ (23.0 mg, 0.1 mmol) in 2.0 mL of DMF was sonicated for 5 minutes. Subsequently, the ligand 2,6-dicarboxy-9,10-anthraquinone (29.6 mg, 0.1 mmol) and 0.3 mL of acetic acid (47 equiv.) were added to the solution. The mixture was sonicated for 15 minutes and held at 120 °C for 24 h. The 2,6-Zr-AQ-MOF was obtained as a pink powder and isolated by three cycles of centrifugation alternated with washes with fresh DMF. The MOF was dried under vacuum at room temperature (Yield 31.3 mg, 75 %).[6]

3.3.4 Synthesis of 1,4- Zr-AQ-MOF $[Zr_6O_4(OH)_4(C_{16}O_6H_6)_4(C_2O_2H_3)_{2.76}(CO_2H)_{1.24}(C_3H_7NO)_{11}(H_2O)_{40}]$

A mixture of $ZrCl_4$ (23.0 mg, 0.1 mmol), the ligand 1,4-dicarboxy-9,10-anthraquinone (29.6 mg, 0.1 mmol), acetic acid (1.2 mL, 200 equiv.) and DMF (3.0 mL) was sonicated for 15 minutes. The solution was heated at 120 °C for 48 h. The mixture was cooled to room temperature at a rate of 1 °C/min. The 1,4-Zr-AQ-MOF was obtained as a pink powder, which was isolated by three cycles of centrifugation alternated with washes with fresh DMF. The MOF was dried under vacuum at room temperature (Yield 30.0 mg, 72 %).[6]

3.4 RESULTS AND DISCUSSION

The solvothermal synthesis of 2,6-Zr-AQ-MOF $[Zr_6O_4(OH)_4(C_{16}O_6H_6)_6(C_3H_7NO)_{17}(H_2O)_{22}]$ and 1,4-Zr-AQ-MOF $[Zr_6O_4(OH)_4(C_{16}O_6H_6)_4(C_2O_2H_3)_{2.76}(CO_2H)_{1.24}(C_3H_7NO)_{11}(H_2O)_{40}]$ was achieved by following a previously reported procedure.[6] Explicitly, the 2,6-Zr-AQ-

MOF was obtained by the addition of 2,6-dicarboxy-9,10-anthhraquinone and acetic acid (47 equiv.) to a solution of $ZrCl_4$ in DMF, followed by a static heating at 120 °C for 1 day. Likewise, the treatment of 1,4-dicarboxy-9,10-anthhraquinone and $ZrCl_4$ in a mixture of acetic acid (200 equiv.) and DMF (1:2.5 by volume) at 120 °C for 2 days afforded 1,4-Zr-AQ-MOF.[6]

The powder X-ray diffraction (PXRD) patterns of 2,6-Zr-AQ-MOF and 1,4-Zr-AQ-MOF are consistent with the ones reported before for these two frameworks (Figure 3.1).[6] On one hand, the non-defective 2,6-Zr-AQ-MOF displays the typical PXRD peaks at low angle characteristic of UiO-type frameworks. On the other hand, the high defectivity of 1,4-Zr-AQ-MOF is confirmed by the broad peak at 2θ range of *ca.* 3-6°, which has been assigned as a fingerprint of missing node defects in UiO frameworks.[6, 15, 16]

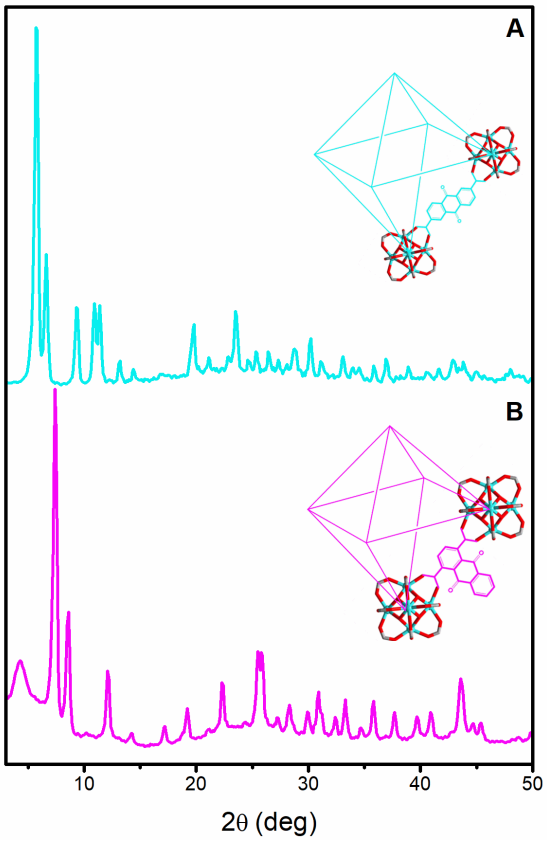

Figure 3.1. PXRD patterns and schematic structural representation of A) **2,6-Zr-AQ-MOF** and B) **1,4-Zr-AQ-MOF**.

Cyclic voltammetry of the anthraquinone frameworks was performed using two different types of working electrodes: 1) A dried slurry of the MOF powder (10 mg), graphite (10 mg), poly-methyl methacrylate (3.34 mg), and THF (1 mL), deposited on a GC electrode, and 2) the solvothermally synthesized MOF, grown as a thin film on a conductive FTO slide. The two working electrodes were used separately in a three-electrode assembly, with a HEPES-buffered aqueous solution as supporting electrolyte (see SI for details). CV measurements were taken over the pH range of chemical stability of both MOFs (pH < 9.67 for 2,6-Zr-AQ-MOF, and pH < 6.75 for 1,4-Zr-AQ-MOF).[6] It has been reported before that the 2,6-Zr-AQ-MOF has an electrochemical pKa of 7.56 for the transition between a two-electron, two-proton transfer (at pH < pKa) and a two-electron, one-proton transfer (at pH > pKa).[6] Similarly, a pKa of 5.18 for 1,4-Zr-AQ-MOF divides the transition from a two-electron, three-proton transfer (at pH < pKa) to a two-electron, one-proton transfer (at pH > pKa).[6]

The cyclic voltammograms of 2,6-Zr-AQ-MOF and 1,4-Zr-AQ-MOF in the slurry modified electrode and as thin films, over the pH range studied, showed a reversible redox process which shifted to more negative potential with increasing pH (Figure 3.2). For both MOFs the current of the reductive wave was higher in the thin films (Figure 3.2 E-H) than in the slurry modified electrode (Figure 3.2 A-D). We sought to calculate the percentages of accessible electroactive quinones moieties in the slurry and the films, by using the integrated charge of the reductive wave of the cyclic voltammograms (shaded area in Figure 3.2). At a certain scan rate, the charge corresponds to the integration of the current over the range of potential where the wave is observed, according to the expression:

$$Q = \frac{\int_{E_1}^{E_2} I \, dE}{v} \qquad \textbf{(3.1)}$$

where Q is the charge, I is the current, E is the potential, E_1 and E_2 are the potentials comprising the reductive wave, and υ is the scan rate. The theoretical charge was calculated by determining the number of quinone sites available in the slurry modified electrode and the thin films. The quinones available in the slurry were obtained from the concentration of MOF in the original graphite-MOF- PMMA solution. Similarly, ICP analysis of the digested films for determination of Zr, allowed the calculation of the quinone moieties in the thin films (see SI for detailed calculations). For each range of pH, the CV experiments were repeated three times on different slurry modified electrodes or films, in order to obtain the average percentages of accessible quinones and the correspondent statistical error (see SI for detailed electrochemical procedures).

Remarkably, both 2,6-Zr-AQ-MOF and 1,4-Zr-AQ-MOF revealed different percentages of accessible electroactive quinones moieties at the lower and higher pH range (Figure 3.3 A-B). The 2,6-Zr-AQ-MOF showed lower quinones accessed (0.003% - 0.03%) at pH 1.5 - 7.0, while higher quinones accessed (0.08% - 0.14%) at pH 7.0 - 9.67 (Figure 3.3A). Since the 2,6-Zr-AQ-MOF has an electrochemical pKa of 7.56, at pH < pKa the two-electron, two-proton transfer from quinone to hydroquinone[6] on the ligands of this framework takes place with a low accessibility of quinone sites in the slurry modified electrode. At pH > pKa, the ligands of this MOF undergo a two-electron, one-proton transfer, from quinone to protonated dianion.[6] This process appeared to be assisted by a higher electronic accessibility to the MOF quinones sites in the same type of electrode (Figure 3.3A).

Conversely, the 1,4-Zr-AQ-MOF displayed higher quinones accessed (0.09% - 0.11%) at pH 1.5 - 4.5, while lower quinones accessed (0.02% - 0.03%) at pH 4.5 - 6.75 (Figure 3.3B). This fact suggests that at pH lower than the pKa of 1,4-Zr-AQ-MOF (pKa = 5.18)[6] the two-electron,

three-proton transfer is carried out with a higher accessibility to the quinone sites, as compared to the two-electron, one-proton transfer (at pH > pKa),[6] where the percentage of quinones active is lower (Figure 3.3B). Additionally, a similar pKa trend was observed for the specific capacitance of the slurry modified electrode of both frameworks.

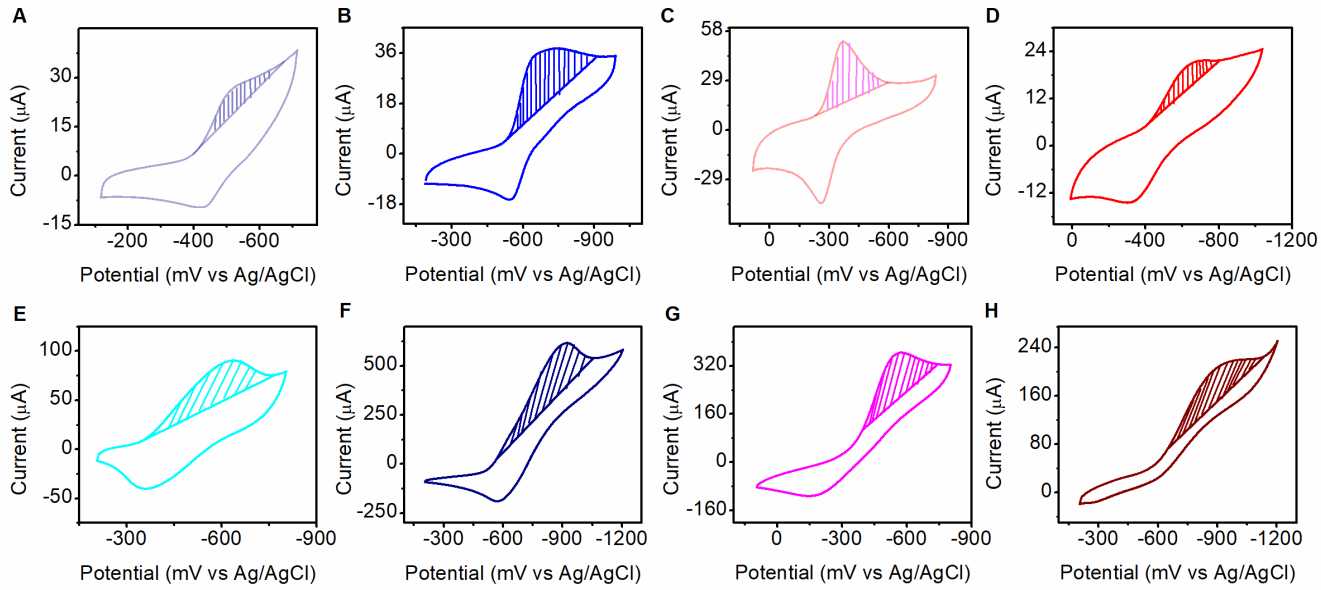

Figure 3.2. Cyclic voltammograms (100 mV s^{-1}, 0.1 M HEPES buffer as supporting electrolyte) of: ***Top:*** the slurry modified electrode of A) **2,6-Zr-AQ-MOF** at pH < pKa, B) **2,6-Zr-AQ-MOF** at pH > pKa, C) **1,4-Zr-AQ-MOF** at pH < pKa, D) **1,4-Zr-AQ-MOF** at pH > pKa, ***Bottom:*** the thin films of E) **2,6-Zr-AQ-MOF** at pH < pKa, F) **2,6-Zr-AQ-MOF** at pH > pKa, G) **1,4-Zr-AQ-MOF** at pH < pKa, H) **1,4-Zr-AQ-MOF** at pH > pKa. *Shaded Area*: The integrated charge of the reductive wave

The specific capacitance was calculated from the integration of their cyclic voltammograms at the same pH values (see SI), using the expression:

$$C = \frac{\int I\, dE}{2 * \Delta E * \upsilon * m} \qquad \textbf{(3.2)}$$

where C is the capacitance, I is the current, E is the potential, ΔE is the potential window for the CV, υ is the scan rate, and m is the mass of the MOF. The 2,6-Zr-AQ-MOF exhibited specific capacitance around 0.15 - 0.55 F g^{-1}, at pH 1.5 - 7.0 F g^{-1}, and higher specific capacitance

values (0.45 - 0.78 F g^{-1}) at pH 7.0 - 9.67 (Figure 3.3C). On the other hand, the 1,4-Zr-AQ-MOF revealed specific capacitance of 0.76 - 0.79 F g^{-1} at pH 1.5 - 4.5 (Figure 3.3D), while at pH 4.5 - 6.75 the specific capacitance was lower (0.48 - 0.56 F g^{-1}).

The pKa dependence of the accessible quinone sites and capacitance for both MOFs in their identically prepared slurry modified electrodes, suggests that the structural differences between 2,6-Zr-AQ-MOF and 1,4-Zr-AQ-MOF in terms of defectivity and PCET processes (number of electrons and proton transferred at pH < pKa, and pH > pKa) are directly influencing the accessibility to quinone sites and the ability of the materials to store charge. Remarkably, the non-defective 2,6-Zr-AQ-MOF showed a better performance at pH > pKa, revealing that the protonated dianion,[6] formed from the two-electron, one-proton transfer, provides stability to store charge in a higher extent than the hydroquinone analogue formed at pH < pKa. This behavior is similar to the one observed by anthraquinone COFs, where higher quinone accessibility was achieved in aprotic solvents than in a very acidic environment.[4] In contrast, the highly defective 1,4-Zr-AQ-MOF showed higher accessibility and capacitance at pH < pKa, revealing that the hydrogen bonding resultant from the cooperative behavior between node and linker to achieve the two-electron, three-proton transfer,[6] is indeed facilitating charge transfer. The stabilization by intramolecular hydrogen bonding displaying high capacitance and accessibility, was also previously observed in a quinone COF material.[10]

Although the tridimensional uniformity and crystalline nature of MOF materials is supposed to facilitate efficient charge transport,[4, 10] other effects may take an influential role in this type of slurry modified electrodes. For instance, the MOF particles are randomly dispersed in a mixture with graphite, and the PMMA polymer is a barrier between the mixture and the electrolyte. The solvothermal growth of MOF thin films provides a platform for studying the capacitance of

these materials in their crystalline form without the addition of graphite, and avoiding any permeability effects of the polymer in pH-dependence studies.

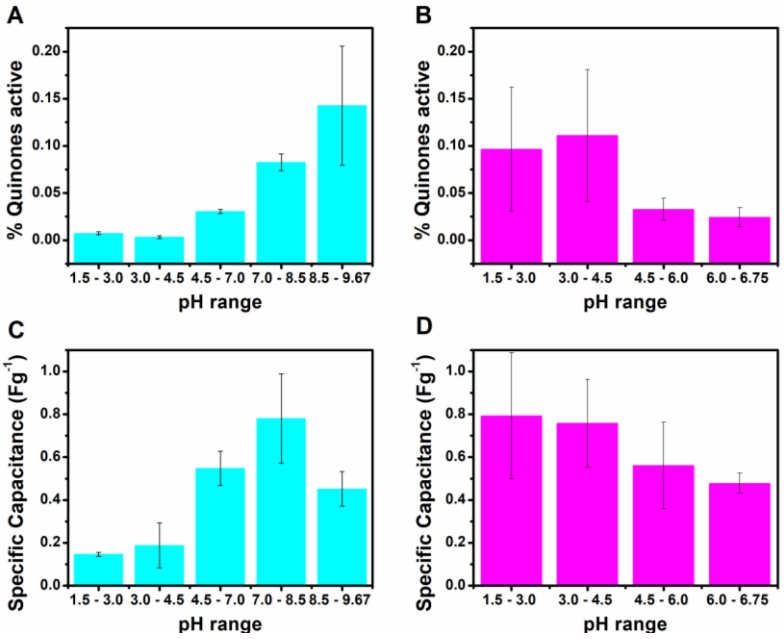

Figure 3.3. ***Top:*** Percentage of quinones active in the slurry modified electrode of A) **2,6-Zr-AQ-MOF** and B) **1,4-Zr-AQ-MOF** at different pH. ***Bottom:*** Specific capacitance of the slurry modified electrode of C) **2,6-Zr-AQ-MOF** D) **1,4-Zr-AQ-MOF** at different pH.

However, the same pKa-dependence trend in terms of percentage of quinone accessed and specific capacitance was observed in the thin films (Figure 3.4). The 2,6-Zr-AQ-MOF (pKa 7.56) showed lower quinones accessed (0.03% - 0.08%) at pH 1.5 - 7.0, while higher quinones accessed (0.2% - 0.6%) at pH 7.0 - 9.67 (Figure 3.4A). Additionally, the 1,4-Zr-AQ-MOF (pKa 5.18) revealed higher quinone accessed (0.41% - 0.50%) at pH 1.5 – 4.5, and lower quinone accessed (0.01% - 0.28%) at pH 4.5 – 6.75 (Figure 3.4B). Moreover, the capacitance of the 2,6-Zr-AQ-MOF thin films was lower at pH 1.5 - 7.0 (around 0.35 - 0.45 F g^{-1}) and higher (around 0.96 – 1.63 F g^{-1}) at pH 7.0 - 9.67 (Figure 3.4C). Conversely, the 1,4-Zr-AQ-MOF films revealed specific capacitance of 1.60 – 1.68 F g^{-1} at pH 1.5 - 4.5 (Figure 3.4D), while at pH 4.5 - 6.75 the specific capacitance was lower (0.82 F g^{-1}).

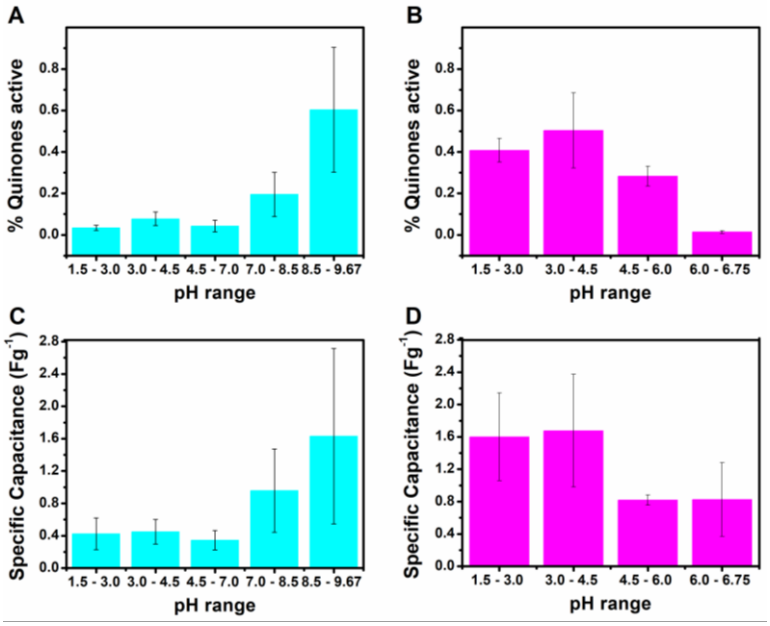

Figure 3.4. ***Top:*** Percentage of quinones active in the films of A) **2,6-Zr-AQ-MOF** and B) **1,4-Zr-AQ-MOF** at different pH. ***Bottom:*** Specific capacitance of the films of C) **2,6-Zr-AQ-MOF** D) **1,4-Zr-AQ-MOF** at different pH

The percentages of quinones accessed in the thin films of both MOFs (Figure 3.4 A-B) are in the order of 3 or 10 times higher than the ones displayed in the slurry modified electrodes (Figure 3.3 A-B). Similarly, the capacitance values of the films of both frameworks (Figure 3.4 C-D) are approximately twice in magnitude than the ones observed in the slurry modified electrodes (Figure 3.3 C-D). These facts confirm that the well-organized and crystalline structure of the MOF thin films allow higher quinone accessibility and increase the charge transfer performance, as compared to the electrodes built with a randomly oriented MOF powder.[4]

The thin films and slurry modified electrodes of both 2,6-Zr-AQ-MOF and 1,4-Zr-AQ-MOF show higher values of specific capacitance than many MOFs reported in the literature, such as UiO-66, MIL-100, MIL-101, ZIF-8, and ZIF-67 (0.002 -0.133 F g^{-1}).[17] However, these values are lower than the highest capacitance values reported for MOFs in the literature.[18-20] Interestingly, the percentages of accessible quinone sites and specific capacitance of the films of both quinone

MOFs are considerably lower than those reported in the literature for 2-D quinone COF based materials.[4, 9, 10] This fact suggests that the stacking of layers may create paths for conductivity, where the thickness of the films have a crucial role.[4] The films synthesized in this study have an approximate thickness of 1 μm, while the 2-D COF films reported in the literature are usually in the nanometric range.[4] We anticipate that varying the amount of modulator on the solvothermally-grown MOF thin films, could potentially provide a difference in the thickness and crystallinity of the films, where paths for electron and proton transfer could be optimized.

Lastly, in order to check the performance of both the 2,6-Zr-AQ-MOF and 1,4-Zr-AQ-MOF as active materials in batteries, we assembled coin cells of both frameworks (see SI) and obtained their charge-discharge potential profiles as a function of time at 0.1 mA and 0.2 mA using ethanol as the electrolyte (Figure 3.5). Both frameworks showed the characteristic response related to the reduction and oxidation of the anthraquinone ligands in the frameworks over several cycles. Nevertheless, the capacitance behavior seemed limited as compared to coin cells of COFs materials that exhibited an enhanced charge-storage capability due to the addition of conductive moieties by electropolymerization.[11] The distance between anthraquinone ligands in 2,6-Zr-AQ-MOF and 1,4-Zr-AQ-MOF may not be ideal for electrons to hop, as compared to the charge-transport path resulting from the stacking of quinone layers offered by 2D-COF materials.[4]

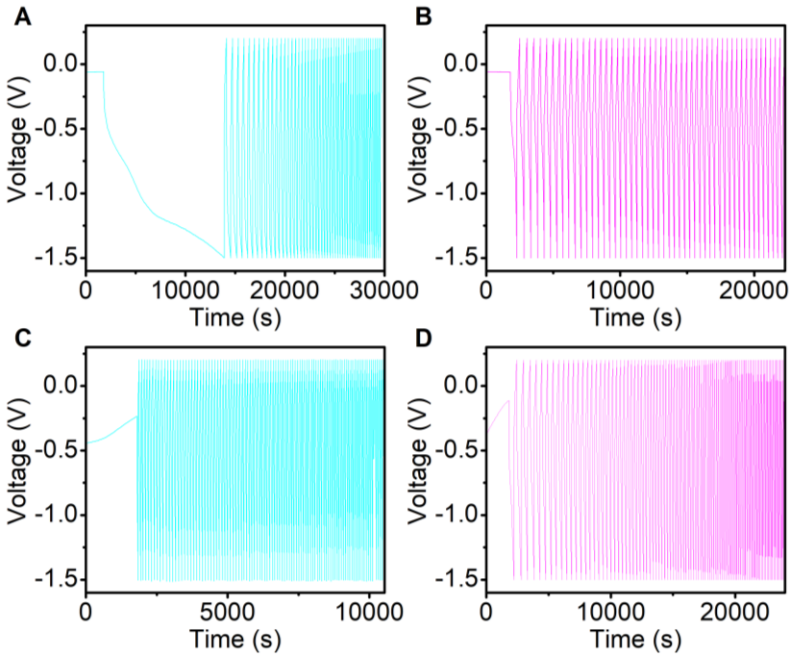

Figure 3.5. Charge-discharge potential profiles for a coin cell assembled with A) 2,6-Zr-AQ-MOF at 0.1 mA B) 1,4-Zr-AQ-MOF at 0.1 mA C) 2,6-Zr-AQ-MOF at 0.2 mA D) 1,4-Zr-AQ-MOF at 0.2 mA

3.5 CONCLUSION

In summary, we have studied the quinone accessibility and specific capacitance in two anthraquinone-based Zr MOFs thin films and slurry modified electrodes, as a function of the pH. The pKa of the frameworks, the defectivity, and the stabilization through hydrogen bonding, showed an important effect on the percentage of quinones active and their ability to store charge in both type of electrodes. While the anthraquinone MOF thin films displayed superior performance than the powder-based electrodes, improving charge transport paths in the films through crystal engineering methods is vital to exploit the potential of these materials as charge transport agents.

3.6 SUPPORTING INFORMATION

3.6.1 Materials and Instrumentation

3.6.1.1 Materials

All reagents and solvents were purchased from commercial sources and used without further purification.

3.6.1.2 Nuclear Magnetic Resonance (NMR)

^{1}H NMR spectra were acquired on a Agilent U4-DD2 spectrometer operating at 400 MHz. Samples were analyzed as solutions in DMSO-d6 (ca. 10 mg mL^{-1}) at 25 °C in standard 5 mm o.d. tubes.

3.6.1.3 Powder X-Ray Diffraction (PXRD)

PXRD measurements were carried out on a Rigaku Miniflex equipped with a Cu(Kα) radiation source (λ=1.5418 Å). The scanning rate was 1°/min using a 2θ range of 3- 50° on continuous mode. The samples were mounted onto reflective disks with a Si (510) surface.

3.6.1.4 Electrochemistry

All electrochemical experiments were performed in a BASi EC Epsilon potentiostat using a standard three-electrode configuration: a working electrode (either a slurry-modified glassy carbon (GC) electrode containing the MOF sample, or a solvothermally grown MOF deposited into a FTO thin film), a high surface area Pt mesh as the counter electrode, and an aqueous Ag/AgCl reference electrode (saturated aqueous KCl). Potassium Ferricyanide was used to calibrate the reference electrode with all the potentials reported vs Ag/AgCl.

3.6.2 Electrochemical Methods

3.6.2.1 Preparation and dropcasting of the slurry modified electrode

A solution of poly-methyl methacrylate (3.34 mg) in 1.0 mL of THF was sonicated for 10 min. Subsequently, 10.0 mg of MOF and 10.0 mg of graphite were added to the solution in order to create a suspension that was stirred for 1 h. The dropcasting was performed by adding 40.0 μL of the slurry in the surface of the glassy carbon electrode, and letting it dry for 20 min. The electrode was polished and re-coated again after every measurement.

3.6.2.2 Preparation of thin films

The films were synthesized solvothermally by introducing a fluorinated tin oxide (FTO) film in the synthesis vial containing the linker, $ZrCl_4$, the modulator, and the DMF solvent (as described in the Experimental section), just before the solution was about to be held at 120 °C. A multimeter was used to differentiate the conductive side of the film, leaving such side facing up during the synthesis.

3.6.2.3 Cyclic voltammetry analysis

Analyses were performed in a standard three-electrode array: Either a slurry modified GC electrode or a MOF thin film, a Ag/AgCl reference, and a Pt mesh. Solutions of 0.1 M HEPES (10.0 mL) buffer at different pH were used as the supporting electrolyte. The pH was adjusted using either HCl or NaOH. Before the experiment was carried out, nitrogen was bubbled for 20 minutes to the solution. Cyclic voltammograms were collected at a scan rate of 100 mV s^{-1} (12 cycles).

For each range of pH, the CV experiments were repeated three times on different slurry modified electrodes or films, in order to obtain the average percentages of accessible quinones and the correspondent statistical error. The cyclic voltammograms obtained in the three repetitions

(series 1, 2, and 3) for both MOFs in the slurry modified electrode and films at the different pH range are shown on Figures S3.1-S3.12.

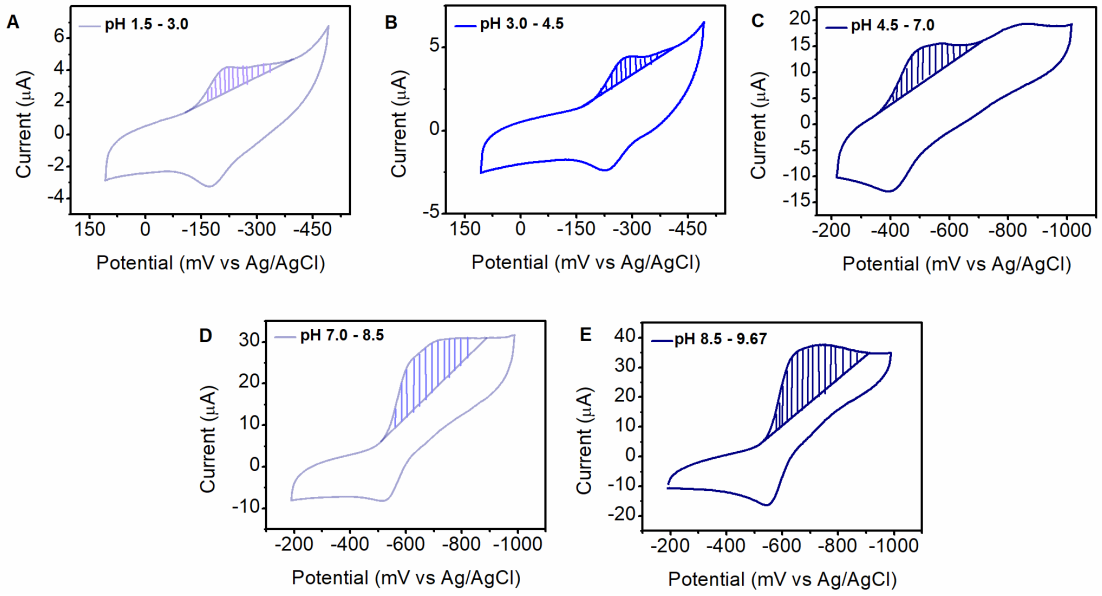

Figure S3.1: Cyclic voltammograms (slurry modified GC electrode - series 1, 100 mV s^{-1}, 0.1 M HEPES buffer in water as supporting electrolyte) of **2,6-Zr-AQ-MOF** at different pH. *Shaded area:* The integrated charge of the reductive wave.

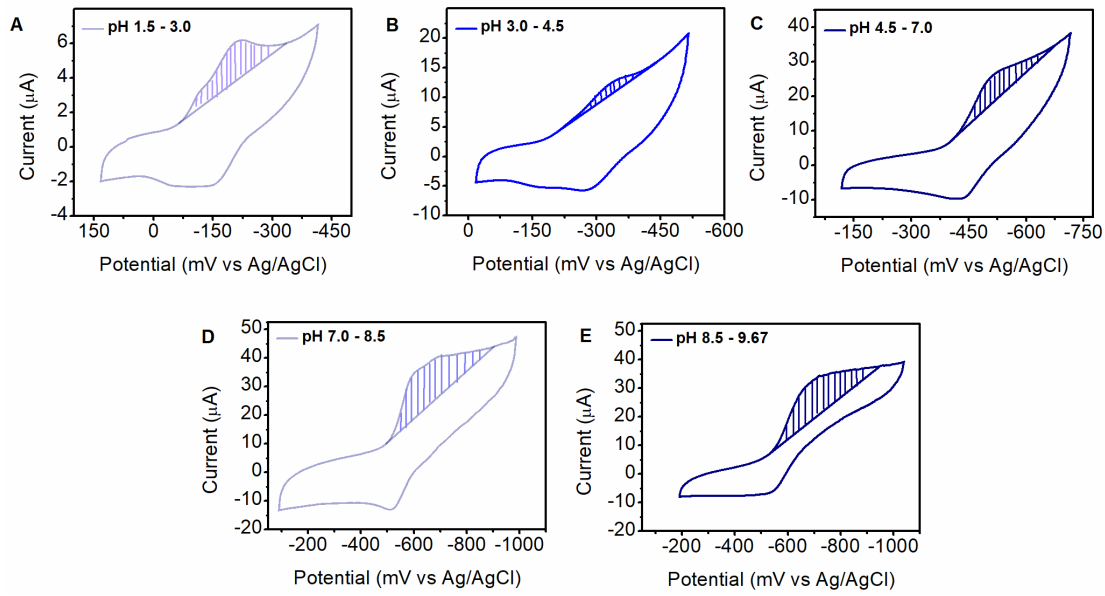

Figure S3.2: Cyclic voltammograms (slurry modified GC electrode - series 2, 100 mV s^{-1}, 0.1 M HEPES buffer in water as supporting electrolyte) of **2,6-Zr-AQ-MOF** at different pH. *Shaded area:* The integrated charge of the reductive wave.

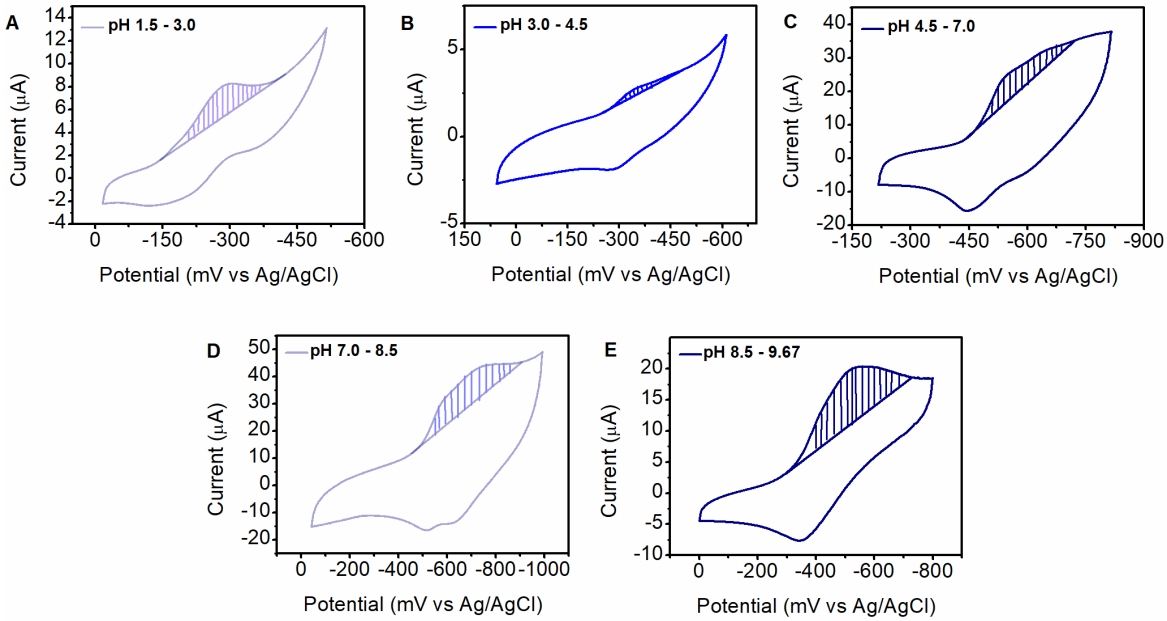

Figure S3.3: Cyclic voltammograms (slurry modified GC electrode - series 3, 100 mV s^{-1}, 0.1 M HEPES buffer in water as supporting electrolyte) of **2,6-Zr-AQ-MOF** at different pH. *Shaded area:* The integrated charge of the reductive wave.

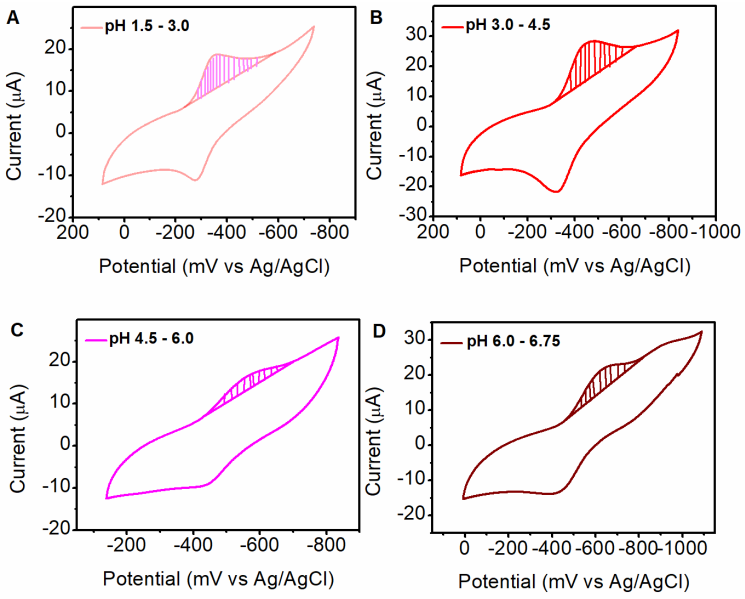

Figure S3.4: Cyclic voltammograms (slurry modified GC electrode - series 1, 100 mV s^{-1}, 0.1 M HEPES buffer in water as supporting electrolyte) of **1,4-Zr-AQ-MOF** at different pH. *Shaded area:* The integrated charge of the reductive wave.

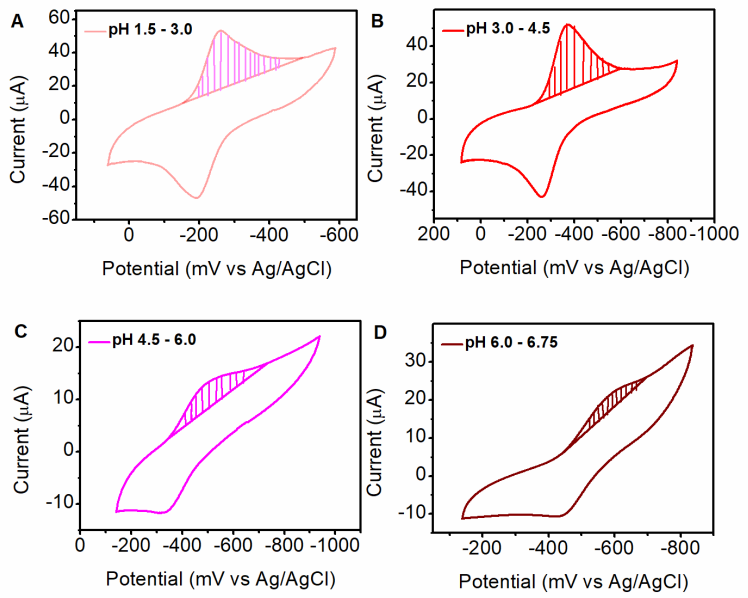

Figure S3.5: Cyclic voltammograms (slurry modified GC electrode - series 2, 100 mV s^{-1}, 0.1 M HEPES buffer in water as supporting electrolyte) of **1,4-Zr-AQ-MOF** at different pH. *Shaded area:* The integrated charge of the reductive wave.

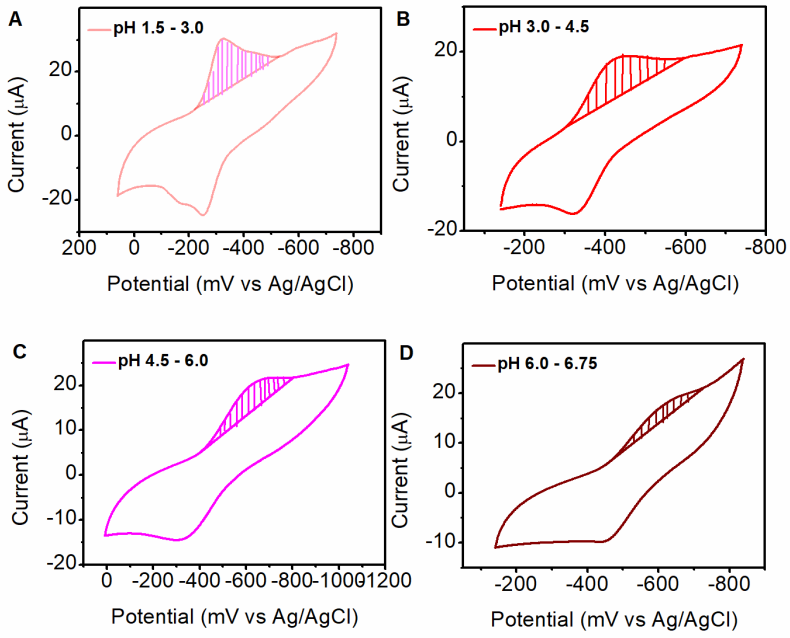

Figure S3.6: Cyclic voltammograms (slurry modified GC electrode - series 3, 100 mV s^{-1}, 0.1 M HEPES buffer in water as supporting electrolyte) of **1,4-Zr-AQ-MOF** at different pH. *Shaded area:* The integrated charge of the reductive wave.

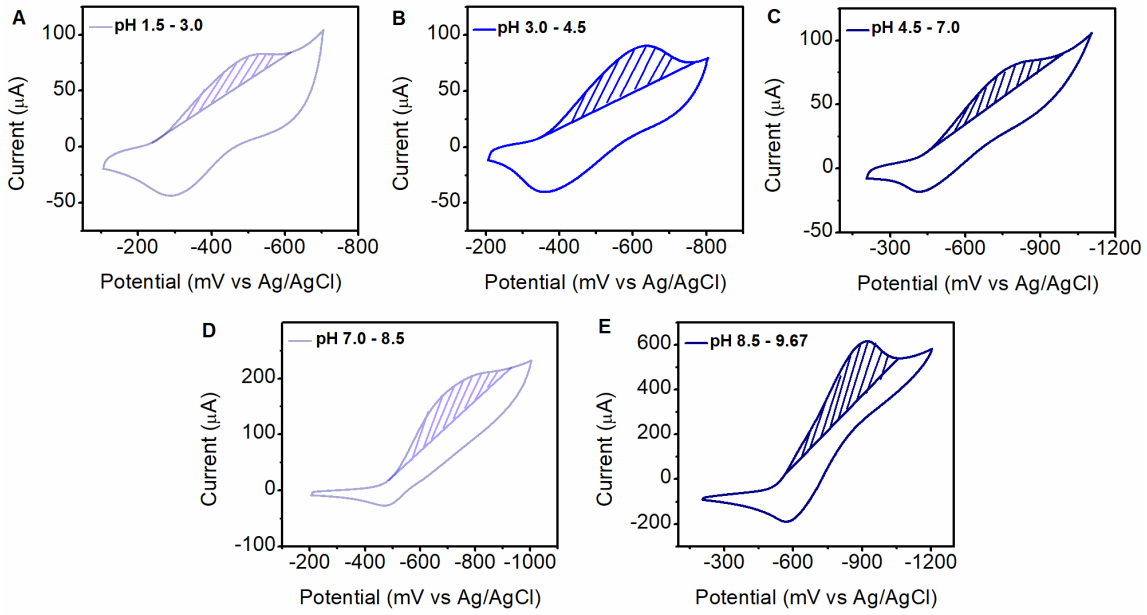

Figure S3.7: Cyclic voltammograms (thin films - series 1, 100 mV s^{-1}, 0.1 M HEPES buffer in water as supporting electrolyte) of **2,6-Zr-AQ-MOF** at different pH. *Shaded area:* The integrated charge of the reductive wave.

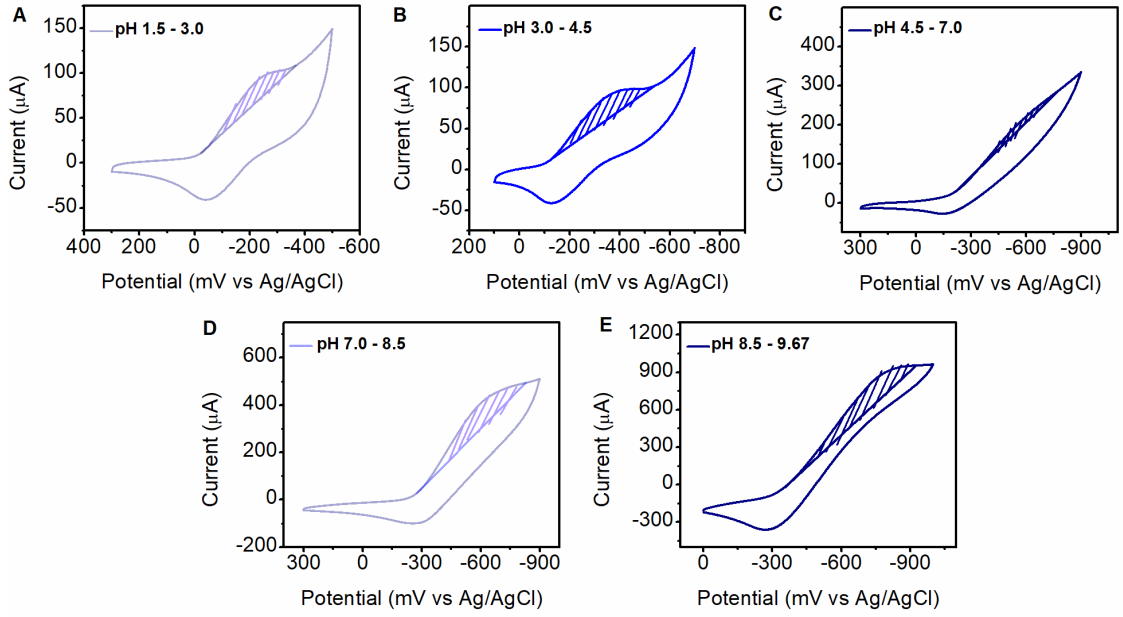

Figure S3.8: Cyclic voltammograms (thin films - series 2, 100 mV s^{-1}, 0.1 M HEPES buffer in water as supporting electrolyte) of **2,6-Zr-AQ-MOF** at different pH. *Shaded area:* The integrated charge of the reductive wave.

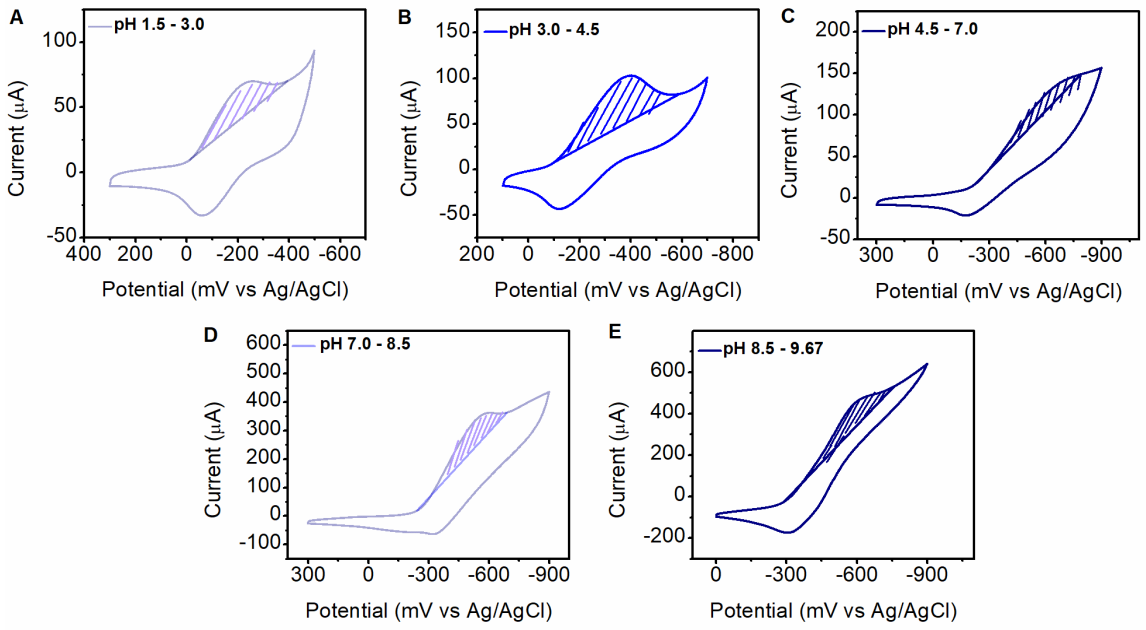

Figure S3.9: Cyclic voltammograms (thin films - series 3, 100 mV s^{-1}, 0.1 M HEPES buffer in water as supporting electrolyte) of **2,6-Zr-AQ-MOF** at different pH. *Shaded area:* The integrated charge of the reductive wave.

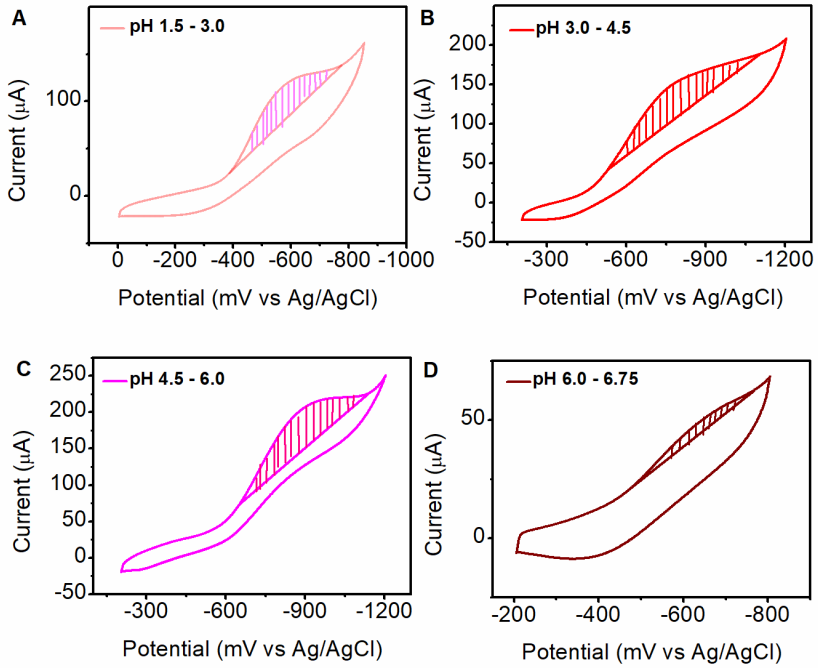

Figure S3.10: Cyclic voltammograms (thin films - series 1, 100 mV s^{-1}, 0.1 M HEPES buffer in water as supporting electrolyte) of **1,4-Zr-AQ-MOF** at different pH. *Shaded area:* The integrated charge of the reductive wave.

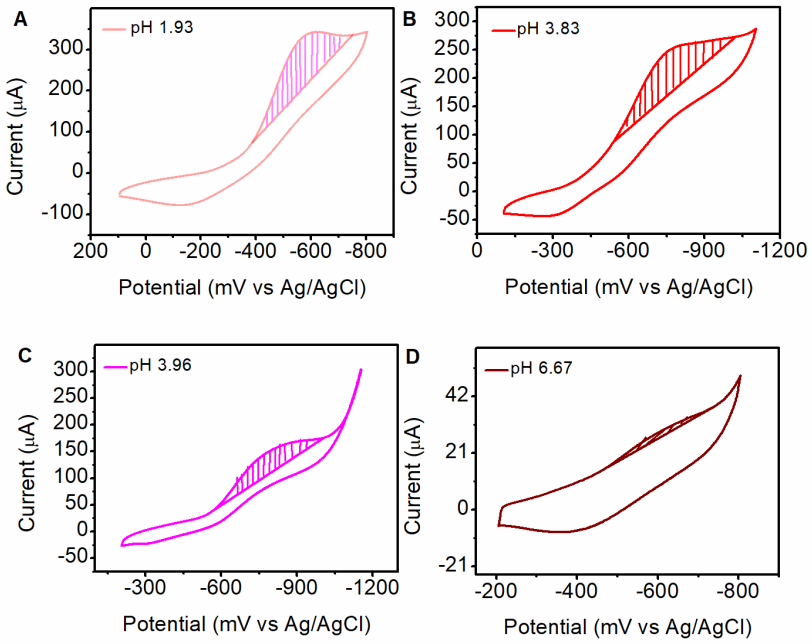

Figure S3.11: Cyclic voltammograms (thin films - series 2, 100 mV s^{-1}, 0.1 M HEPES buffer in water as supporting electrolyte) of **1,4-Zr-AQ-MOF** at different pH. *Shaded area:* The integrated charge of the reductive wave.

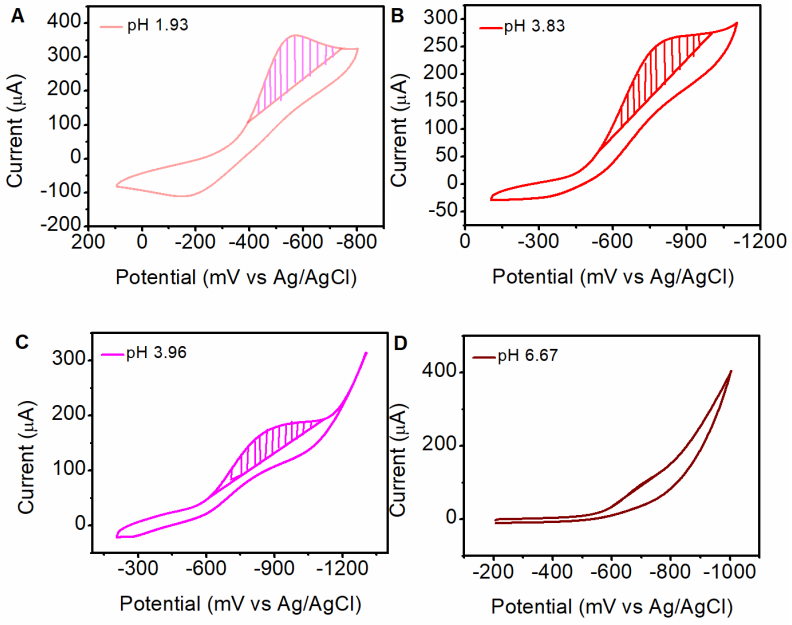

Figure S3.12: Cyclic voltammograms (thin films - series 3, 100 mV s^{-1}, 0.1 M HEPES buffer in water as supporting electrolyte) of **1,4-Zr-AQ-MOF** at different pH. *Shaded area:* The integrated charge of the reductive wave.

3.6.2.3.1 Calculation of % of Quinone active from CV analysis

The percentages of accessible electroactive quinones moieties in the slurry and the films were calculated using the integrated charge of the reductive wave of the cyclic voltammograms (shaded area on Figures S3.1-S3.12). As described in the manuscript, at a certain scan rate, the charge corresponds to the integration of the current over the range of potential were the wave is observed, according to the expression:

$$Q = \frac{\int_{E_1}^{E_2} I \, dE}{v} \qquad \textbf{(3.1)}$$

where Q is the charge, I is the current, E is the potential, E_1 and E_2 are the potentials comprising the reductive wave, and υ is the scan rate.

As an example, for one of the **2,6-Zr-AQ-MOF** slurry-modified GC electrode experiments, at υ= 0.1 Vs^{-1}, the integration of the peak (numerator in equation 1) gave 8.71 E-6 AV. Therefore, the experimental charge of the reductive wave was Q_{exp} = 8.71 E-5 C.

The theoretical charge was calculated by determining the number of quinone sites available in the slurry modified electrode. The concentration of MOF in the original graphite-MOF-PMMA solution was 3.34 mg/mL, and the dropcasting was done by taking 40 µL of such slurry. Since the molecular mass of the MOF is known (4083.58 g/mol), it was determined that there were 3.27 E-5 mmol of **2,6-Zr-AQ-MOF** in the slurry-modified GC electrode. Each mol of MOF contains 6 mol of quinone ligand, and every mol of ligand is able to transfer 2 mol of electrons. Using these facts and the Faraday constant (96485 C mol^{-1}), it was determined a theoretical charge of Q_{theo}= 3.79 E-2 C. Therefore, the percentage of quinone accessed during this particular experiment is calculated as:

$$\%Quinone\ active = \frac{8.71 * 10^{-5}\ C}{3.79\ 10^{-2}\ C} * 100 = 0.23\%$$

The theoretical charge in the case of the thin films was obtained by digesting the MOF thin film in nitric acid, and obtaining the Zr content by ICP analysis. Once more, using the molecular formula of the MOF, the number of quinone ligands was obtained. Using the fact that each ligand transfers two electrons and the Faraday constant, the theoretical charge (Q_{theo}) through the quinone moieties in the thin films is easily calculated.

3.6.2.3.2 Calculation of Specific Capacitance from CV analysis

The specific capacitance was calculated from the integration of the whole CV (all the potential window) by using the equation:

$$C = \frac{\int I \, dE}{2 * \Delta E * v * m} \qquad \textbf{(3.2)}$$

where C is the capacitance, I is the current, E is the potential, ΔE is the potential window for the CV, υ is the scan rate, and m is the mass of the MOF. The mass of the MOF was obtained from the concentration of the framework in the original graphite-MOF-PMMA solution for the slurry-modified electrode, and the ICP analysis of the digested films.

3.6.2.4 Coin cells assembly and tests

The working electrodes were assembled by evenly distributing the active materials (either 2,6-Zr-AQ-MOF or 1,4-Zr-AQ-MOF), acetylene black, and polytetrafluoroethylene (PTFE) with the mass ratio of 75:15:10. This mixture was pressed into a thin film that was cut to small pieces (around 1 cm x 1 cm). The counter electrodes were prepared by mixing active carbon and PTFE with the mass ratio of 90:10, and subsequently pressing the mixture into a thin film, that was also cut to small pieces (around 1 cm x 1 cm). The active mass loadings for working and counter

electrodes were 6 mg/cm^2. Then, all the electrodes were dried in vacuum oven at room-temperature overnight. The CR2032 coin cells were assembled using the working electrodes, counter electrodes, glass fiber as separator, and ethanol as the electrolyte. All coin cells were cycled with an electrochemical workstation (Wuhan Land Company) at 25°C at the constant current of 0.1 - 0.5 mA in the voltage range of -1.5 - 0.2 V.

3.7 ACKNOWLEDGMENTS

This material is based upon work supported by the National Science Foundation under Grant No. 1551964

3.8 REFERENCES

1. Xu, G.; Nie, P.; Dou, H.; Ding, B.; Li, L.; Zhang, X. Exploring metal organic frameworks for energy storage in batteries and supercapacitors. *Materials Today* **2017,** 20 (4), 191-209 DOI: https://doi.org/10.1016/j.mattod.2016.10.003.

2. Wang, G.; Zhang, L.; Zhang, J. A review of electrode materials for electrochemical supercapacitors. *Chemical Society Reviews* **2012,** 41 (2), 797-828 DOI: 10.1039/C1CS15060J.

3. Allendorf, M. D.; Schwartzberg, A.; Stavila, V.; Talin, A. A. A roadmap to implementing metal-organic frameworks in electronic devices: challenges and critical directions. *Chemistry* **2011,** 17 (41), 11372-88 DOI: 10.1002/chem.201101595.

4. DeBlase, C. R.; Hernández-Burgos, K.; Silberstein, K. E.; Rodríguez-Calero, G. G.; Bisbey, R. P.; Abruña, H. D.; Dichtel, W. R. Rapid and Efficient Redox Processes within 2D Covalent Organic Framework Thin Films. *ACS Nano* **2015,** 9 (3), 3178-3183 DOI: 10.1021/acsnano.5b00184.

5. Guin, P. S.; Das, S.; Mandal, P. C. Electrochemical Reduction of Quinones in Different Media: A Review. *International Journal of Electrochemistry* **2011,** 2011, 22 DOI: 10.4061/2011/816202.

6. Celis-Salazar, P. J.; Epley, C. C.; Ahrenholtz, S. R.; Maza, W. A.; Usov, P. M.; Morris, A. J. Proton-Coupled Electron Transport in Anthraquinone-Based Zirconium Metal–Organic Frameworks. *Inorganic Chemistry* **2017,** 56 (22), 13741-13747 DOI: 10.1021/acs.inorgchem.7b01656.

7. Liu, J.; Woll, C. Surface-supported metal-organic framework thin films: fabrication methods, applications, and challenges. *Chemical Society Reviews* **2017,** 46 (19), 5730-5770 DOI: 10.1039/C7CS00315C.

8. Ahrenholtz, S. R.; Epley, C. C.; Morris, A. J. Solvothermal Preparation of an Electrocatalytic Metalloporphyrin MOF Thin Film and its Redox Hopping Charge-Transfer Mechanism. *Journal of the American Chemical Society* **2014,** 136 (6), 2464-2472 DOI: 10.1021/ja410684q.

9. DeBlase, C. R.; Silberstein, K. E.; Truong, T.-T.; Abruña, H. D.; Dichtel, W. R. β-Ketoenamine-Linked Covalent Organic Frameworks Capable of Pseudocapacitive Energy Storage. *Journal of the American Chemical Society* **2013,** 135 (45), 16821-16824 DOI: 10.1021/ja409421d.

10. Chandra, S.; Roy Chowdhury, D.; Addicoat, M.; Heine, T.; Paul, A.; Banerjee, R. Molecular Level Control of the Capacitance of Two-Dimensional Covalent Organic Frameworks: Role of Hydrogen Bonding in Energy Storage Materials. *Chemistry of Materials* **2017,** 29 (5), 2074-2080 DOI: 10.1021/acs.chemmater.6b04178.

11. Mulzer, C. R.; Shen, L.; Bisbey, R. P.; McKone, J. R.; Zhang, N.; Abruña, H. D.; Dichtel, W. R. Superior Charge Storage and Power Density of a Conducting Polymer-Modified Covalent Organic Framework. *ACS Central Science* **2016,** 2 (9), 667-673 DOI: 10.1021/acscentsci.6b00220.

12. Cabellero, A. G.; Croft, A. K.; Nalli, S. M. Remote aromatic stabilization in radical reactions. *Tetrahedron Letters* **2008,** 49 (22), 3613-3615 DOI: http://dx.doi.org/10.1016/j.tetlet.2008.04.009.

13. Arient, J.; Podstata, J. Nitration and oxidation of anthraquinone dimethyl derivatives. *Collect. Czech. Chem. Commun.* **1974,** 39 (11), 3117-3123.

14. Garay, R. O.; Naarmann, H.; Muellen, K. Synthesis and characterization of poly(1,4-anthrylenevinylene). *Macromolecules* **1994,** 27 (7), 1922-1927 DOI: 10.1021/ma00085a040.

15. Shearer, G. C.; Chavan, S.; Bordiga, S.; Svelle, S.; Olsbye, U.; Lillerud, K. P. Defect Engineering: Tuning the Porosity and Composition of the Metal–Organic Framework UiO-66 via Modulated Synthesis. *Chemistry of Materials* **2016,** 28 (11), 3749-3761 DOI: 10.1021/acs.chemmater.6b00602.

16. Cliffe, M. J.; Wan, W.; Zou, X.; Chater, P. A.; Kleppe, A. K.; Tucker, M. G.; Wilhelm, H.; Funnell, N. P.; Coudert, F. X.; Goodwin, A. L. Correlated defect nanoregions in a metal-organic framework. *Nat Commun* **2014,** 5, 4176 DOI: 10.1038/ncomms5176.

17. Li, W. H.; Ding, K.; Tian, H. R.; Yao, M. S.; Nath, B.; Deng, W. H.; Wang, Y.; Xu, G. Conductive Metal–Organic Framework Nanowire Array Electrodes for High-Performance Solid-State Supercapacitors. *Advanced Functional Materials* **2017,** 27 (27), 1702067 DOI: doi:10.1002/adfm.201702067.

18. Gholipour-Ranjbar, H.; Soleimani, M.; Naderi, H. R. Application of Ni/Co-based metal-organic frameworks (MOFs) as an advanced electrode material for supercapacitors. *New Journal of Chemistry* **2016,** 40 (11), 9187-9193 DOI: 10.1039/C6NJ01449F.

19. Lee, D. Y.; Shinde, D. V.; Kim, E.-K.; Lee, W.; Oh, I.-W.; Shrestha, N. K.; Lee, J. K.; Han, S.-H. Supercapacitive property of metal–organic-frameworks with different pore dimensions and morphology. *Microporous and Mesoporous Materials* **2013,** 171, 53-57 DOI: http://dx.doi.org/10.1016/j.micromeso.2012.12.039.

20. Tan, Y.; Zhang, W.; Gao, Y.; Wu, J.; Tang, B. Facile synthesis and supercapacitive properties of Zr-metal organic frameworks (UiO-66). *RSC Advances* **2015,** 5 (23), 17601-17605 DOI: 10.1039/C4RA11896K.

4. Elucidation of the Relative Contributions of Electronic and Ionic Diffusion from the Solid-State Voltammetry of Metallocene-doped Metal-Organic Frameworks Thin Films

Paula J. Celis-Salazar, Clark A. Cucinell, Spencer R. Ahrenholtz, Meng Cai, Charity C. Epley, Pavel M. Usov, Amanda J. Morris*

4.1 ABSTRACT

The chronoamperometric response (*I* vs. *t*) of three metallocene-doped metal-organic frameworks (MOFs) thin films (M-NU-1000, M= Fe, Ru, Os) in two different electrolytes ($TBAPF_6$ and TBATFAB) was utilized to elucidate the diffusion coefficients of electrons and ions (D_e and D_i, respectively) through the structure in response to an oxidizing applied bias. The application of a theoretical model for solid state-voltammetry to the experimental data revealed that the diffusion of ions is the rate-determining step at the three different time stages of the electrochemical transformation: an initial stage characterized by the rapid electron diffusion along the crystal-solution boundary (Stage A), a maximum exhaustive conversion of all the redox centers of such crystal-electrolyte interface (Stage B), and a final period of the conversion dominated only by the diffusion of ions from the surface of the crystal into the bulk (Stage C). Remarkably, the electron diffusion (D_e) increased in the order of Fe < Ru < Os using PF_6^{1-} as the counter anion in all the stages of the voltammogram, demonstrating the strategy to modulate the rate of electron transport through the incorporation of rapidly self-exchanging molecular moieties into the MOF structure. The D_e values obtained with larger $TFAB^{1-}$ counter anion were generally in agreement with the previous trend, but were on average lower than those obtained with PF_6^{1-}. Similarly, the ionic diffusion coefficient (D_i) was higher for PF_6^{1-} than for $TFAB^{1-}$ in the first two stages,

confirming that smaller ions move more rapidly through the MOF pores. These structure-function relationships provide a foundation for the future design, control, and optimization of electronic and ionic transport properties in MOF thin films.

4.2 INTRODUCTION

Metal-Organic Frameworks (MOFs) are prominent materials with considerable promise in many fields such as electrocatalysis, electronics and batteries.[1, 2] These hybrid arrays of inorganic nodes connected by organic-based ligands to form multidimensional structures have arisen as potential candidates to satisfy the current demands for cleaner energy and its environmentally sustainable storage.[3, 4] Recently, the fabrication of MOF thin films on conductive substrates, have facilitated their electrochemical characterization, and improved the utility of these systems in a wider variety of applications.[3]

Although originally most MOFs were considered electrical insulators, several examples of MOFs capable of efficient charge transport has been reported in the recent years.[5-7] Careful selection of ligands and nodes with appropriate electronic properties in the MOF synthesis, could lead to the extended structures containing charge transport pathways.[6, 7] Similarly, post-synthetic modifications (PSM) of existing MOFs have shown to be an effective strategy for incorporation of electroactive moieties.[8, 9] In particular, the use of coordinatively unsaturated metal clusters has been extensively employed to append the redox-active species inside the frameworks.[8, 10]

While these synthetic approaches have contributed to the development of an extensive variety of conductive MOFs, detailed studies on the mechanism of electron transport in these materials are still lacking. In principle, the charge propagation in frameworks can be facilitated by three different mechanisms: 1) ligand-node orbital energy overlap,[11] 2) π-stacking interactions between planar linkers,[12] and 3) redox hopping between the neighboring centers.[13] Indeed, the

latter mechanism was demonstrated experimentally by quantifying the apparent diffusion coefficient (D_{app}) in Co-based MOF thin films, suggesting that charge conduction occurs through discrete ambipolar redox-hopping steps.[13]

Specifically, for such mechanism to take place in a MOF, the electrochemical charge transport should depend on the rate of electron diffusion (D_e) from one redox center to another along the framework backbone, and the rate of ionic diffusion (D_i) through the MOF pores to maintain the electroneutrality.[13] The electron diffusion coefficient is related to the homogeneous self-exchange rate of the redox centers, whereas the ionic diffusion is primarily dependent on the ion size, MOF pore size, and the ion pairing ability. Despite the importance of these diffusion terms for understanding the overall charge transport properties in MOFs, there are no detailed reports examining their relative contributions towards this process. This information would be vital for establishing structure-function relationships in the design of these materials. Nevertheless, a theoretical model capable of individually quantifying these diffusional components has been developed in the past, for idealized microcrystals immobilized on the surface of an electrode.[14]

In order to apply this theoretical model to the solid-state voltammetry of MOF thin films, a series of materials with systematic parameter variation was devised. There are several important considerations: (1) First, the films should be constructed from a robust and chemically stable MOF with open metal sites, providing the possibility for a post-synthetic functionalization. For instance, the NU-1000 exhibits a high degree of stability, and has been previously functionalized with ferrocene molecules.[10, 15] (2) Additionally, the redox active centers inside the framework must be systematically varied through the use of isostructural guests with different self-exchange rates. For example, metallocenes behave as ideal redox couples, undergoing reversible one-electron oxidation reactions from M^{2+} to M^{3+}.[16, 17] Moreover, ferrocene, ruthenocene, and osmocene have

self-exchange rates differing by orders of magnitude,[18, 19] which is important to effectively probe the electronic diffusion. (3) Lastly, ionic diffusion should be interrogated by utilizing counter anions with substantially different sizes. For this role, non-coordinating anions such as PF_6 and TFAB,[20] combined with low donor solvents, such as dichloromethane, should facilitate the unimpeded ion mobility during the electrochemical analysis.[16]

Herein, we report the synthesis of metallocene-doped M-NU-1000 (M = Fe, Ru, Os) thin films on conductive fluorine-doped tin oxide (FTO) support. A series of chronoamperometry experiments in PF_6^{1-} and $TFAB^{1-}$ based electrolytes was performed with the goal of unravelling the individual contributions of electronic and ionic diffusion (D_e and D_i) in MOF thin films. We separated these contributions by applying a solid-state voltammetric model to the experimental data identifying three key stages in the process of electrochemical transformation. To the best of our knowledge, this investigation is the first attempt to directly quantify the main contributing factors to the redox-hopping process in MOFs.

4.3 EXPERIMENTAL SECTION

4.3.1 Synthesis of Ferrocene Carboxylic Acid (Fe-COOH)

The synthesis of **Fe-COOH** was achieved in two steps by following a procedure described in the literature (**Scheme S4.1**).[21] Ferrocene (1.86 g, 0.01 mol), 2-chlorobenzoyl chloride (1.3 mL, 0.01 mol) and 20 mL of dry dichloromethane were placed in a two-necked round bottom flask under positive flow of nitrogen and continuous stirring at 0 °C (ice bath). Anhydrous aluminum chloride (1.4 g, 0.01 mol) was added to the reaction mixture in small portions. As the reaction proceeded, the appearance of a blue color was observed. Once the addition was finished the mixture was stirred at 0 °C for 30 min, and at room temperature for 2 h. Subsequently, the mixture was cooled in ice and 100 mL of water were added to the flask. The two-phase mixture was stirred

vigorously for 30 min, and successively extracted with DCM. The DCM phase was reduced under vacuum and dried under air, to afford a red viscous slurry of 2-cholorobenzoyl ferrocene that was used in the next step without further purification. Potassium *tert*-butoxide (4.6 g, 0.04 mol) and 50.0 mL of tetrahydrofuran (THF) were added to the flask containing the 2-cholorobenzoyl ferrocene slurry with continuous stirring before it was placed under nitrogen flow, and equipped with a reflux condenser. Water (0.2 mL, 0.01 mol) was added to the mixture, and the reaction was refluxed for 1 h, undergoing a color change from yellow to tan. Once the reaction was cooled, 100 mL of water were added to the mixture and several extractions with diethyl ether were performed. The aqueous phase was isolated and acidified with concentrated hydrochloric acid (37 % HCl). The resultant yellow precipitate was filtered under vacuum and washed with water. The solid was dried overnight, affording pure **Fe-COOH** with 81% yield.[21] ^{1}H NMR (400 MHz, d_6-DMSO): δ 4.69 (s, 2H), 4.43 (s, 2H), 4.21 (s, 5H).

4.3.2 Synthesis of Ruthenocene Carboxylic Acid (Ru-COOH)

The synthesis of **Ru-COOH** was achieved in two steps by adapting the procedure reported for **Fe-COOH** (**Scheme S4.1**).[21] Ruthenocene (0.56 g, 2.4 mmol), 2-chlorobenzoyl chloride (0.30 mL, 2.4 mmol) and 20 mL of dry dichloromethane (DCM) were placed in a two-necked round bottom flask under positive flow of nitrogen and continuous stirring at 0 °C (ice bath). Anhydrous aluminum chloride (0.32 g, 2.4 mmol) was added to the reaction mixture in small portions. As the reaction proceeded, the color of the mixture changed from yellow to orange. Once the addition was finished the mixture was stirred at 0 °C for 30 min, and at room temperature for 2 h. Subsequently, the mixture was cooled in ice and 100 mL of water were added to the flask. The two-phase mixture was stirred vigorously overnight, and successively extracted with DCM. The DCM phase was reduced under vacuum and dried under air, to afford a yellow slurry of 2-

cholorobenzoyl ruthenocene that was used in the next step without further purification. Potassium *tert*-butoxide (1.1 g, 0.01 mol) and 25.0 mL of tetrahydrofuran (THF) were added to the flask containing the 2-cholorobenzoyl ruthenocene slurry with continuous stirring before the flask was placed under nitrogen flow, and equipped with a reflux condenser. Water (50 μL, 2.5 mmol) was added to the mixture, and the reaction was refluxed for 4 h, appearing beige in color. Once the reaction was cooled, 100 mL of water were added to the mixture, and several extractions with diethyl ether were performed. The aqueous phase was isolated and acidified with concentrated hydrochloric acid (37 % HCl). The pale yellow precipitate was filtered under vacuum and washed with water. The solid was dried overnight, affording pure **Ru-COOH** with 52% yield. ^{1}H NMR (400 MHz, d_6-DMSO): δ 5.01 (t, J = 1.9 Hz, 2H), 4.74 (t, J = 1.9 Hz, 2H), 4.60 (s, 5H).

4.3.3 Synthesis of Osmocene Carboxylic Acid (Os-COOH)

The synthesis of **Os-COOH** was achieved in two steps by adapting the procedure reported for **Fe-COOH** (**Scheme S4.1**).[21] Osmocene (0.52 g, 1.6 mmol), 2-chlorobenzoyl chloride (0.2 mL, 1.6 mmol) and 15 mL of dry dichloromethane (DCM) were placed in a two-necked round bottom flask under positive flow of nitrogen and continuous stirring at 0 °C (ice bath). Anhydrous aluminum chloride (0.23 g, 1.6 mmol) was added to the reaction mixture in small portions. As the reaction proceeded, the color of the mixture changed from white to yellow. Once the addition was finished the mixture was stirred at 0 °C for 30 min, and at room temperature for 2 h. Subsequently, the mixture was cooled in ice and 70 mL of water were added to the flask. The two-phase mixture was stirred vigorously overnight, and successively extracted with DCM. The aqueous phase was reduced under vacuum and dried under air, to afford a yellow slurry of 2-cholorobenzoyl osmocene that was used in the next step without further purification. Potassium *tert*-butoxide (0.74 g, 6.7 mol) and 25.0 mL of tetrahydrofuran (THF) were added to the flask containing the 2-

cholorobenzoyl osmocene slurry with continuous stirring before the flask was placed under nitrogen flow, and equipped with a reflux condenser. Water (34 μL, 2.5 mmol) was added to the mixture, and the reaction was refluxed for 4 h. Once the reaction was cooled, 100 mL of water were added to the mixture, and several extractions with diethyl ether were performed. The aqueous phase was isolated and acidified with concentrated hydrochloric acid (37 % HCl). The beige precipitate was filtered under vacuum and washed with water. The solid was dried overnight, affording **Os-COOH** with 50% yield. ^{1}H NMR (400 MHz, d_6-DMSO): δ 5.10 (m, 2H), 5.02 (m, 2H), 4.92 (s, 5H).

4.3.4 Synthesis of 1,3,6,8-tetrakis(p-benzoic acid)pyrene (TBAPy) ligand

The synthesis was achieved in two steps by following the previously reported procedure.[22] First, a stirred solution of 4-(methoxycarbonyl)phenyl boronic acid (5 g, 32.9 mmol), 1,3,6,8-tetrabromopyrene (2.85 g, 5.5 mmol), palladium tetrakis (triphenylphosphine) (0.1 g, 0.09 mmol), and potassium carbonate (6 g, 44 mmol) in dry dioxane (50 mL) was heated at 85 °C for 72 h under nitrogen flow. Subsequently, the mixture was poured into a solution containing concentrated hydrochloric acid (37 % HCl) and ice (w/w 1:3). Multiple extractions were performed using chloroform to purify the organic layer which was dried over magnesium sulfate. The solvent was removed under reduced pressure and the resulting solid of 1,3,6,8-tetrakis(4-methoxycarbonyl)phenyl pyrene was dried under vacuum and used in the next step without further purification. The compound 1,3,6,8-tetrakis(4-methoxycarbonyl)phenyl pyrene was dissolved in 100.0 mL of a mixture of THF-Dioxane-Water (5:2:2), and 20 mL of a concentrated NaOH solution were added to the suspension. The mixture was stirred and heated at 85 °C for 24 h. After removing the solvent, 50 mL of water were added to the solution, which was stirred for additional 2 h. The aqueous phase was acidified with concentrated hydrochloric acid (37 % HCl), and the

resulting yellow solid was filtered and dried under vacuum affording pure 1,3,6,8-tetrakis(p-benzoic acid)pyrene (TBAPy) with 84% yield.[22] ^{1}H NMR (400 MHz, d_6-DMSO): δ 8.21 (s, 4H), 8.16 (d, J = 8.4 Hz, 8H), 8.08 (s, 2H), 7.87 (d, J = 8.4 Hz, 8H)

4.3.5 Synthesis of NU-1000 MOF [$Zr_6(\mu_3{-}OH)_8(OH)_8(TBAPy)_2$]

The synthesis was carried out by following a procedure previously reported in the literature.[23] $ZrCl_4$ (70 mg, 0.3 mmol), and benzoic acid (2700 mg, 22 mmol) were dissolved in 8.0 mL of DMF and sonicated for 5 min. The mixture was placed in an oven at 80 °C for 1 h, and allowed to cool to room temperature. Then, the ligand, 1,3,6,8-tetrakis(p-benzoic acid)pyrene TBAPy (40 mg, 0.06 mmol) was added to the solution. The mixture was sonicated for 20 minutes before heating at 120 °C for 48 h. The NU-1000 MOF was obtained as a yellow powder, which was isolated by centrifugation, washed three times with fresh DMF and dried under vacuum.

4.3.6 Solvent Assisted Ligand Incorporation (SALI)

The SALI procedure was carried out by following an analogous procedure described in the literature.[10] The concentration of the metallocene carboxylic acids solutions was experimentally adjusted to obtain a constant Zr_6/ metallocene ratio of 1.

4.3.6.1 Fe-NU-1000

The NU-1000 (60 mg, 0.027 mmol) and 2.4 mL of a 0.1 M solution of Fe-COOH in DMF (0.24 mmol) were mixed in a 3 mL vial. The mixture was heated at 60 °C for 18 h, with occasional stirring. After cooling to room temperature, the powder was isolated by centrifugation. Subsequently, the resultant pink solid was washed and centrifuged three times with fresh DMF, and two times with acetone and diethyl ether. The Fe-NU-1000 sample was dried under vacuum at room temperature.[10]

4.3.6.2 Ru-NU-1000

The NU-1000 (60 mg, 0.027 mmol) and 2.4 mL of a 0.05 M solution of Ru-COOH in DMF (0.12 mmol) were mixed in a 3 mL vial. The mixture was heated at 60 °C for 18 h, with occasional stirring. After cooling to room temperature, the powder was isolated by centrifugation. Subsequently, the resultant pink solid was washed and centrifuged three times with fresh DMF, and two times with acetone and diethyl ether. The Ru-NU-1000 sample was dried under vacuum at room temperature.

4.3.6.3 Os-NU-1000

The NU-1000 (12 mg, 0.0054 mmol) and 2.4 mL of a 0.1 M solution of Os-COOH in DMF (0.24 mmol) were mixed in a 3 mL vial. The mixture was heated at 60 °C for 18 h, with occasional stirring. After cooling to room temperature, the powder was isolated by centrifugation. Subsequently, the resultant pink solid was washed and centrifuged three times with fresh DMF, and two times with acetone and diethyl ether. The Os-NU-1000 sample was dried under vacuum at room temperature.

4.3.7 Electrophoretic Deposition of MOF thin films

The electrophoretic deposition of the MOF films was achieved by using a previously reported procedure.[10] A suspension of the M-NU-1000 (M = Fe, Ru, Os; 14 mg) in 26 mL of toluene was stirred, while two identical FTO slides separated by 1 cm were placed in the solution. A constant DC voltage of 130 V was maintained for 3 hours.

4.4 RESULTS AND DISCUSSION

The monodentate metallocene-based ligands, namely ferrocene carboxylic acid **(Fe-COOH)**, ruthenocene carboxylic acid **(Ru-COOH)**, and osmocene carboxylic acid **(Os-COOH)**

were synthesized in two steps using a Friedel-Crafts acylation reaction of the parent metallocene, followed by a cleavage of the non-enolizable ketone to form the carboxylic acid (Scheme S4.1).[21] The ligand 1,3,6,8-tetrakis(p-benzoic acid)pyrene (TBAPy) was synthesized via a Suzuki reaction and a basic hydrolysis according to previously reported procedures.[22] The solvothermal reaction of TBAPy and $ZrCl_4$ in DMF, using benzoic acid as a modulator afforded NU-1000 MOF as a yellow powder.[23]

The incorporation of the metallocene ligands in the structure of the NU-1000 to obtain M-NU-1000 (M= Fe, Ru, Os) was achieved through a commonly employed solvent assisted ligand incorporation (SALI) procedure.[10] NMR analysis of the digested M-NU-1000 samples (Figure S4.1) revealed that the ratio of Zr_6 to metallocene was 1:1 in all the frameworks, suggesting the presence of one metallocene molecule per zirconium node (Figure 4.1A). It is important to keep this ratio constant across the series, to ensure that metallocene concentration inside NU-1000 and the distance between them remains unchanged during the electrochemical characterization. Additionally, powder X-ray diffraction (PXRD) patterns of **Fe-NU-1000**, **Ru-NU-1000**, and **Os-NU-1000** samples confirmed the expected NU-1000 structure, which remained consistent after the SALI procedure (Figure 4.1B). The deposition of these MOFs as thin films was achieved by electrophoretic deposition using conductive FTO slides as a support.[10] SEM analysis showed an average film thickness of 1 μm (Figure S4.2), and a hexagonal rod morphology of framework particles across the film surface, characteristic of NU-1000 microcrystals (Figure S4.3).

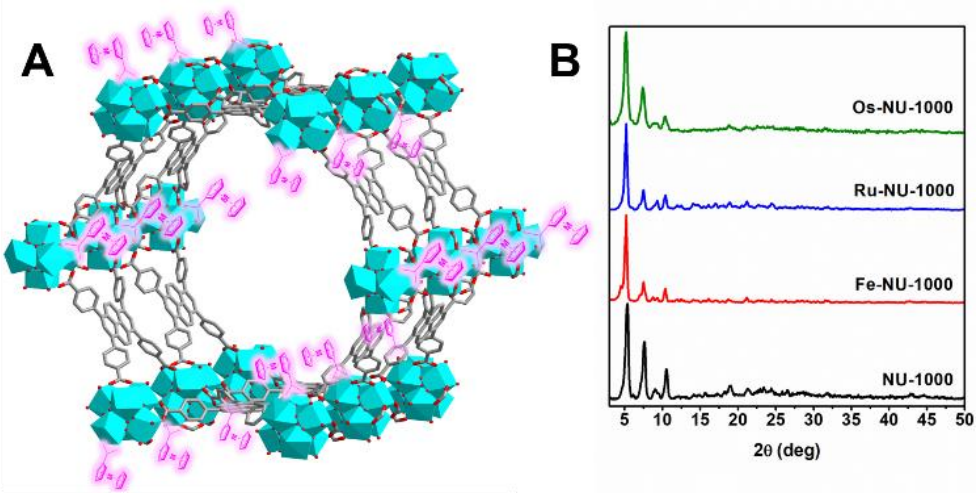

Figure 4.1. A) Schematic representation of M-NU-1000 (M = Fe, Ru, Os) displaying one metallocene per node loading. B) PXRD patterns of **Nu-1000** (Black)**, Fe-NU-1000** (Red), **Ru-NU-1000** (Blue), and **Os-NU-1000** (Green).

Cyclic voltammetry (CV) of the M-NU-1000 (M = Fe, Ru, Os) thin films was performed in a three-electrode assembly, using the film as the working electrode and either a $TBAPF_6$ or TBATFAB acetonitrile solution (0.1 M) as a supporting electrolyte (see SI for detailed electrochemical procedures). All the cyclic voltammograms of M-NU-1000 (M = Fe, Ru, Os) thin films showed a single reversible redox process, characteristic of the one-electron metallocene-centered oxidation process from M^{2+} to M^{3+} (M = Fe, Ru, Os) (Figure 4.2). The counter anion [A^-] in the electrolyte solution (PF_6^{1-} or $TFAB^{1-}$) acts as a charge compensator to maintain electroneutrality, according to the following redox reaction:

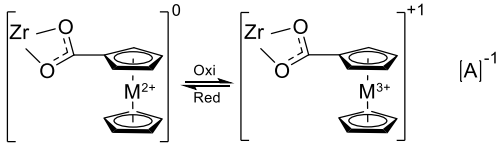

(4.1)

In principle, the rate of this redox reaction inside the MOF depends on both the rate of electron diffusion from one metallocene center to another (represented by the electron diffusion coefficient, D_e), and the rate of counter anion diffusion through the MOF pores to maintain the

charge balance (represented by the ionic diffusion coefficient, D_i). Specifically, D_e should be dependent to the homogeneous self-exchange rate (M^{2+} to M^{3+}) of the metallocene centers (Fe ≈ 10^6 $M^{-1}s^{-1}$, Ru ≈ 10^4 $M^{-1}s^{-1}$, Os ≈ 10^2 $M^{-1}s^{-1}$).[18, 19] D_i on the other hand, should be directly related to the anion size ($PF_6^{1-}{}_{vol}$ = 0.109 nm^3, $TFAB^{1-}{}_{vol}$= 0.405 nm^3).[20] The possibility of anion coordination can be neglected in this case, since both anions are relatively weekly interacting. CV analysis allowed the determination of the oxidation potentials for the M^{2+}/M^{3+} redox couple for each of the six metallocene-counter anion combinations (Figure 4.2). These values (*E*) were used in the subsequent potential-step experiments.

To obtain the diffusion coefficients, chronoamperometry experiments were carried out on the **Fe-NU-1000**, **Ru-NU-1000**, and **Os-NU-1000** thin films, which were held at a potential just below the redox peak for 20 min. After that, the potential was stepped above the oxidation process, as determined from CV data (Figure 4.2). A schematic representation of the applied time-dependent potential profile is shown in Figure 4.3A. The current passed through the film at the applied potential E_2 was monitored for 20 min, obtaining a current vs. time (*I* vs. *t*) plot (Figure 4.3B). It has been theoretically demonstrated that for solid state voltammetry of electrode-confined collection of microcrystals in contact with an electrolyte solution, this current-time response is governed by the electronic and ionic diffusion coefficients (D_e and D_i).[14] A three-dimensional theoretical model to quantify the relative contribution of both D_e and D_i was developed by Scholz et al.[14] who assumed that the electrochemical reaction starts at the electrolyte-crystal-electrode three-phase junction (Figure 4.3D).[14] From this boundary, a simultaneous injection or removal of electrons and the corresponding dislocation of ions to maintain electroneutrality takes place, as the reaction zone propagates into the crystal interior.[14] Electron diffusion is postulated to be perpendicular to the electrode surface, while the ionic diffusion is parallel (Figure 4.3D).[14] We

sought to apply this model to the current-time response obtained for the **Fe-NU-1000**, **Ru-NU-1000**, and **Os-NU-1000** thin films in two different electrolytes (Figure 4.4 A-F), for the purpose of elucidating the values of D_e and D_i.

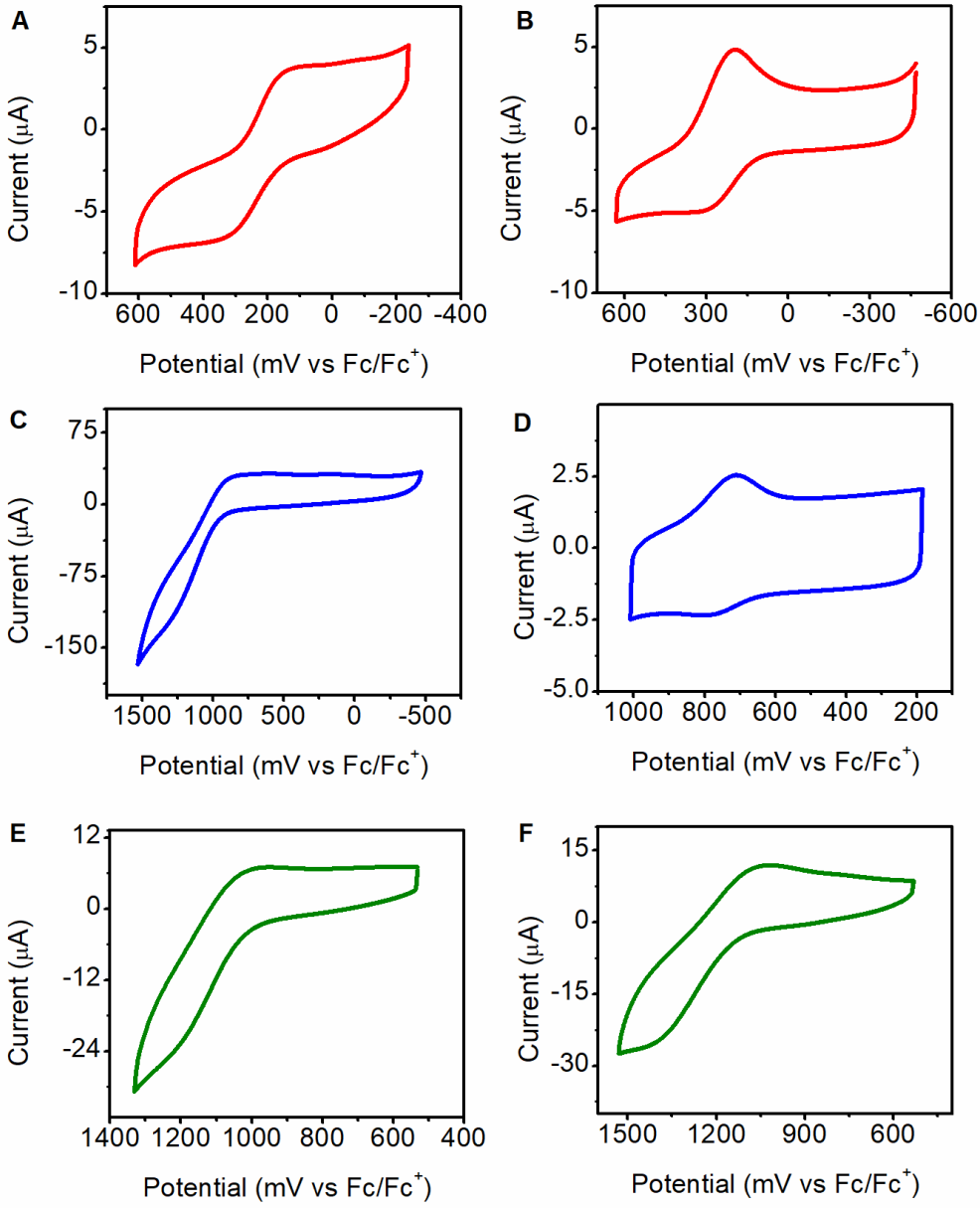

Figure 4.2. Cyclic voltammograms (100 mV s^{-1}) of the MOF films in 0.1 M supporting electrolyte in acetonitrile A) **Fe-NU-1000**, $TBAPF_6$, B) **Fe-NU-1000**, TBATFAB, C) **Ru-NU-1000**, $TBAPF_6$, D) **Ru-NU-1000**, TBATFAB, E) **Os-NU-1000**, $TBAPF_6$, F) **Os-NU-1000**, TBATFAB.

The model suggests the existence of three distinct reaction stages in the observed *I* vs. *t* curves, representing the extent of redox conversion. When plotting the chronoamperometric response as a $I\sqrt{t}$ vs.$\sqrt{t}$ plot, these three stages (denoted as A, B, and C) become evident (Figure 4.3C). During Stage A, both electron and ionic diffusion are unhindered, and the faster process leads the spread of the initial conversion either along the crystal-solution interface or along the crystal-electrode boundary.[14] Stage B, is the maximum of the $I\sqrt{t}$ vs.$\sqrt{t}$ curve (Figure 4.3C) and corresponds to the moment when all the redox centers across such interface are converted. From this instant, the further course of the reaction into the crystal bulk is controlled by the slowest process (Stage C), being the very end of these stage the most characteristic segment, where the conversion of the crystal is higher than 99% (Figure 4.3C).[14] The model derived separate current-time equations for each stage, as a function of several physical parameters, including the diffusion coefficients (D_e and D_i).[14] These equations were used to fit the experimental data at each stage, to obtain the physical values of D_e and D_i and their evolution as the electrochemical reaction progresses.

First, the $I\sqrt{t}$ vs.$\sqrt{t}$ curves for the **Fe-NU-1000**, **Ru-NU-1000**, and **Os-NU-1000** thin films in the two different electrolytes were constructed, as shown in Figure 4.4 G-L. For each of the six combinations of metallocene-counter anion couples, the chronoamperometry experiments were repeated four times on different films, in order to obtain the average D_e and D_i values and the correspondent statistical error (see SI for detailed electrochemical procedures and a step by step sample calculation of the applied model at the three different stages). Once the three stages (A, B, and C) where identified from the $I\sqrt{t}$ vs.$\sqrt{t}$ plots (Figure 4.4 G-L), the curve fitting of the experimental data to the appropriate current-time equation was carried out as follows:

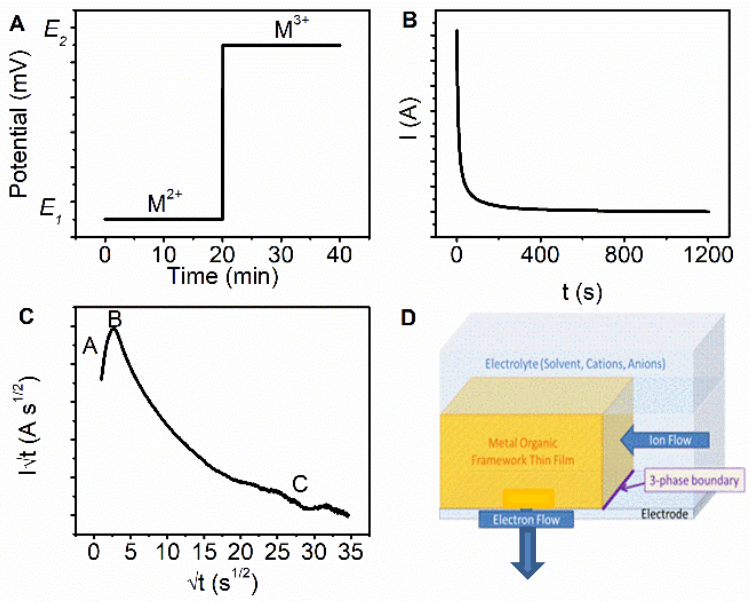

Figure 4.3. Schematic representation of A) Time-dependent potential function applied to the M-NU-1000 (M= Fe, Ru, Os) thin films. B) An example of current response observed in a M-NU-1000 (M= Fe, Ru, Os) thin film at an applied potential (E_2) as a function of time - (I vs. t) plot. C) The $I\sqrt{t}$ vs.$\sqrt{t}$ plot of chronoamperometric response, depicting the different time stages. D) An illustration of MOF microcrystals immobilized on an electrode surface, in contact with an electrolyte solution.

4.4.1 Stage A

This initial stage corresponds to the beginning of the electrochemical reaction (Figure 4.3C, and Figure 4.4 G-L). During this period, the model assumes that unhindered diffusion of both electrons and ions occurred through a quasi-semi-infinite space.[14] The resulting current-time function for Stage A is expressed as:[14]

$$I(t) = \frac{NF}{V_m}\left\{\frac{1}{1+\exp(-\varphi)}\right\}\left[u\left(\left(\frac{\Delta x_0\sqrt{D_e}+\Delta z_0\sqrt{D_i}}{2\sqrt{\pi t}}\right)+\sqrt{D_e D_i}\right)-4D_i\sqrt{2D_e t}\right] \quad \textbf{(4.2)}$$

where N is the number of MOF crystallites in the film, F is Faraday's constant, u is the length of the three-phase junction (perimeter of the electrode-crystal interface), V_m is the MOF molar volume, D_e is the electronic diffusion coefficient, D_i is the ionic diffusion coefficient, Δx_0 is the distance an ion travels in one hopping step, Δz_0 is the distance an electron travels in one hopping step, and

$$\varphi = \frac{F}{RT}(E_f - E) \quad \textbf{(4.3)}$$

where R is the gas constant, T is temperature, E is the applied potential, and E_f is the formal potential. All of the above parameters can be empirically obtained from the crystal structure of NU-1000, SEM images of the films, and the Zr_6/metallocene ratio calculated from NMR digestion studies (See SI).

The fitting of Eq. 4.2 to the current- time response (I vs. t) of all the M-NU-1000 (M = Fe, Ru, Os) thin films in both electrolytes is shown in Figure 4.4 A-F (blue traces). A generally good fit (R^2> 96%, see SI) was observed for all the films, evidencing a close agreement between the experimental data and the theoretical model. The diffusion coefficients calculated in Stage A are presented in Figure 4.5 and summarized in Table 4.1.

Theoretically, two different cases can occur during the initial Stage A, as the reaction zone spreads: **(1)** If the ionic diffusion is faster than the electronic diffusion ($D_e < D_i$), this period is characterized by the rapid migration of ions along the electrode-crystal interface, where the redox active centers along this boundary are quickly converted.[14] On the other hand, **(2)** if the electronic diffusion is faster than the ionic diffusion ($D_e > D_i$), the reaction zone rapidly spreads away from the electrode in a perpendicular direction, parallel to the electrolyte-crystal interface (the crystal surface). As a result, the redox centers along this boundary are the first to undergo the electrochemical transformation.[14]

It is evident from the model fit (Figure 4.5, Table 4.1) that the values of D_e (10^{-5} - 10^{-7}) are considerably higher than those of D_i (10^{-15} - 10^{-18}) across all the M-NU-1000 (M = Fe, Ru, Os) thin films regardless of the counter ion size. Therefore, the mechanism of the electron/ion transport in Stage A, follows the latter case ($D_e > D_i$) with rapid electron hopping along the crystal walls. Another important finding is the considerable variation in the D_e values for the M-NU-1000 (M =

Fe, Ru, Os) series in Stage A (Figure 4.5- Stage A). The magnitude of electronic diffusion followed the trend of the self-exchange rates of the metallocene centers. That is, D_e increased in the order **Fe-NU-1000** < **Ru-NU-1000** < **Os-NU-1000** using PF_6^{1-} as the counter anion. This result highlights the interdependence of electronic diffusion and the self-exchange rate of the redox centers, presenting the strategy to control the rate of electron transport in MOFs. A similar behavior was observed using $TFAB^{1-}$ as the counter anion, however the trend was weaker, the D_e values varied in the order of **Fe-NU-1000 ≈ Ru-NU-1000 < Os-NU-1000.**

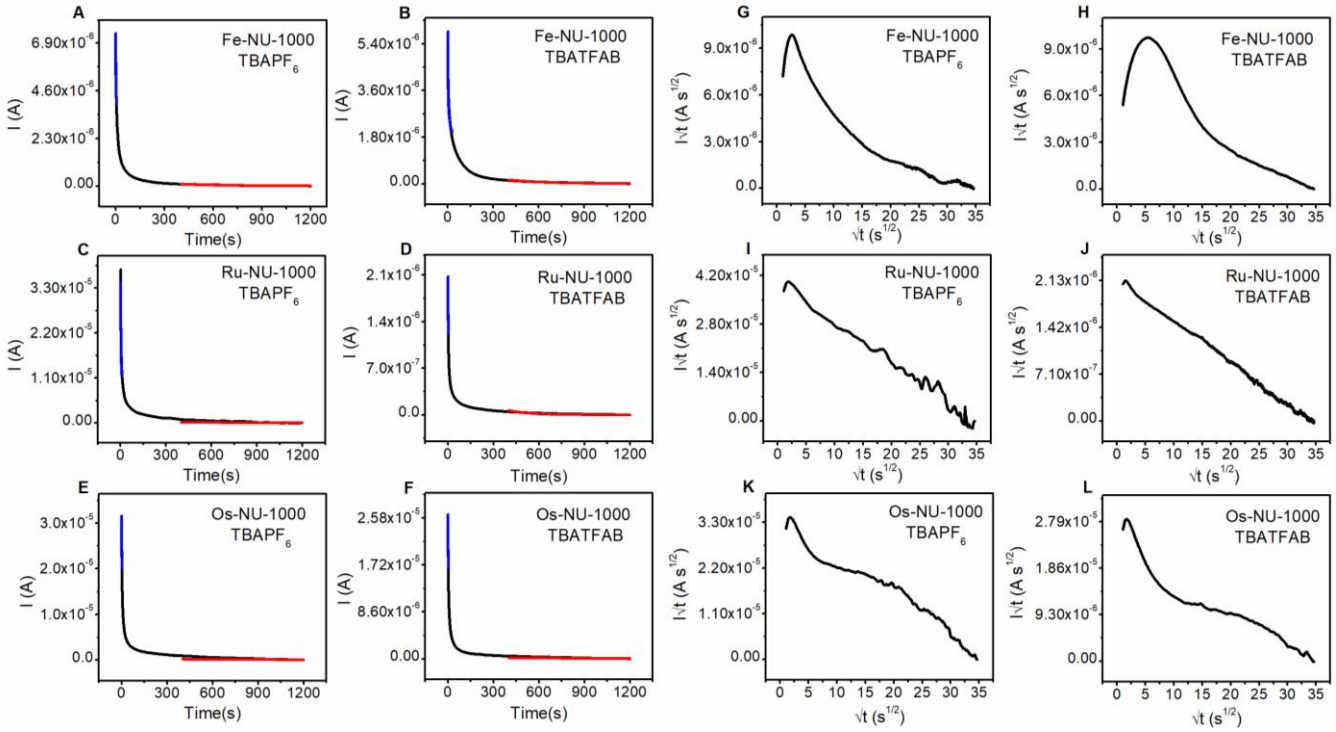

Figure 4.4. ***Left:*** The current - time response (*I* vs. *t*) at an applied potential *E*, measured in 0.1 M supporting electrolyte for the films of A) **Fe-NU-1000**, $TBAPF_6$, B) **Fe-NU-1000**, TBATFAB, C) **Ru-NU-1000**, $TBAPF_6$, D) **Ru-NU-1000**, TBATFAB, E) **Os-NU-1000**, $TBAPF_6$, F) **Os-NU-1000**, TBATFAB. *Black*: Experimental response, *Blue*: Model fitting **Stage A** Equation (2), *Red*: Model fitting **Stage C** Equation (4.6). ***Right:*** Chronoamperometric response expressed as a $I\sqrt{t}$ vs.$\sqrt{t}$ plot at an applied potential *E*, measured in 0.1 M supporting electrolyte for the films of G) **Fe-NU-1000**, $TBAPF_6$, H) **Fe-NU-1000**, TBATFAB, I) **Ru-NU-1000**, $TBAPF_6$, J) **Ru-NU-1000**, TBATFAB, K) **Os-NU-1000**, $TBAPF_6$, L) **Os-NU-1000**, TBATFAB.

Noteworthy, the electronic diffusion (D_e) was considerably faster in PF_6^{1-} based electrolyte than in $TFAB^{1-}$ for all the M-NU-1000 (M = Fe, Ru, Os) thin films (Figure 4.5- Stage A). This fact suggests that the smaller volume of PF_6^{1-} relative to $TFAB^{1-}$ facilitated the faster electron transport across the metallocene centers. Similarly, and perhaps unsurprisingly, the ionic diffusion (D_i) was faster for PF_6^{1-} compared to $TFAB^{1-}$, due to its smaller ionic radius (Figure 4.5- Stage A). In summary, the redox hopping in stage A is dominated by electron hopping along the crystal boundary.

4.4.2 Stage B

The moment when all the redox centers in the electrolyte-crystal interface are converted, corresponds to the maximum of the $I\sqrt{t}$ vs.$\sqrt{t}$ curve (Figure 4.3C, and Figure 4.4 G-L). At this point, Eq. 4.2 loses its validity as electrons reach a physical barrier (the crystal-solution interface), and diffusion is no longer assumed unhindered.[14] Therefore, the theoretical model developed by Scholz et al.[14] defined this maximum of the $I\sqrt{t}$ vs.$\sqrt{t}$ curves (Figure 4.3C), as a characteristic time t_{ref}, that follows the mathematical expression:

$$t_{ref} = \frac{H^2}{1.1\, D_e} \qquad \textbf{(4.4)}$$

where H is the thickness of the MOF particles (1 μm, according to SEM images, Figure S4.2).

As a result, the current detected at this time (I_{ref}) can be expressed as:[14]

$$I_{ref} = 0.72 \frac{NFu}{V_m} \sqrt{D_e D_i} \qquad \textbf{(4.5)}$$

The diffusion coefficients (D_e and D_i) in Stage B were calculated using Eq.4.4 and Eq.4.5 and are summarized in Figure 4.5 and Table 4.1. Since the process is limited by ion movement, the values of D_e (≈ 10^{-9} - 10^{-10}) were again found to be higher than those of D_i (≈ 10^{-11} - 10^{-14}) for all the metallocenes in both electrolytes. Importantly, the D_e values in Stage B are lower than those

obtained in Stage A, which is a consequence of electrons reaching the crystal-solution interface as a physical barrier. Also, the overall ionic diffusion (D_i) has increased across the series in Stage B compared to Stage A, demonstrating that ions were initially slower to move from the electrolyte to the crystal surface to satisfy the electroneutrality requirement in Stage A, but started to navigate faster on the MOF channels once inside the MOF particle (Stage B).

One of the key conclusions of this modelling was that the principal trends in diffusion coefficients observed for the M-NU-1000 (M = Fe, Ru, Os) thin films in Stage A remained largely unchanged in Stage B (Figure 4.5). In particular, the electronic diffusion (D_e) also varied as a function of the metallocene self-exchange rate. The D_e values in PF_6^{1-} based electrolyte, increased in the order **Fe-NU-1000** < **Ru-NU-1000** < **Os-NU-1000**. While using $TFAB^{1-}$ as the counter anion, the as the order was **Fe-NU-1000** < **Ru-NU-1000** ≈ **Os-NU-1000,** which could be attributed to the retardation of the electron diffusion of **Os-NU-1000** by the slower diffusion of $TFAB^{1-}$ inside the framework (Figure 4.5 - Stage B). Moreover, the use of PF_6^{1-} as the counter anion resulted in generally faster electronic diffusion relative to $TFAB^{1-}$, except for the **Ru-NU-1000** thin films (Figure 4.5 - Stage B). Consequently, the electron transport across the metallocene centers of the Fe and Os analogues appeared to be maximized in the presence of the smaller counter anion. As for the ionic diffusion (D_i), it is evident that the PF_6^{1-} anion has higher mobility than $TFAB^{1-}$ as they infiltrate inside the MOF particles (Figure 4.5 - Stage B).

Remarkably, the similarities in the diffusion coefficient trends (D_e and D_i) for the M-NU-1000 (M = Fe, Ru, Os) thin films at both Stage A and Stage B, suggest that the redox hopping rate can be modulated (and potentially maximized) through the incorporation of molecular moieties with rapid self-exchange rates into the MOF structure containing large channels, as well as employing electrolytes based on smaller counter ions.

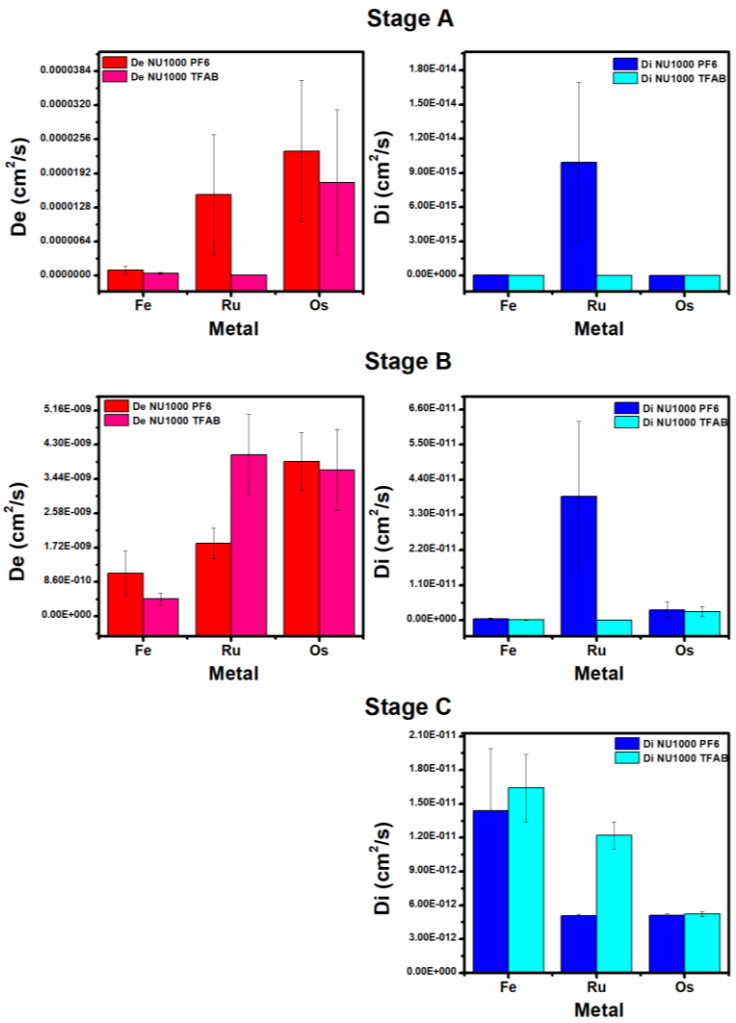

Figure 4.5. Summary of the diffusion coefficients for M-NU-1000 (M = Fe, Ru, Os) thin films in $PF_6^{1-}$and $TFAB^{1-}$ based electrolytes at the three reaction stages. **Stage A:** Electronic diffusion coefficient D_e (*Top left*), ionic diffusion coefficient D_i (*Top right*). **Stage B:** Electronic diffusion coefficient D_e (*Middle left*), ionic diffusion coefficient D_i (*Middle right*). **Stage C:** Ionic diffusion coefficient D_i (*Bottom right*).

4.4.3 Stage C

After the rapid exhaustion of the metallocene centers at the electrolyte-crystal interface (maximum of the $I\sqrt{t}$ vs.$\sqrt{t}$ curve, or Stage B), the further course of the reaction into the crystal bulk is controlled by the ability of ions to propagate into the MOF interior and provide the charge balance (Stage C). More specifically, during this final stage the electrochemical reaction front

spreads deeper into the crystallites, where the ion migration trough the framework channels becomes extremely important (Figure 4.3C and Figure 4.4 G-L).

During this stage, the ions diffuse into the bulk of the MOF particles trough a large electrolyte-crystal interface, as compared to the thickness of the film. Therefore, the last period of the electrochemical conversion is determined by the dimensions of the MOF crystallites. As a consequence, the chronoamperometric curves for Stage C can be modeled exclusively in terms of the ionic diffusion coefficients (D_i), and the crystal dimensions:[14]

$$I(t) = \frac{NFLHD_i}{V_m B}\left\{\frac{1}{(1+\exp(-\varphi))}\right\} exp\left[\frac{-\pi D_i t}{B^2}\right] \quad \textbf{(4.6)}$$

where L and B are the average length and the average width of the MOF particles, respectively (according to SEM images, Figure S4.3). It is important to note that Eq. 4.6 has been developed for the very last segment of Stage C, where the total conversion of the crystal is higher than 99% (Figure 4.3C).[14]

The fitting of Eq. 4.6 to the current- time response (I vs. t) of all the M-NU-1000 (M = Fe, Ru, Os) thin films in both electrolytes is shown in Figures 4.4 A-F (red traces). A generally good fit (R^2 > 90%, see SI) was achieved for the majority of the films, evidencing a good agreement between the experimental data and the theoretical model. The diffusion coefficients obtained in Stage C are presented in Figure 4.5 and summarized in Table 4.1.

The values of D_i in this final stage are higher than those obtained in both Stage A and Stage B, for all the M-NU-1000 (M = Fe, Ru, Os) thin films, demonstrating again that once the ions have satisfied the electroneutrality in the crystal-solution interface, ionic diffusion is enhanced inside the crystallite particle through the MOF channels (Figure 4.5- Stage C). Since the last segment of Stage C represents the moment of 99% of conversion, the values obtained for D_i describe an instant where the diffusion conditions are similar to a typical twin-electrode thin film cell, and the

electroneutrality requirement is almost totally satisfied across the particle. Only the D_i of the **Ru-NU-1000** thin film in the presence of PF_6^{1-} appears to diminish from Stage B to Stage C. However, this particular combination exhibited abnormally high ionic diffusion in the earlier stages.

Table 4.1. Summary of the electronic (D_e) and ionic (D_i) diffusion coefficients for M-NU-1000 (M = Fe, Ru, Os) thin films in PF_6^{1-} and $TFAB^{1-}$ based electrolytes

Stage A

	D_e ($cm^2\ s^{-1}$)		D_i ($cm^2\ s^{-1}$)	
	PF_6^{1-}	**$TFAB^{1-}$**	**PF_6^{1-}**	**$TFAB^{1-}$**
Fe	$(9.99 \pm 7.75) \times 10^{-7}$	$(3.94 \pm 1.64) \times 10^{-7}$	$(4.01 \pm 1.88) \times 10^{-17}$	$(1.47 \pm 1.23) \times 10^{-17}$
Ru	$(1.52 \pm 1.13) \times 10^{-5}$	$(8.22 \pm 2.33) \times 10^{-8}$	$(9.92 \pm 7.03) \times 10^{-15}$	$(1.88 \pm 2.76) \times 10^{-18}$
Os	$(2.34 \pm 1.33) \times 10^{-5}$	$(1.75 \pm 1.37) \times 10^{-5}$	$(8.40 \pm 4.62) \times 10^{-18}$	$(1.00 \pm 1.01) \times 10^{-17}$

Stage B

	D_e ($cm^2\ s^{-1}$)		D_i ($cm^2\ s^{-1}$)	
	PF_6^{1-}	**$TFAB^{1-}$**	**PF_6^{1-}**	**$TFAB^{1-}$**
Fe	$(1.08 \pm 0.56) \times 10^{-9}$	$(4.34 \pm 1.50) \times 10^{-10}$	$(3.72 \pm 3.23) \times 10^{-13}$	$(1.42 \pm 1.11) \times 10^{-13}$
Ru	$(1.83 \pm 0.38) \times 10^{-9}$	$(4.05 \pm 1.02) \times 10^{-9}$	$(3.88 \pm 2.36) \times 10^{-11}$	$(1.32 \pm 0.21) \times 10^{-14}$
Os	$(3.88 \pm 0.73) \times 10^{-9}$	$(3.67 \pm 1.01) \times 10^{-9}$	$(3.21 \pm 2.54) \times 10^{-12}$	$(2.72 \pm 1.59) \times 10^{-12}$

Stage C

	D_i ($cm^2\ s^{-1}$)	
	PF_6^{1-}	**$TFAB^{1-}$**
Fe	$(1.44 \pm 0.55) \times 10^{-11}$	$(1.64 \pm 0.30) \times 10^{-11}$
Ru	$(5.08 \pm 0.12) \times 10^{-12}$	$(1.22 \pm 0.12) \times 10^{-11}$
Os	$(5.12 \pm 0.13) \times 10^{-12}$	$(5.23 \pm 0.24) \times 10^{-12}$

Interestingly, ionic diffusion correlated with the self-exchange rates of the metallocene centers, despite occurring on a much slower timescale. The values decreased in the order **Fe-NU-**

1000 > **Ru-NU-1000** > **Os-NU-1000** for both electrolytes (Figure 4.5 - Stage C). Since it was demonstrated in Stages A and B, that the electronic diffusion increased in the order **Fe-NU-1000** < **Ru-NU-1000** < **Os-NU-1000**, this result suggests that the ionic diffusion inside the MOF channels is enhanced by the urge of satisfying the electroneutrality requirement in the redox nodes showing the slower electronic diffusion. However, given the difference of orders of magnitude between the electronic and ionic diffusion coefficients obtained in this study, and the fact that equations developed for Stage C corresponds to the moment of 99% of conversion, this correlation may be insignificant.[14]

4.5 CONCLUSION

In summary, the systematic variation of metallocene redox center and counter anions in a series of chronoamperometry experiments allowed the elucidation of the relative contribution of electronic and ionic diffusion in metallocene-doped NU-MOF thin films. Outstandingly, the trends observed in the diffusion coefficients (D_e and D_i) of these systems obtained in PF_6^{1-} and $TFAB^{1-}$ based electrolytes at the different stages of the electrochemical reaction, demonstrated that the redox hopping rates inside frameworks can be controlled through the modifications of the self-exchange rates of redox centers, the use of large MOF channels, and the utilization of smaller counter anions. The successful application of a solid-state voltammetric model to the experimental chronoamperometry data of MOF thin films, is a significant advancement to the understanding of electron and ion mobility in the context of electrochemical experiments, and can be used to guide further research into other redox-active MOFs.

4.6 SUPPORTING INFORMATION

4.6.1 Materials and Instrumentation

4.6.1.1 Materials

All reagents and solvents were purchased from commercial sources and used without further purification.

4.6.1.2 Nuclear Magnetic Resonance (NMR)

^{1}H NMR spectra were acquired on a Agilent U4-DD2 spectrometer operating at 400 MHz. Samples were analyzed as solutions in DMSO-d_6 (ca. 10 mg mL^{-1}) at 25 °C in standard 5 mm o.d. tubes.

4.6.1.3 Powder X-Ray Diffraction (PXRD)

PXRD measurements were carried out on a Rigaku Miniflex equipped with a Cu(Kα) radiation source (λ=1.5418 Å). The scanning rate was 1°/min using a 2θ range of 3- 50° on continuous mode. The samples were mounted onto reflective disks with a Si (510) surface.

4.6.1.4 Scanning Electron Microscopy (SEM)

A LEO (Zeiss) 1550 high-performance Schottky field-emission scanning electron microscope equipped with an in-lens detector was used at 5.0 kV to obtain high-resolution images of the MOFs.

4.6.1.5 Electrochemistry

All electrochemical experiments were performed in a BASi EC Epsilon potentiostat using a standard three-electrode configuration: The M-NU-1000 (M=Fe, Ru, Os) thin films as a working electrode, a high surface area Pt mesh as the counter electrode, and a non-aqueous Ag/Ag^+ reference electrode (0.1 M $TBAPF_6$). Ferrocene was used to calibrate the reference electrode with all the potentials reported vs Fc/Fc^+.

4.6.2 Synthetic Procedures

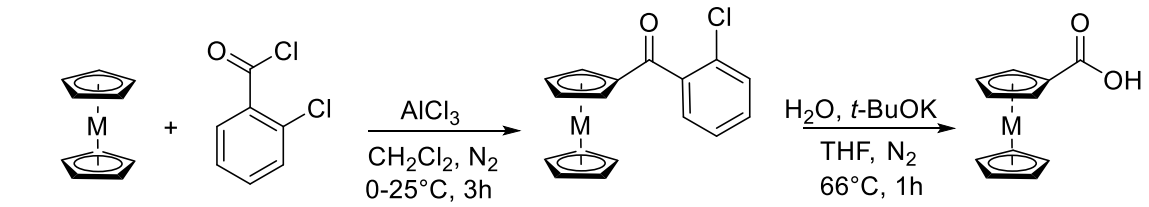

M= Fe, Ru, Os

Scheme S4.1: Synthesis of metallocene carboxylic acid ligands **Fe-COOH**, **Ru-COOH**, and **Os-COOH**

4.6.3 Determination of Metallocene to Node ratio of M-NU-1000 MOFs (M=Fe, Ru, and Os) from NMR

The experimental determination of the metallocene /Zr_6 ratio was achieved by following a similar procedure described in the literature.[10] A sample of 1.0 mg of the **M-NU-1000 MOFs (M=Fe, Ru, and Os)** powder was placed in a NMR tube, where 1 drop of H_2SO_4 and 500 μL of DMSO-d_6 were added. A quantitative ^{1}H NMR was taken, showing the signals of both the TBAPy ligand and the correspondent metallocene **M-COOH (M=Fe, Ru, and Os)** (Figure S4.1). The molar ratio of metallocene to TBAPy ligand was calculated as follows:

$$\frac{Metallocene}{\text{TBAPy}} = \frac{Integration\ Metallocene}{Equivalent\ ^1H\ nuclei\ Metallocene} * \frac{Equivalent\ ^1H\ nuclei\ \text{TBAPy}}{Integration\ \text{TBAPy}}$$

where $\boldsymbol{Equivalent\ ^1H\ nuclei}$ is the number of equivalent ^{1}H nuclei contributing to the ^{1}H NMR signal per molecule. For example, the three ^{1}H signals of the **M-COOH (M=Fe, Ru, and Os)** metallocene ligand originate from its three groups of equivalent protons, where each signal represents the integration of 2H, 2H, and 5H respectively (Figure S4.1). Therefore $\boldsymbol{Equivalent\ ^1H\ nuclei\ Metallocene = 9}$.Similarly, $\boldsymbol{Equivalent\ ^1H\ nuclei}$ **TBAPy** = **22.** Replacing the numerical $\boldsymbol{Integration}$ value of the signals for TBAPy and the **M-COOH**

(M=Fe, Ru, and Os) ligands obtained from the ^{1}H NMR spectra (Figure S4.1), the molar ratios were find to be:

$$\frac{\mathbf{Fe-COOH}}{\text{TBAPy}} = \frac{5.21}{9} * \frac{22}{21.52} = 0.59$$

$$\frac{\mathbf{Ru-COOH}}{\text{TBAPy}} = \frac{4.11}{9} * \frac{22}{20.69} = 0.48$$

$$\frac{\mathbf{Os-COOH}}{\text{TBAPy}} = \frac{9.65}{9} * \frac{22}{42.58} = 0.55$$

According to the formula of **NU-1000 MOF** $[Zr_6(\mu_3\text{–}OH)_8(OH)_8(TBAPy)_2]$, there are 2 TBAPy ligands per Zr_6. As a result, the obtained metallocene /Zr_6 ratios were:

$$\frac{\mathbf{Fe-COOH}}{Zr_6} = 0.59 * 2 = 1.18$$

$$\frac{\mathbf{Ru-COOH}}{Zr_6} = 0.48 * 2 = 0.96$$

$$\frac{\mathbf{Os-COOH}}{Zr_6} = 0.55 * 2 = 1.10$$

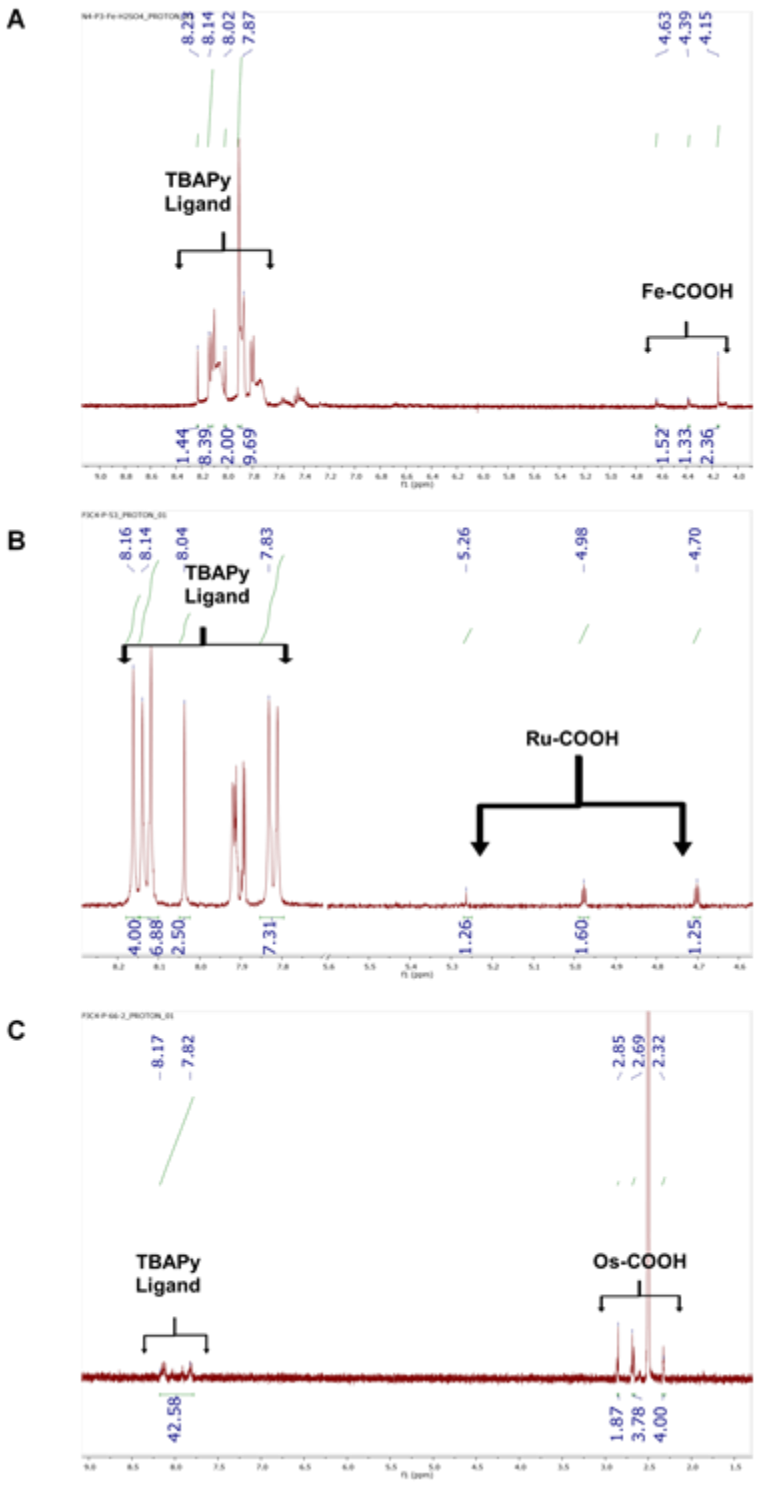

Figure S4.1: ^{1}H NMR spectra obtained for digested A) **Fe-NU-1000**, B) **Ru-NU-1000**, and B) **Os-NU-1000**

4.6.4 Scanning Electron Microscopy (SEM) Images

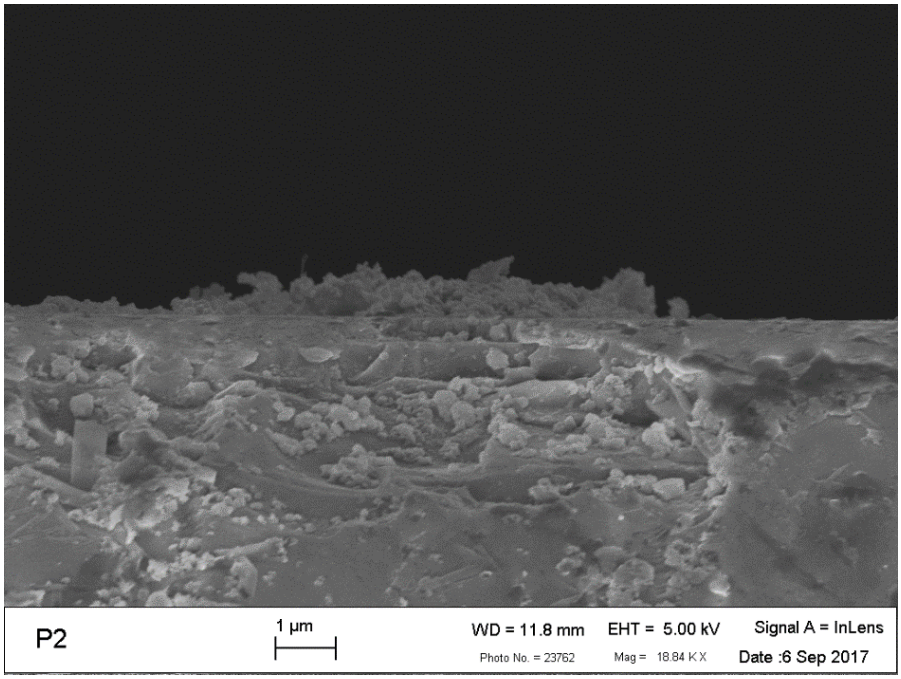

Figure S4.2: SEM side image of a film displaying a thickness of ≈ 1µm

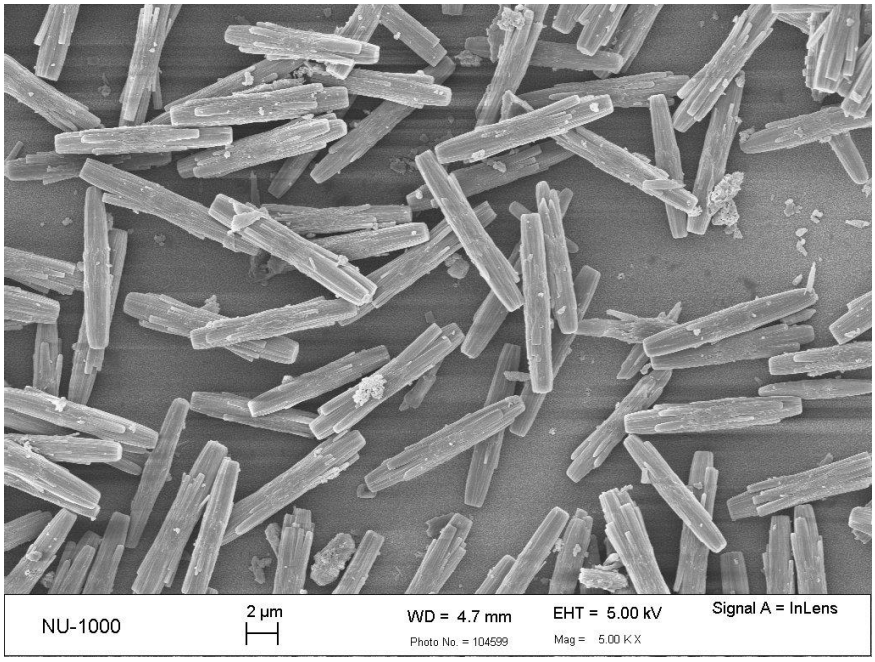

Figure S4.3: SEM image of NU-1000 microcrystals across the film surface

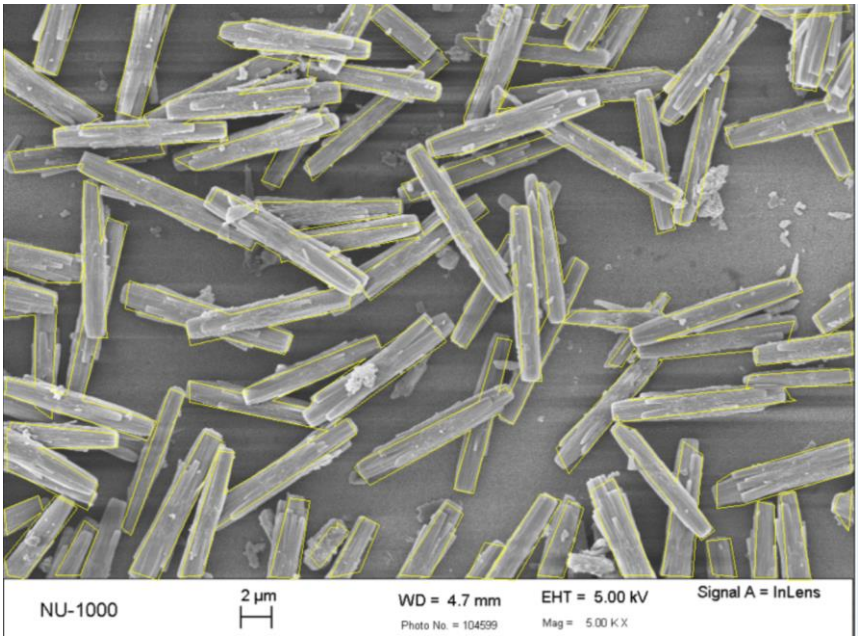

Figure S4.4: SEM image of NU-1000 microcrystals across the film surface. ImageJ program was used to calculate the average perimeter of a rod, and the number of rods per unit of area.

4.6.5 Electrochemical Methods

Analyses were performed in a standard three-electrode array: The M-NU-1000 (M=Fe, Ru, Os) thin film as a working electrode, a Pt mesh as the counter electrode, and a non-aqueous Ag/Ag^{+} reference electrode (0.1 M $TBAPF_6$ in Acetonitrile). Solutions of either 0.1M $TBAPF_6$ or 0.1M TBATFAB in dry DCM (10.0 mL) were used as the supporting electrolyte. The $TBAPF_6$ electrolyte was previously recrystallized in ethyl acetate. Before the experiment was carried out, Argon was bubbled for 10 minutes to the solution, and then left flowing in the head-space of the cell while running the experiment.

For each of the six combinations of metallocene-counter anion couples, the cyclic voltammetry and chronoamperometry experiments were repeated four times on different films, and using fresh electrolyte solution.

4.6.5.1 Cyclic voltammetry analysis

Cyclic voltammograms were collected at a scan rate of 100 mV s^{-1} for 12 cycles.

4.6.5.2 Chronoamperometry analysis – DC Potential Amperometry (DCPA)

Chronoamperometry experiments were carried out by holding the film at a potential just below the redox peak for 20 min, and subsequently, applying a potential above the oxidation process (as determined from CV experiments) during other 20 min. The current vs. time (I vs. t) plots for the latter period were obtained.

4.6.6 Determination of D_e and D_i based on the Sholtz model of solid state voltammetry of microcrystals[14]

4.6.6.1 Step by step sample calculation of the model using a Fe-NU-1000 thin film

The current vs. time (I vs. t) plot obtained for one of the four Fe-NU-1000 thin films (Fe-NU-1000-1) in $TBAPF_6$ is presented in Figure S4.5-A. This chronoamperometric response was plotted as a I√t vs.√t plot (Figure S4.5-B) were the three stages (denoted as A, B, and C) are illustrated.

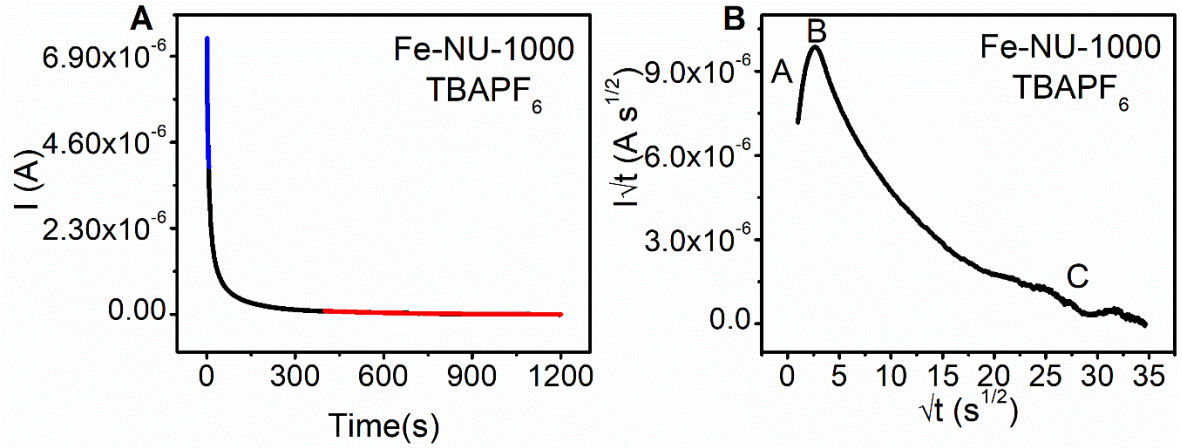

Figure S4.5: A) The current - time response (*I* vs. *t*) at an applied potential *E*, measured in 0.1 M $TBAPF_6$ supporting electrolyte for the film **Fe-NU-1000-1**. *Black*: Experimental response, *Blue*: Model fitting **Stage A** Equation (4.2), *Red*: Model fitting **Stage C** Equation (4.6). **B)** Chronoamperometric response expressed as a $I\sqrt{t}$ vs.$\sqrt{t}$ plot at an applied potential *E*, measured in 0.1 M $TBAPF_6$ supporting electrolyte for the film **Fe-NU-1000-1**

4.6.6.1.1 Stage A

As described in the manuscript, equation (4.2) is characteristic for Stage A:

$$I(t) = \frac{NF}{V_m}\left\{\frac{1}{1+\exp(-\varphi)}\right\}\left[u\left(\left(\frac{\Delta x_0\sqrt{D_e}+\Delta z_0\sqrt{D_i}}{2\sqrt{\pi t}}\right)+\sqrt{D_e D_i}\right)-4D_i\sqrt{2D_e t}\right] \quad \textbf{(4.2)}$$

$$\varphi = \frac{F}{RT}(E_f - E) \quad \textbf{(4.3)}$$

The variables are defined as:

F: Faraday's constant = 96485.3329 C/mol

R: Gas constant = 8.314 J/mol K

T: Temperature = 298.15 K

E_f: Formal potential ($E_{1/2}$ from CV) = 0.21535 V

E: applied potential = 0.512 V

Therefore,

φ = 11.56 (dimensionless)

V_m: molar volume of NU-1000 MOF = 4609.598 cm^3/mol

(from NU-1000 MOF density d = 0.473 g/cm^3, and molar mass MM = 2180.34 g/mol; V_m = MM/d)

N: number of MOF crystallites in the film = 4.40 E6

(from SEM image shown in Figure S4.4. Using ImageJ program, the area of all rods in the image is determined as 956.581 μm^2, and the area of one rod is 18.789 μm^2. Therefore, there are approximately 50.912 rods in the image. The total area of the image is 2314.903 μm^2 and the film has an area of 2.00 E8 μm^2. Consequently, a film will contain 8.64 E4 images. Therefore, there are 4.40 E6 rods in the film.)

u: the length of the three-phase junction or perimeter of the electrode-crystal interface in one single crystallite= 2.68E-03 cm

(from SEM image shown in Figure S4.4. Using ImageJ program, the perimeter of one rod is 26.8 μm)

Δx_0: the distance an ion travels in one hopping step = 8.639 E-08 cm

(from NU-1000 MOF crystal structure, see Figure S4.6)

Δz_0: the distance an electron travels in one hopping step = 1.234 E-07 cm

(from NU-1000 MOF crystal structure, see Figure S4.6)

Using all the previously defined variables, equation (4.2) can be expressed as:

$$I(t) = 9.21 * 10^{7}\left[2.68 * 10^{-3}\left(\left(\frac{8.64 *\ 10^{-8}\sqrt{D_e} + 1.23 * 10^{-7}\sqrt{D_i}}{3.55\sqrt{t}}\right) + \sqrt{D_e D_i}\right) - 4D_i\sqrt{2D_e t}\right] \quad \textbf{(4.2)}$$

The latter expression was used to fit only the data correspondent for Stage A in the current - time response (*I* vs. *t*) plot. From Figure S4.5-B, it was determined that the maximum occurred at $\sqrt{t}$ = 2.6 $s^{1/2}$. Therefore, *t* = 6.76 s, and the expression was fitted only for values from *t* =0 s to *t* = 6.76 s in the (*I* vs. *t*) plot. The fit is shown as a blue trace in Figure S4.5-A. The diffusion coefficient obtained are:

$$\boldsymbol{D_e = 8.65\ E\text{-}07\ cm^2/s}$$

$$\boldsymbol{D_i = 6.85\ E\text{-}17\ cm^2/s}$$

with an R^2 value of 0.97.

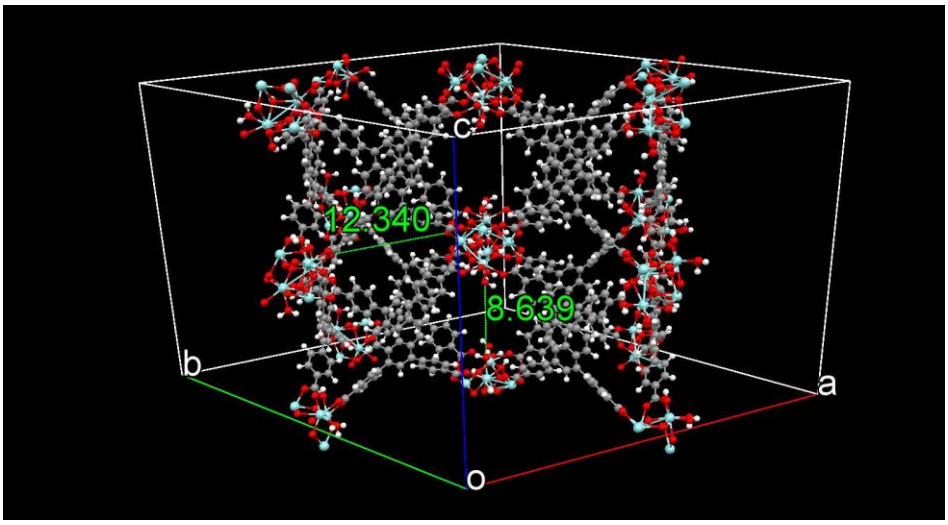

Figure S4.6: Crystal structure of NU-1000 MOF. The hexagonal rods grow along the *c* axis, across the film surface. Therefore, Δx_0 is 8.639 Å and Δz_0 is 12.340 Å

4.6.6.1.2 Stage B

As described in the manuscript, the maximum of the $I\sqrt{t}$ vs.$\sqrt{t}$ curves (Figure S4.5-B), corresponds to a characteristic time (t_{ref}, I_{ref}) in the (I vs. t) plot (Figure S4.5-A), that is defined by the following equations (4.4) and (4.5):

$$t_{ref} = \frac{H^2}{1.1\, D_e} \tag{4.4}$$

$$I_{ref} = 0.72 \frac{NFu}{V_m} \sqrt{D_e D_i} \tag{4.5}$$

All the variables are defined previously is Stage A, excepting:

H: thickness of the MOF particles = 1 µm

(from SEM images, Figure S4.2)

From Figure S4.5-B, it was determined that the maximum occurred at $\sqrt{t}$ = 2.6 $s^{1/2}$. Therefore, t_{ref} = 6.76 s. Using this value and the thickness of the film (H) in equation (4.4), the D_e value in Stage B was obtained as:

$$\mathbf{D_e = 1.34\ E\text{-}09\ cm^2/s}$$

From Figure S4.5-B, it was determined that at t_{ref} = 6.76 s., the current value was I_{ref} = 3.79 E-6. Using this value in equation (4.5), and all the variables previously defined the D_i value was calculated as:

$$\mathbf{D_i = 3.38\ E\text{-}13 cm^2/s}$$

4.6.6.1.3 Stage C

As described in the manuscript, equation (4.6) is characteristic for Stage C:

$$I(t) = \frac{NFLHD_i}{V_m B}\left\{\frac{1}{1+\exp(-\varphi)}\right\} exp\left[\frac{-\pi D_i t}{B^2}\right] \qquad \textbf{(4.6)}$$

All the variables are defined in the previous stages, excepting:

L: average length of the MOF particles = 11.59 µm

(from SEM images, Figure S4.3)

B: average width of the MOF particles = 1.7 µm

(from SEM images, Figure S4.3)

Replacing all the known numerical variables, equation (4.6) can be expressed as:

$$I(t) = (6.28 * 10^4 D_i) exp[-3.42 * 10^8 D_i t] \quad \textbf{(4.6)}$$

The latter expression was used to fit only the data correspondent for Stage C in the current - time response (*I* vs. *t*) plot. The Sholtz model[14] has specified that equation (4.6) has been developed for the very last segment of Stage C, where the total conversion of the crystal is higher than 99%. For all the films on this study, it was assumed that the very end of the conversion occurred at $\sqrt{t}$ = 20 $s^{1/2}$ (Figure S4.5-B). Therefore, the expression was fitted only for values from *t* = 400 to the end of the conversion in the (*I* vs. *t*) plot. The fit is shown as a red trace in Figure S4.5-A. The diffusion coefficient obtained was:

$$\boldsymbol{D_i = 1.52\ E\text{-}11\ cm^2/s}$$

with an R^2 value of 0.88.

4.6.6.2 Statistical error on the D_e and D_i values calculated in each stage

The chronoamperometry experiments were repeated four or three times on different films for each of the metallocene-counter anion combinations. The average and standard deviation of the D_e and D_i values were calculated, at each stage. Also, the R^2 values obtained for the fitting of equation (4.2) in Stage A, and equation (4.6) in Stage C are presented in Table S4.1:

Table S4.1. Summary of the average, standard deviation, and R^2 fitting values for the electronic (D_e) and ionic (D_i) diffusion coefficients for M-NU-1000 (M = Fe, Ru, Os) thin films in PF_6^{1-} and $TFAB^{1-}$ based electrolytes.

Stage A

PF_6^{1-}				$TFAB^{1-}$			
Film	D_e ($cm^2\ s^{-1}$)	D_i ($cm^2\ s^{-1}$)	**Equation (2) R^2**	**Film**	D_e ($cm^2\ s^{-1}$)	D_i ($cm^2\ s^{-1}$)	**Equation (2) R^2**
Fe-1	8.65×10^{-7}	6.85×10^{-17}	0.97	**Fe-5**	3.54×10^{-7}	6.18×10^{-18}	0.98
Fe-2	1.07×10^{-7}	1.59×10^{-17}	0.98	**Fe-6**	6.38×10^{-7}	3.46×10^{-17}	0.96
Fe-3	2.24×10^{-6}	3.54×10^{-17}	0.96	**Fe-7**	4.04×10^{-7}	1.48×10^{-17}	0.99
Fe-4	7.83×10^{-7}	4.07×10^{-17}	0.98	**Fe-8**	1.78×10^{-7}	3.22×10^{-18}	0.99
Average	9.99×10^{-7}	4.01×10^{-17}		**Average**	3.94×10^{-7}	1.47×10^{-17}	
Standard Deviation	7.75×10^{-7}	1.88×10^{-17}		**Standard Deviation**	1.64×10^{-7}	1.23×10^{-17}	

PF_6^{1-}				$TFAB^{1-}$			
Film	D_e ($cm^2\ s^{-1}$)	D_i ($cm^2\ s^{-1}$)	**Equation (2) R^2**	**Film**	D_e ($cm^2\ s^{-1}$)	D_i ($cm^2\ s^{-1}$)	**Equation (2) R^2**
Ru-1	1.30×10^{-5}	6.77×10^{-15}	0.92	**Ru-5**	8.44×10^{-8}	6.62×10^{-18}	1.00
Ru-2	3.43×10^{-5}	4.62×10^{-18}	0.99	**Ru-6**	8.20×10^{-8}	1.27×10^{-34}	0.99
Ru-3	6.96×10^{-6}	1.51×10^{-14}	0.90	**Ru-7**	4.82×10^{-8}	3.05×10^{-34}	0.99
Ru-4	6.56×10^{-6}	1.80×10^{-14}	0.70	**Ru-8**	1.14×10^{-7}	8.90×10^{-19}	1.00
Average	1.52×10^{-5}	9.92×10^{-15}		**Average**	8.22×10^{-8}	1.88×10^{-18}	
Standard Deviation	1.13×10^{-5}	7.03×10^{-15}		**Standard Deviation**	2.33×10^{-8}	2.76×10^{-18}	

PF_6^{1-}				$TFAB^{1-}$			
Film	D_e ($cm^2\ s^{-1}$)	D_i ($cm^2\ s^{-1}$)	**Equation (2) R^2**	**Film**	D_e ($cm^2\ s^{-1}$)	D_i ($cm^2\ s^{-1}$)	**Equation (2) R^2**
Os-1	8.16×10^{-6}	2.78×10^{-18}	0.99	**Os-5**	4.02×10^{-5}	9.28×10^{-33}	0.99
Os-2	4.06×10^{-5}	8.31×10^{-18}	0.99	**Os-6**	4.03×10^{-6}	2.19×10^{-18}	1.00
Os-3	2.14×10^{-5}	1.41×10^{-17}	0.99	**Os-7**	1.04×10^{-5}	2.57×10^{-17}	0.99

Os-4				**Os-8**	1.53×10^{-5}	1.21×10^{-17}	0.99
Average	2.34×10^{-5}	8.40×10^{-18}		**Average**	1.75×10^{-5}	1.00×10^{-17}	
Standard Deviation	1.33×10^{-5}	4.62×10^{-18}		**Standard Deviation**	1.37×10^{-5}	1.01×10^{-17}	

Stage B

	PF_6^{1-}			$TFAB^{1-}$	
Film	D_e ($cm^2\ s^{-1}$)	D_i ($cm^2\ s^{-1}$)	**Film**	D_e ($cm^2\ s^{-1}$)	D_i ($cm^2\ s^{-1}$)
Fe-1	1.34×10^{-9}	3.38×10^{-13}	**Fe-5**	2.60×10^{-10}	9.37×10^{-14}
Fe-2	5.68×10^{-10}	3.06×10^{-14}	**Fe-6**	3.12×10^{-10}	3.28×10^{-13}
Fe-3	5.41×10^{-10}	8.99×10^{-13}	**Fe-7**	5.68×10^{-10}	1.13×10^{-13}
Fe-4	1.88×10^{-9}	2.20×10^{-13}	**Fe-8**	5.98×10^{-10}	3.30×10^{-14}
Average	1.08×10^{-9}	3.72×10^{-13}	**Average**	4.34×10^{-10}	1.42×10^{-13}
Standard Deviation	0.56×10^{-9}	3.23×10^{-13}	**Standard Deviation**	1.50×10^{-10}	1.11×10^{-13}

	PF_6^{1-}			$TFAB^{1-}$	
Film	D_e ($cm^2\ s^{-1}$)	D_i ($cm^2\ s^{-1}$)	**Film**	D_e ($cm^2\ s^{-1}$)	D_i ($cm^2\ s^{-1}$)
Ru-1	1.34×10^{-9}	5.24×10^{-11}	**Ru-5**	2.27×10^{-9}	1.45×10^{-14}
Ru-2	1.88×10^{-9}	5.84×10^{-11}	**Ru-6**	4.64×10^{-9}	1.03×10^{-14}
Ru-3	2.27×10^{-9}	5.60×10^{-12}	**Ru-7**	4.64×10^{-9}	1.21×10^{-14}
Ru-4			**Ru-8**	4.64×10^{-9}	1.58×10^{-14}
Average	1.83×10^{-9}	3.88×10^{-11}	**Average**	4.05×10^{-9}	1.32×10^{-14}
Standard Deviation	0.38×10^{-9}	2.36×10^{-11}	**Standard Deviation**	1.02×10^{-9}	0.21×10^{-14}

	PF_6^{1-}			$TFAB^{1-}$	
Film	D_e ($cm^2\ s^{-1}$)	D_i ($cm^2\ s^{-1}$)	**Film**	D_e ($cm^2\ s^{-1}$)	D_i ($cm^2\ s^{-1}$)
Os-1	4.57×10^{-9}	1.23×10^{-12}	**Os-5**	4.64×10^{-9}	5.07×10^{-12}
Os-2	4.64×10^{-9}	6.97×10^{-12}	**Os-6**	4.64×10^{-9}	5.93×10^{-13}

Os-3	3.15×10^{-9}	4.08×10^{-12}	**Os-7**	2.27×10^{-9}	2.41×10^{-12}
Os-4	3.15×10^{-9}	5.60×10^{-13}	**Os-8**	3.15×10^{-9}	2.82×10^{-12}
Average	3.88×10^{-9}	3.21×10^{-12}	**Average**	3.67×10^{-9}	2.72×10^{-12}
Standard Deviation	0.73×10^{-9}	2.54×10^{-12}	**Standard Deviation**	1.01×10^{-9}	1.59×10^{-12}

Stage C

PF_6^{1-}			$TFAB^{1-}$		
Film	D_i ($cm^2\ s^{-1}$)	**Equation (6) R^2**	**Film**	D_i ($cm^2\ s^{-1}$)	**Equation (6) R^2**
Fe-1	1.52×10^{-11}	0.88	**Fe-5**	1.52×10^{-11}	0.90
Fe-2	2.10×10^{-11}	0.90	**Fe-6**	1.21×10^{-11}	0.95
Fe-3	5.77×10^{-12}	0.45	**Fe-7**	1.85×10^{-11}	0.61
Fe-4	1.58×10^{-11}	0.59	**Fe-8**	1.98×10^{-11}	0.55
Average	1.44×10^{-11}		**Average**	1.64×10^{-11}	
Standard Deviation	0.55×10^{-11}		**Standard Deviation**	0.30×10^{-11}	

PF_6^{1-}			$TFAB^{1-}$		
Film	D_i ($cm^2\ s^{-1}$)	**Equation (6) R^2**	**Film**	D_i ($cm^2\ s^{-1}$)	**Equation (6) R^2**
Ru-1	4.95×10^{-12}	-1.80	**Ru-5**	2.22×10^{-11}	0.40
Ru-2	5.05×10^{-12}	-1.52	**Ru-6**	2.44×10^{-11}	0.30
Ru-3	5.25×10^{-12}	-0.50	**Ru-7**	2.11×10^{-11}	0.52
Ru-4			**Ru-8**	2.19×10^{-11}	0.66
Average	5.08×10^{-12}		**Average**	1.22×10^{-11}	
Standard Deviation	0.12×10^{-12}		**Standard Deviation**	0.12×10^{-11}	

PF_6^{1-}			$TFAB^{1-}$		
Film	D_i ($cm^2\ s^{-1}$)	**Equation (6) R^2**	**Film**	D_i ($cm^2\ s^{-1}$)	**Equation (6) R^2**
Os-1	5.28×10^{-12}	-0.30	**Os-5**	5.15×10^{-12}	-0.54

Os-2	4.97×10^{-12}	-1.24	**Os-6**	4.95×10^{-12}	0.87
Os-3	5.10×10^{-12}	0.83	**Os-7**	5.60×10^{-12}	0.24
Os-4			**Os-8**	5.21×10^{-12}	-0.21
Average	5.12×10^{-12}		**Average**	5.23×10^{-12}	
Standard Deviation	0.13×10^{-12}		**Standard Deviation**	0.24×10^{-12}	

4.7 ACKNOWLEDGMENTS

This material is based upon work supported by the National Science Foundation under Grant No. 1551964

4.8 REFERENCES

1. Allendorf, M. D.; Schwartzberg, A.; Stavila, V.; Talin, A. A. A Roadmap to Implementing Metal–Organic Frameworks in Electronic Devices: Challenges and Critical Directions. *Chemistry – A European Journal* **2011,** 17 (41), 11372-11388 DOI: 10.1002/chem.201101595.

2. Stavila, V.; Talin, A. A.; Allendorf, M. D. MOF-based electronic and opto-electronic devices. *Chemical Society Reviews* **2014,** 43 (16), 5994-6010 DOI: 10.1039/C4CS00096J.

3. Liu, J.; Woll, C. Surface-supported metal-organic framework thin films: fabrication methods, applications, and challenges. *Chemical Society Reviews* **2017,** 46 (19), 5730-5770 DOI: 10.1039/C7CS00315C.

4. Falcaro, P.; Ricco, R.; Doherty, C. M.; Liang, K.; Hill, A. J.; Styles, M. J. MOF positioning technology and device fabrication. *Chem Soc Rev* **2014,** 43 (16), 5513-60 DOI: 10.1039/c4cs00089g.

5. Halls, J. E.; Jiang, D.; Burrows, A. D.; Kulandainathan, M. A.; Marken, F. In *Electrochemistry: Volume 12*; The Royal Society of Chemistry: 2014; Vol. 12, pp 187-210.

6. Gándara, F.; Uribe-Romo, F. J.; Britt, D. K.; Furukawa, H.; Lei, L.; Cheng, R.; Duan, X.; O'Keeffe, M.; Yaghi, O. M. Porous, Conductive Metal-Triazolates and Their Structural Elucidation by the Charge-Flipping Method. *Chemistry – A European Journal* **2012,** 18 (34), 10595-10601 DOI: 10.1002/chem.201103433.

7. Kobayashi, Y.; Jacobs, B.; Allendorf, M. D.; Long, J. R. Conductivity, Doping, and Redox Chemistry of a Microporous Dithiolene-Based Metal−Organic Framework. *Chemistry of Materials* **2010,** 22 (14), 4120-4122 DOI: 10.1021/cm101238m.

8. Marshall, R. J.; Forgan, R. S. Postsynthetic Modification of Zirconium Metal-Organic Frameworks. *European Journal of Inorganic Chemistry* **2016,** 2016 (27), 4310-4331 DOI: 10.1002/ejic.201600394.

9. Lin, S.; Pineda-Galvan, Y.; Maza, W. A.; Epley, C. C.; Zhu, J.; Kessinger, M. C.; Pushkar, Y.; Morris, A. J. Electrochemical Water Oxidation by a Catalyst-Modified Metal–Organic Framework Thin Film. *ChemSusChem* **2017,** 10 (3), 514-522 DOI: 10.1002/cssc.201601181.

10. Hod, I.; Bury, W.; Gardner, D. M.; Deria, P.; Roznyatovskiy, V.; Wasielewski, M. R.; Farha, O. K.; Hupp, J. T. Bias-Switchable Permselectivity and Redox Catalytic Activity of a Ferrocene-Functionalized, Thin-Film Metal–Organic Framework Compound. *The Journal of Physical Chemistry Letters* **2015,** 6 (4), 586-591 DOI: 10.1021/acs.jpclett.5b00019.

11. Sun, L.; Miyakai, T.; Seki, S.; Dincă, M. Mn2(2,5-disulfhydrylbenzene-1,4-dicarboxylate): A Microporous Metal–Organic Framework with Infinite (−Mn–S−)∞ Chains and High Intrinsic

Charge Mobility. *Journal of the American Chemical Society* **2013,** 135 (22), 8185-8188 DOI: 10.1021/ja4037516.

12. Narayan, T. C.; Miyakai, T.; Seki, S.; Dincă, M. High Charge Mobility in a Tetrathiafulvalene-Based Microporous Metal–Organic Framework. *Journal of the American Chemical Society* **2012,** 134 (31), 12932-12935 DOI: 10.1021/ja3059827.

13. Ahrenholtz, S. R.; Epley, C. C.; Morris, A. J. Solvothermal Preparation of an Electrocatalytic Metalloporphyrin MOF Thin Film and its Redox Hopping Charge-Transfer Mechanism. *Journal of the American Chemical Society* **2014,** 136 (6), 2464-2472 DOI: 10.1021/ja410684q.

14. Schröder, U.; Oldham, K. B.; Myland, J. C.; Mahon, P. J.; Scholz, F. Modelling of solid state voltammetry of immobilized microcrystals assuming an initiation of the electrochemical reaction at a three-phase junction. *Journal of Solid State Electrochemistry* **2000,** 4 (6), 314-324 DOI: 10.1007/s100080000130.

15. Hod, I.; Farha, O. K.; Hupp, J. T. Modulating the rate of charge transport in a metal-organic framework thin film using host:guest chemistry. *Chemical Communications* **2016,** 52 (8), 1705-1708 DOI: 10.1039/C5CC09695B.

16. Swarts, J. C.; Nafady, A.; Roudebush, J. H.; Trupia, S.; Geiger, W. E. One-Electron Oxidation of Ruthenocene: Reactions of the Ruthenocenium Ion in Gentle Electrolyte Media. *Inorganic Chemistry* **2009,** 48 (5), 2156-2165 DOI: 10.1021/ic802105b.

17. Zahl, A.; van Eldik, R.; Matsumoto, M.; Swaddle, T. W. Self-Exchange Reaction Kinetics of Metallocenes Revisited: Insights from the Decamethylferricenium−Decamethylferrocene

Reaction at Variable Pressure. *Inorganic Chemistry* **2003,** 42 (12), 3718-3722 DOI: 10.1021/ic030067y.

18. Hill, M. G.; Lamanna, W. M.; Mann, K. R. Tetrabutylammonium tetrakis[3,5-bis(trifluoromethyl)phenyl]borate as a noncoordinating electrolyte: reversible 1e- oxidations of ruthenocene, osmocene, and Rh2(TM4)42+ (TM4=2,5-diisocyano-2,5-dimethylhexane). *Inorganic Chemistry* **1991,** 30 (25), 4687-4690 DOI: 10.1021/ic00025a003.

19. Smith, T. P.; Iverson, D. J.; Droege, M. W.; Kwan, K. S.; Taube, H. Halogen-mediated electron transfer between metallocenes of ruthenium and osmium in the oxidation states 4+ and 2+. *Inorganic Chemistry* **1987,** 26 (17), 2882-2884 DOI: 10.1021/ic00264a033.

20. Engesser, T. A.; Lichtenthaler, M. R.; Schleep, M.; Krossing, I. Reactive p-block cations stabilized by weakly coordinating anions. *Chemical Society Reviews* **2016,** 45 (4), 789-899 DOI: 10.1039/C5CS00672D.

21. Reeves, P. C. Carboxylation of aromatic compounds: Ferrocenecarboxylic acid. *Organic Syntheses* **1977,** 56, 28 DOI: DOI: 10.15227/orgsyn.056.0028.

22. Stylianou, K. C.; Heck, R.; Chong, S. Y.; Bacsa, J.; Jones, J. T. A.; Khimyak, Y. Z.; Bradshaw, D.; Rosseinsky, M. J. A Guest-Responsive Fluorescent 3D Microporous Metal−Organic Framework Derived from a Long-Lifetime Pyrene Core. *Journal of the American Chemical Society* **2010,** 132 (12), 4119-4130 DOI: 10.1021/ja906041f.

23. Mondloch, J. E.; Bury, W.; Fairen-Jimenez, D.; Kwon, S.; DeMarco, E. J.; Weston, M. H.; Sarjeant, A. A.; Nguyen, S. T.; Stair, P. C.; Snurr, R. Q.; Farha, O. K.; Hupp, J. T. Vapor-Phase Metalation by Atomic Layer Deposition in a Metal–Organic Framework. *Journal of the American Chemical Society* **2013,** 135 (28), 10294-10297 DOI: 10.1021/ja4050828.

5. Conclusions and Future Work

In order to design MOFs as active materials to achieve efficient charge storage in electronic devices, a deeper understanding on the electron, ion, and proton transport pathways in these materials is needed. In the present work, we have demonstrated that proton-coupled electron transport can be modulated in anthraquinone-based Zr MOFs as a function of the pH, and that structural features such as the positioning of the quinone moiety with respect to the zirconium node, the amount of defects, and the pore size of these materials are directly influencing the transport properties of these frameworks. The observed possibility of proton transport in MOFs through a cooperative behavior between the ligand and the inorganic node encourage further research in this area, since proton transport plays an important role in many processes such as enzymatic catalysis, where MOF materials are potential candidates.

The studies of quinone accessibility and specific capacitance in the two anthraquinone-based Zr MOFs thin films and slurry modified electrodes, showed that the pKa of the frameworks, the defectivity, and the stabilization through hydrogen bonding have also an important effect on the percentage of quinones active and their ability to store charge in both type of electrodes. While the anthraquinone MOF thin films displayed superior performance than the powder-based electrodes, improving charge transport paths in the films through crystal engineering methods is vital to exploit the potential of these materials as charge transport agents.

Remarkably, the systematic variation of metallocene redox center and counter anions in a series of chronoamperometry experiments allowed the elucidation, for the first time, of the relative contribution of electronic and ionic diffusion in metallocene-doped NU-MOF thin films. The trends observed in the diffusion coefficients (D_e and D_i) of these systems obtained in PF_6^{1-} and

$TFAB^{1-}$ based electrolytes at the different stages of the electrochemical reaction, demonstrated that the redox hopping rates inside frameworks can be controlled through the modifications of the self-exchange rates of redox centers, the use of large MOF channels, and the utilization of smaller counter anions. The results constitute a significant advancement to the understanding of electron and ion mobility in the context of electrochemical experiments, and can be used to guide further research into other redox-active MOFs. Specifically, we encourage research efforts on applying the theoretical method utilized on the present work to experimental data of MOFs containing the redox moieties in the ligand itself, and displaying different pore sizes.